University of Alberta

ALTA: ALBERTA LARGE AREA TIME COINCIDENCE ARRAY

by

Andrew Hamilton ©

A thesis submitted to the Faculty of Graduate Studies and Research in partial fulfillment of the requirements for the degree of **Master of Science**.

Department of Physics

Edmonton, Alberta
Fall 2002

National Library
of Canada

Bibliothèque nationale
du Canada

Acquisitions and
Bibliographic Services

Acquisitions et
services bibliographiques

395 Wellington Street
Ottawa ON K1A 0N4
Canada

395, rue Wellington
Ottawa ON K1A 0N4
Canada

The author has granted a non-exclusive licence allowing the National Library of Canada to reproduce, loan, distribute or sell copies of this thesis in microform, paper or electronic formats.

L'auteur a accordé une licence non exclusive permettant à la Bibliothèque nationale du Canada de reproduire, prêter, distribuer ou vendre des copies de cette thèse sous la forme de microfiche/film, de reproduction sur papier ou sur format électronique.

The author retains ownership of the copyright in this thesis. Neither the thesis nor substantial extracts from it may be printed or otherwise reproduced without the author's permission.

L'auteur conserve la propriété du droit d'auteur qui protège cette thèse. Ni la thèse ni des extraits substantiels de celle-ci ne doivent être imprimés ou autrement reproduits sans son autorisation.

0-612-81405-X

Canada

University of Alberta
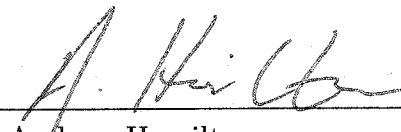
Library Release Form

Name of Author: Andrew Hamilton

Title of Thesis: ALTA: Alberta Large Area Time Coincidence Array

Degree: Master of Science

Year this Degree Granted: 2002

Andrew Hamilton
208-10636 120 St.
Edmonton, AB
Canada T5H 4L5
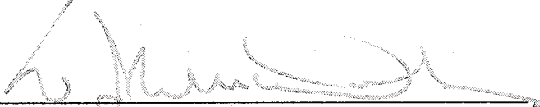
Date: Sept 24/02
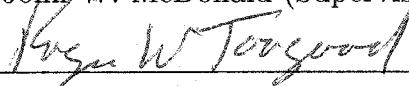
University of Alberta

Faculty of Graduate Studies and Research

The undersigned certify that they have read, and recommend to the Faculty of Graduate Studies and Research for acceptance, a thesis entitled **ALTA: Alberta Large Area Time Coincidence Array** submitted by Andrew Hamilton in partial fulfillment of the requirements for the degree of **Master of Science**.

Dr. John W. McDonald (Supervisor)

Dr. Roger Toogood (External)

Dr. James Pinfold

Dr. Sharon Morsink

Date: Sept 24/02

Abstract

The Alberta Large Area Time Coincidence Array (ALTA) is a joint collaboration between the University of Alberta and area high schools to study some fundamental properties of high energy cosmic rays. Scintillating air shower detectors are mounted on the roofs of Alberta high schools and connected to a data acquisition system that is controlled by a computer in the classroom. The primary objective of the ALTA project is to find correlations in the arrival times of air showers over large distances and to find non-random arrival times in showers arriving at a single site. This thesis contains a review of cosmic ray physics, a detailed description of the ALTA experiment, and an overview of the analysis routines and techniques that will be used.

Acknowledgements

Contents

List of Tables

List of Figures

List of Symbols

Acronyms

ADC	Analog to Digital Converter
ALTA	Alberta Large Area Time Coincidence Array
CFPHT	Constant Fraction Pulse Height Trigger
EAS	Extensive Air Shower
eV	electron Volt
FIFO	First In First Out memory device
FPGA	Field Programable Gate Array
GPS	Global Positioning System
HA	Hour Angle
HV	High Voltage
ICRC	International Cosmic Ray Conference
LST	Local Sidereal Time
Mpc	Megaparsec
PC	Personal Computer
RMS	Root Mean Square
TAC	Time to Analog Converter
TDC	Time to Digital Converter
UTC	Universal Coordinated Time

Symbols

α	Right Ascension angle of celestial coordinates
δ	Declination angle of celestial coordinates
l	Galactic longitude of galactic coordinates
b	Galactic latitude of galactic coordinates
θ	Altitude angle of horizon coordinates
ϕ	Azimuth angle of horizon coordinates
ρ	Longitude on Earth
λ_c	Geocentric latitude on Earth
λ_g	Geographic latitude on Earth
β	Vertical incidence angle of correlated showers (see Figure 4.6)
ξ	Exponential slope of primary cosmic ray energy spectrum

0.1 Introduction

0.1.1 Objectives of Experiment

The Alberta Large Area Time Coincidence Array (ALTA) was first conceived by Jim Pinfold in the mid 90's. The concept is to create a sparse, but very large area, cosmic ray detector to study some intriguing properties of cosmic ray air showers that have been hinted at, but never fully explored. Properties such as correlations between showers separated by very large distances [3] [4] [5], as well as non-random and chaotic series in the arrival times of showers [6] [7] [8] are currently unexplained. The primary objective of the ALTA experiment to gather more data to help unravel these mysteries.

ALTA also has an interest in promoting outreach at the high school level. The experiment's detection equipment is housed at high schools throughout Alberta, giving high school students the opportunity to observe and participate in fundamental scientific research. For more information on the outreach aspects of ALTA visit [9].

ALTA is part of a larger network of experiments called NALTA (North American Large Area Time Coincidence Array). Each experiment in NALTA has objectives similar to ALTA; some placing primary interest in outreach, others placing primary interest in research, all participating actively in both. For more information on NALTA visit [10].

0.1.2 Objectives of Thesis

This thesis has a two-fold objective; the primary goal is to explain work that I have participated in for the ALTA project, the secondary goal is to act as a guide and information manual to the high school teachers involved in the experiment. To this end the material is presented with the intention of being understood by someone with a limited background in physics research, while still exploring the fundamental concepts of cosmic ray research. Due to the nature of the requirements of a Masters thesis, this work will focus on the scientific aspects of the ALTA project, not the outreach aspects.

0.1.3 Summary of Chapters

Chapter 1 is a review of cosmic ray physics and includes a description of the current understanding of the cosmic ray spectrum, the possible origins of cosmic rays, and a brief outline of the current experimental situation of cosmic ray physics. The possibility of correlated and non-random cosmic ray showers is also discussed.

Chapter 2 includes a description of the ALTA experiment. The system and its components are outlined.

Chapter 3 contains a description of the calibration processes and the uncertainties involved in the ALTA system.

In Chapter 4 is the data analysis routines are described. The body of the chapter includes the processes of the routines, while the source code is written in an appendix. The structure and organization of the ALTA data is also included in this chapter.

Chapter 5 contains a conclusion with an overview of what has been accomplished and what still needs to be done to complete the ALTA experiment.

Chapter 1

Cosmic Rays

The purpose of this chapter is to introduce the basic physics of cosmic rays, to present some of the questions of interest to cosmic ray researchers, and to outline some of the experimental attempts currently being applied to answer those questions.

1.1 Cosmic Ray Basics

Cosmic rays were first discovered by Victor Hess in 1912, a discovery which earned him the 1936 Nobel Prize. In a balloon flight up to an altitude of 5350 m, Hess discovered that radiation in the atmosphere increases with altitude. He explained this observation in his 1912 paper:

> *The results of the present observations seem to be most readily explained by the assumption that a radiation of very high penetrating power enters our atmosphere from above, and still produces in the lowest layers a part of the ionization observed in closed vessels.*
>
> - Victor Hess[11]

Naturally, with this discovery there came many questions about cosmic rays. What are they? Where do they come from? How do they get here? How many are there? How much energy do they carry? Ninety years have passed and, while much has been learned, some important questions still remain.

So what do we know about cosmic rays? Cosmic rays are subatomic particles from space constantly bombarding the Earth's atmosphere. It is estimated

1

that roughly 90% of cosmic rays are hydrogen nuclei (protons) and helium nuclei, about 9% heavier nuclei, and the remaining 1% are electrons and positrons [12]. Traditionally, photons and neutrinos were not considered to be cosmic rays because they do not carry any charge. We know today that photons (and even neutrinos) can produce a cosmic ray phenomena known as an *air shower*, a very important phenomena in modern day cosmic ray research.
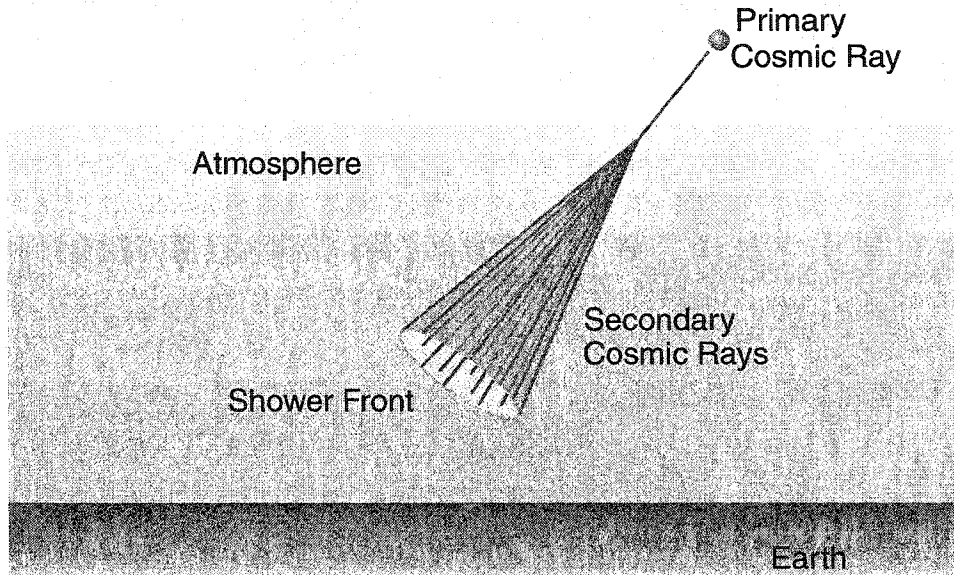
Figure 1.1: Simplified diagram of an air shower

Figure 1.1 is an extraordinarily simplified diagram of a cosmic ray air shower. Air showers occur when a high energy cosmic ray collides with an atmospheric nucleus. The high energy subatomic collision produces additional high energy particles, which then collide with other nuclei in the atmosphere, and so on. This process causes a cascade, or shower, of particles streaming through the atmosphere. The cosmic ray that initiates the shower is referred to as the *primary* cosmic ray, and the shower of particles produced are called *secondary* cosmic rays, or *secondaries*. The secondaries all travel very close to the speed of light, so almost all of them stay in a roughly planar *shower front*. When an air shower is large enough that the secondaries reach the ground it is called an *extensive air shower* (EAS). Extensive air showers will be discussed in more detail in Section 1.2.

The following sections contain an outline of the essential features of primary cosmic rays. The first sections will deal with the energy and composition spectra, and the latter sections will discuss questions about the origin of cosmic rays and what the energy and composition spectra could be telling us about the origin question.

1.1.1 The Energy Spectrum

Cosmic rays have a very wide range of energies. The lowest energy cosmic rays to produce an effect in the Earth's atmosphere are around 10^8 eV. Less energetic particles are deflected by the solar wind and the Earth's magnetic field. The highest energy cosmic rays yet observed are around 10^{20} eV.
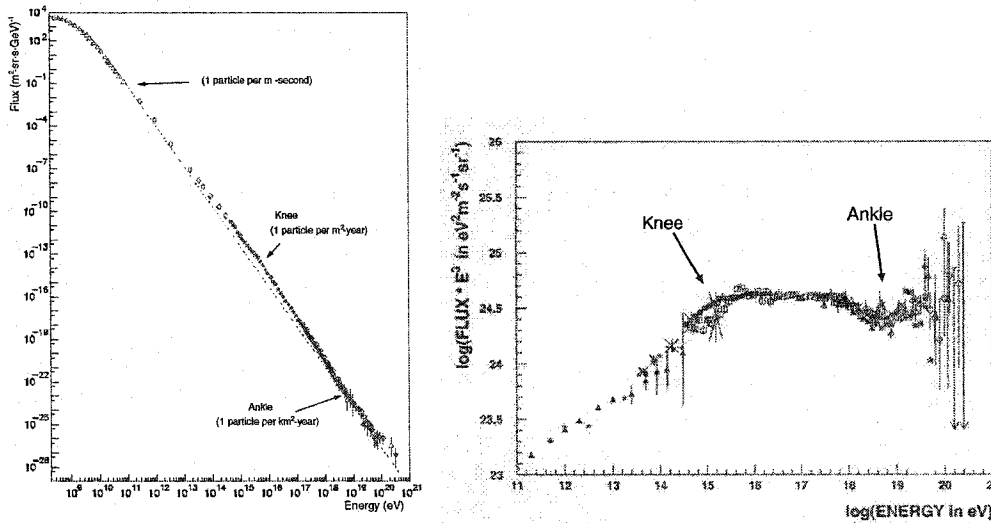
Figure 1.2: Cosmic ray flux as a function of primary energy (left)[1], cosmic ray flux×E^3 as a function of energy to emphesis knee and ankle (right)[2].

Figure 1.2 is a plot of the measured cosmic ray energy spectrum. The first part of the spectrum, below roughly 10^{10} eV, is relatively well understood because the flux is high enough that significant statistics can be achieved by direct measurement of the cosmic ray itself, and not the air shower that it produces.

The rest of the spectrum shows an approximately exponential dependence of the form:

$$\frac{dF}{dE} = kE^{-\xi}$$

3

The value of the exponential slope, ξ, remains almost constant over 10 orders of magnitude. The section between 10^{10} eV and 10^{15} eV satisfies $\xi = 2.7$, while the section between 10^{15} eV and 10^{18} eV satisfies $\xi = 3.1$. The change in the power law at 10^{15} eV is called the 'knee' of the spectrum. Why the spectrum changes at 10^{15} eV is not yet understood. The spectrum then flattens out slightly to $\xi \simeq 2.3$ [13] at approximately 10^{18} eV. This kink is called the 'ankle' of the spectrum. Its cause is also unknown. So, not far into our discussion of cosmic rays, we are already faced with some puzzling, yet fundamental, unanswered questions.

And what is there past the ankle? One of the most intriguing mysteries in cosmic ray physics today is the question of where, or if, the spectrum will end. The question seemed to have a theoretical answer in 1966, but comparison with recent experiments simply makes the problem more puzzling than before. In 1966 Kenneth Greisen published a paper [14] titled *"End to the Cosmic-Ray Spectrum?"* explaining that we should observe a very sharp cut-off of the spectrum at about 5×10^{19} eV. This expected cut-off in the spectrum is now called the Greisen-Zatsepin-Kuz'min (or GZK) limit. The Zatsepin-Kuz'min part of the name comes because G.T. Zatsepin and V.A. Kuz'min published a similar paper [15] at the same time as Greisen. At the time of publication of Greisen's paper there had been one observation of a cosmic ray with an energy of 1.0×10^{19} eV by John Linsley of the Volcano Ranch experiment [16]. Greisen called this event "quite remarkable" [14], due to the very low probability he had calculated for such high energy events. Since then there has been an interestingly large number of even less probable events.

What causes the GZK limit? In 1965 Arno Penzias and Robert Wilson of Bell labs discovered an unexpected source of microwave electromagnetic radiation coming from all directions. The radiation was characteristic of the Planckian black body radiation that would be emitted from a source at 2.73 K, as shown in Figure 1.3 [17]. This radiation is now called the cosmic microwave background (CMB), and seems to permeate all space. The CMB is now interpreted to be the cosmic background radiation (CBR) predicted by the standard Big Bang model.

4
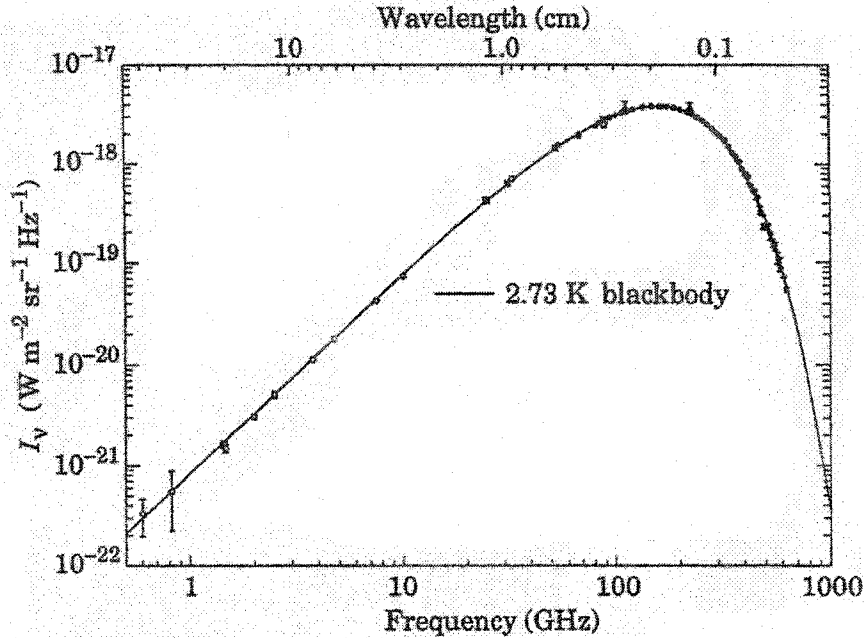
Figure 1.3: Cosmic Microwave Background (CMB) frequency spectrum

Extremely high energy protons are expected to collide with one of these CMB photons roughly once every 20 million years. If the proton has more than 5×10^{19} eV, than a collision with a CMB photon has enough center of mass energy to be above the threshold for the $p + \gamma \Rightarrow p + \pi$ reaction. The creation of the pion takes energy away from the proton, degrading its energy. So, the CMB reduces the distances over which protons can carry energies greater than 5×10^{19} eV. The net result is that protons with more than 5×10^{19} eV cannot travel more than about 160 million light years (or 50 Mpc) through the CMB, without their energy being degraded below 5×10^{19} eV. But, if the proton has less than 5×10^{19} eV then the collisions with CMB photons are elastic, and the CMB is essentially invisible. Figure 1.4 (adapted from [18]) is a plot of the attuation length of protons travelling in the CMB. Notice that the energy of any proton above 5×10^{19} eV will be degraded as the distance it travels increases.

So what does the GZK limit tell us? Basically, it says that if we observe cosmic ray protons above 5×10^{19} eV then they must have come from a source
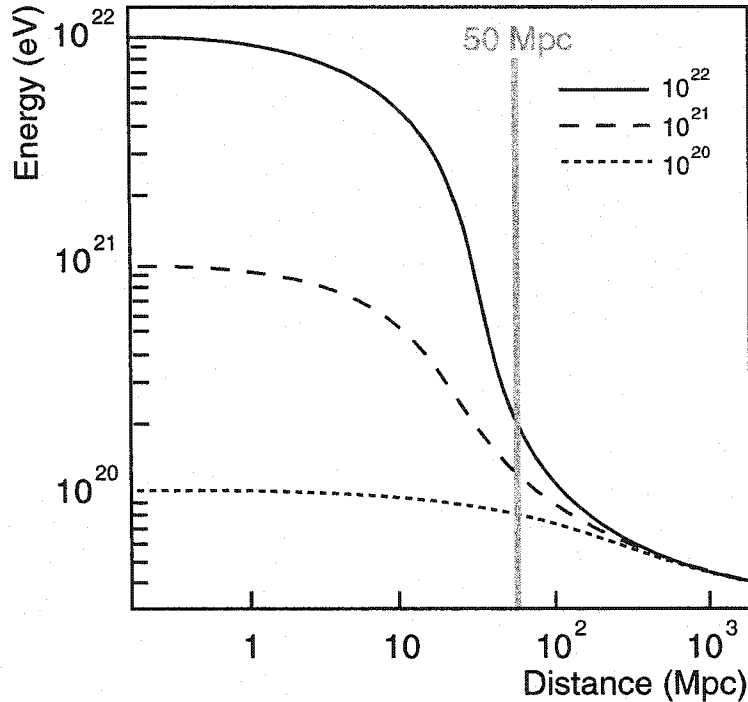
Figure 1.4: Attenuation length of protons in CMB, showing the GZK limit at about 50 Mpc. The three lines represent three different initial energies: 10^{20}, 10^{21}, and 10^{22} eV.

less than 50 Mpc away[1]. Therein lies the conundrum; events above 5×10^{19} eV have been observed, but there doesn't seem to be any nearby astronomical objects that could accelerate particles to such a high energy.

At the 26th International Cosmic Ray Conference (ICRC) a total of 14 events above 10^{20} eV were reported [13] [19]. The two highest energy events were observed by the Akeno Giant Air Shower Array (AGASA) in Japan, and the HiRes experiment in Utah. They had energies of 2×10^{20} eV and 3×10^{20} eV, respectively. Figure 1.5 [13] shows a plot of the spectrum of AGASA's data.

1.1.2   The Composition Spectrum

At the beginning of this chapter I mentioned that roughly 90% of cosmic rays are believed to be hydrogen and helium nuclei, about 9% heavier nuclei,

---

[1]Proton collisions with the CMB is a statistical process, so there is a chance that a proton could retain its energy for more than 50 Mpc, but it is *very* unlikely
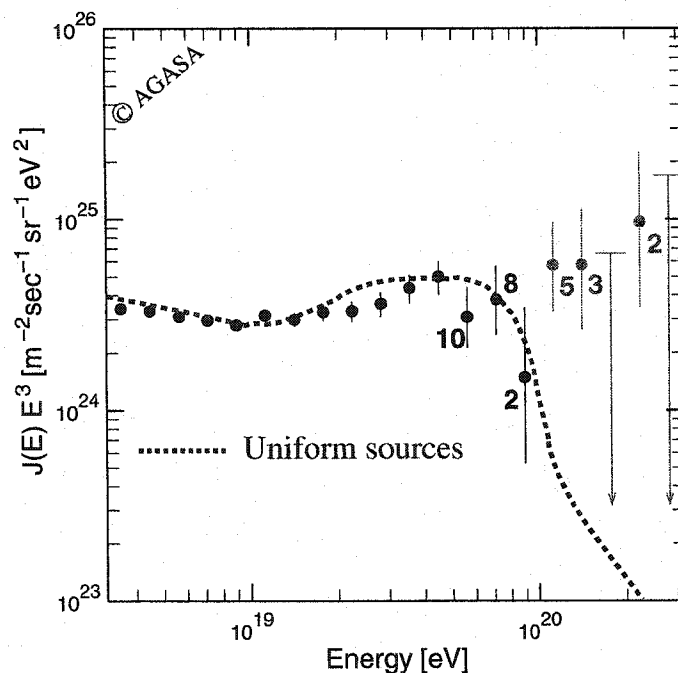
Figure 1.5: The ultra-high energy cosmic ray spectrum reported by the AGASA experiment at the 1999 ICRC. The dotted line is the flux predicted with the GZK limit.

and the remaining 1% are electrons and positrons. Since the flux of low energy cosmic rays is so much greater than the flux of high energy cosmic rays, this ratio is dominated by the composition of the low energy cosmic rays. To look at the composition in the higher energy regions, we need to look at the spectrum piece by piece.

Below 10^{15} eV the flux of cosmic rays is large enough that experiments in high altitude balloons, and on space shuttles, can detect enough cosmic rays to acquire significant statistics. These experiments are called direct measurement experiments because they detect the cosmic ray, not the air shower produced by the cosmic ray. Because they are measuring the cosmic ray itself direct measurement experiments can determine the composition of the particle relatively easily, and thus have created a very detailed description of the composition of the cosmic ray spectrum below 10^{15} eV. Figure 1.6 [20] shows the abundance of species found in cosmic rays compared to the overall universal abundances.

The most prominent difference in the two abundances plots is the over-
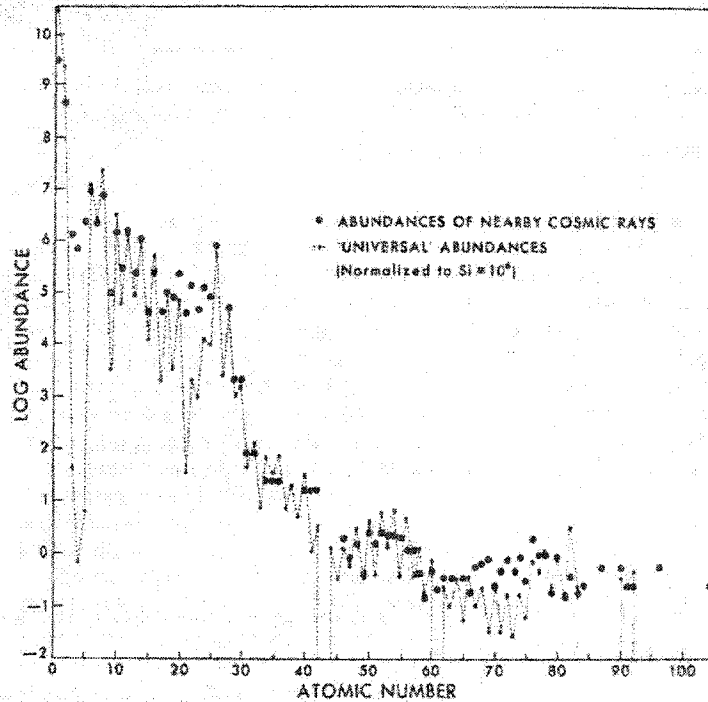
Figure 1.6: The abundances of cosmic rays compared to galactic abundances (normalized to 100 at Si)

abundance of Li, Be, and B in the cosmic ray population. This overabundance is referred to as the LiBeB problem. The most popular explanation of this problem is a process called spallation. Spallation occurs when a heavy nucleus interacts with a proton and fragments into lighter nuclei. The increase in the number of Li, Be, and B nuclei is caused by heavy cosmic rays fragmenting into lighter nuclei like Li, Be, and B. The same can be seen to a lesser extent in the nuclear species just below Fe.

So the composition of cosmic rays in the low energy region is reasonably well understood, but what about at higher energies? As energies approach the knee, the flux is too low for balloon and space craft experiments to get significant statistics. This is where ground based experiments begin to take over. Ground based experiments rely on the observation of some component of cosmic ray air showers. The largest disadvantage for ground based experiment is the difficulty of determining the composition of the primary. Since a typical cosmic ray shower starts around 10 km up in the atmosphere, the challenge of

8

determining the composition of the primary is equivalent to determining the mass and charge of a nucleus 10 km away. Charge determination is currently not possible and mass determination is heavily model dependent. So, when we talk about composition measured by ground based experiments we will discuss whether the primaries are light (like protons) or heavy (like Fe).

As energies approach the knee, experiments like DICE (Dual Imaging Cerenkov Experiment), CASA-MIA (Chicago Air Shower Array - MIchigan muon Array), and JACEE (Japanese-American Cooperative Emulsion Experiment) [21] show that the composition seems to shift from light to heavy. This observation is still under debate since direct measurement experiments like JACEE have very few statistics in the region, and ground based experiments like CASA-MIA and DICE have the model dependence problems discussed above.

At energies above the knee the problem gets worse since the flux continues to decrease; around the ankle matters get worse still, because the models are just extrapolations of lower energy models. Even so, experiments like AGASA [22] and HiRes [23] (these experiments are discussed in Section 1.4) have shown some indications that the composition seems to be getting lighter as energies approach the ankle. HiRes has even shown that the composition seems to be continuing to get lighter above the ankle in the 10^{18} eV to 10^{19} eV region [24].

The question of composition is very important in the discussion of high energy cosmic rays. The composition seems to change at both the knee and the ankle of the energy spectrum. At the knee, as ξ steepens, the composition gets heavier. At the ankle, as ξ flattens, the composition seems to get lighter. Is the change in the composition spectrum the cause of the change in the energy spectrum? If so, what causes the change in the composition spectrum?

Composition is equally important in the question of cosmic rays past the GZK limit. There are theories that the GZK limit has been observed and that the HiRes and AGASA events above 10^{20} eV are gamma rays [25], not protons. Knowing the composition of high energy cosmic rays is likely to be important in solving the multitude of cosmic ray mysteries.

1.1.3 A Question of Origin

The origins of cosmic rays have been a question of hot debate since their discovery. Where do cosmic rays come from? To the naive observer the solution would seem simple: their arrival direction must point back to where they come from. However, cosmic rays appear almost completely isotropic (no preferred direction) for the entire energy spectrum. So, the question of origin does not seem to have a simple solution. What the naive observer didn't take into account was the galactic and intergalactic magnetic fields. When a charged particle travels through a magnetic field its path is bent by the field. So, cosmic rays come to Earth via very complex trajectories following the paths governed by the galactic and intergalactic magnetic fields.

So how can we tell where cosmic rays come from? By modeling the expected physics of the origin's system and comparing the predictions with observations. A complete model for the origins of cosmic rays must fit the observed energy spectrum, composition spectrum, and isotropy information; and take into account production, acceleration, and propagation of the cosmic rays. No present day model can adequately explain all of these things for all energies, especially the highest energies.

At the low end of the spectrum, between 10^8 and 10^{10} eV, Figure 1.2 shows a plateau at the lowest energies. The amount of flattening in this part of the spectrum is dependent on solar activity. When solar activity is high the flux of cosmic rays in this region decreases, and when solar activity is low the flux increases. This implies that cosmic rays in this region come from outside the heliosphere, because increased solar activity means an increased magnetized solar wind that acts to shield out the charged cosmic rays. If the cosmic rays in this region were coming from the sun then the flux would increase with increasing solar activity [26]. So this model has not told us where these cosmic rays come from, rather it tells us where they don't come from, they don't come from our solar system. Determining where cosmic rays do come from is a complex matter. There are a lot of competing theories, but not enough data to prove or disprove many of them.

Above 10^{10} eV and below the knee ($\lesssim 10^{15}$ eV) the most widely accepted theory of acceleration is Fermi acceleration [27] in supernova shock waves. Fermi acceleration involves particles being accelerated as they bounce back and forth between moving magnetic fields. If a magnetic field is strong enough, or large enough, it can act as a magnetic mirror - elastically reflecting charged particles. In the frame of the mirror the cosmic ray always leaves with the same energy as it enters. If the frame of the mirror is boosted with respect to some observer then the frame of the cosmic ray will also be boosted as it is reflected. It's like playing racket ball. When the ball bounces off the wall it is reflected at the same speed that it hit the wall (assuming an elastic collision). When the ball is hit by a player the ball is both reflected and sped up. This acceleration by magnetic mirrors takes millions of years to accelerate cosmic rays. Fermi acceleration in the magnetic mirrors caused by a supernova can explain acceleration up to the knee, and even predicts the slope of the energy spectrum, but cannot account for accelerating particles to greater than 10^{15} eV.

Above the knee ($\gtrsim 10^{15}$ eV) Fermi acceleration is still a possibility, but the magnetic fields making up the mirror must be either much larger, or much stronger, than those that a supernova can create. Pulsars could have strong enough magnetic fields to accelerate cosmic rays past 10^{15} eV and even up to 10^{20} eV [12]. A pulsar is a highly magnetized neutron star with a radius of typically about 10 km and density roughly a 10^{12} times that of the sun. There are pulsars in our Milky Way galaxy, so the cosmic rays accelerated by pulsars could avoid the GZK limit.

What about other theories explaining observations of cosmic rays past the GZK limit? Torres *et. al.* [28] have recently examined the correlation between 7 events above 10^{20} eV and 12 quasar remnants. Quasars are very active galaxies; quasar remnants are dead quasars containing super-massive black holes. Torres discovered a weak correlation between three of the events and some of the quasar remnants. All of the quasar remnants compared were within the 160 million light year threshold of the GZK limit. Another possible theory recently re-examined by Fodor *et.al.* is the possibility that ultra-high energy neutrinos annihilate with relic anti-neutrinos creating Z bosons. The

Z bosons would then decay to fermion anti-fermion pairs which then produce showers of ultra-high energy protons and photons [29] [30]. Relic anti-neutrinos are a predicted result of the Big Bang, similar to the photon CMB. Unlike the CMB, relic anti-neutrinos have not yet been observed. For this theory to predict the flux of ultra-high energy protons observed, the flux of high energy neutrinos needs to be at the present upper limit. Fodor *et. al.* do not present a possible source for the flux of high energy neutrinos.

1.2 Extensive Air Showers

As discussed at the beginning of this chapter extensive air showers (EASs) are cosmic ray air showers that are large enough for the secondary particles to reach the ground. When the secondaries do reach the ground the area and density of the shower front can give a good estimate of the energy of the primary. Higher energy primary particles will produce larger area, higher density, shower fronts. Since the relationship is not a simple one, Monte Carlo simulations are normally used to determine the primary energy from a measured density distribution.

The form of an EAS depends greatly on the type of primary which created it. The two main types of showers are hadronic showers and electromagnetic showers. Hadronic showers are initiated by hadrons (protons and nuclei) while electromagnetic showers are initiated by photons. In principle, electromagnetic showers can also be initiated by electrons and neutrinos, but the flux of primary electrons is very low and the probability of a neutrino interacting in the atmosphere is extremely small. The following two sections will outline some of the basic features of electromagnetic and hadronic showers.

1.2.1 Electromagnetic Showers

The dominant energy loss mechanism for high energy (>10 MeV) photons (γ) is pair production. The process of pair production is the conversion of a photon to an electron-positron pair in the presence of a nucleus, such as an atmospheric nucleus, $\gamma + \gamma \rightarrow e^+ + e^-$. The nucleus is required in the

interaction to conserve momentum; it provides the second γ in the equation. The electron and the positron each get half of the incident photon's energy.

The dominant energy loss mechanism for high energy (>100 MeV) electrons and positrons is Bremsstrahlung radiation loss. In a Bremsstrahlung loss, the electron, or positron, decelerating in the electric field of an atomic nucleus of the medium (air) emits a photon, $e^\pm \rightarrow e^\pm + \gamma$. The emitted photon will then pair produce, the products of that pair production will then Bremsstrahlung, and so on, creating a cascade of electrons, positrons, and photons as shown in Figure 1.7.
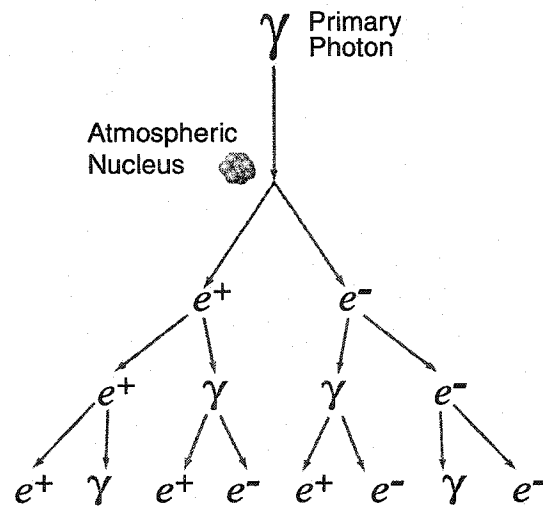
Figure 1.7: Simplified schematic of an electromagnetic shower

The cascade will continue until the pair produced electrons fall below the *critical energy*. The critical energy is the energy at which collision with atoms begin to be the dominant source of energy loss. When this occurs the number of particles in the shower will decrease rapidly, until the shower eventually stops.

Some muons are created in the electromagnetic showers. They are created from the $e^+ + e^- \rightarrow \mu^+ + \mu^-$ interaction when a high energy positron from pair production interacts with an electron of an atmospheric nucleus.

13

1.2.2 Hadronic Showers

Showers produced by protons, neutrons, and nuclei are called hadronic showers. When a high energy hadronic primary interacts with an atmospheric nucleus it produces a more complex shower than the electromagnetic case. Hadronic showers produce many types of high energy particles including: pions, protons, neutrons, kaons, and nuclear fragments. The stable particles go on to have more hadronic interactions, while the unstable particles either decay or undergo more hadronic interactions.

The most common unstable particles produced are kaons and pions. The mean lifetime of a kaon is $\tau_K = 1.2 \times 10^{-8}$ sec. The principal kaon decays produce either pions or muons:

$$K^\pm \to \mu^\pm + \nu \quad (64\%)$$

$$K^\pm \to \pi^\pm + \pi^o \quad (21\%)$$

The number in brackets is the branching ratio of the decay. Charged pions decay into muons $\sim$100% of the time:

$$\pi^\pm \to \mu^\pm + \nu_\mu \quad (\sim 100\%)$$

while neutral pions predominantly decay into photons;

$$\pi^o \to \gamma + \gamma \quad (99\%)$$

Pions also decay very quickly, $\tau_{\pi\pm} = 2.6 \times 10^{-8}$ sec and $\tau_{\pi^o} = 8.4 \times 10^{-17}$ sec, so neither pions nor kaons are observed in showers near sea level. All of this means that almost all of the pions and kaons produced in the shower will decay to muons before reaching the ground.

You can see that hadronic showers make *lots* of muons. Relativistic muons can live long enough to reach the ground. Even though traveling through 10 km of atmosphere at c requires 3.3×10^{-6} sec (longer than their mean lifetime $\tau_\mu = 2.2 \times 10^{-6}$ sec), relativistic time dilation allows the muons to live longer in the Earth's rest frame than their own. Muons do not interact via the strong force (the force that holds a nucleus together). When they pass

through matter, the dominant interactions are electromagnetic interactions with electrons. Since muons are 200 times heavier than electrons, the situation is similar to throwing a baseball into a room full of house flies; the flies don't do much to slow the baseball down. Muons are very penetrating, they will pass several kilometers into the Earth without slowing very much. Muons predominantly decay to an electron and some neutrinos;

$$\mu^{\pm} \to e^{\pm} + \nu_e + \nu_{\mu} \ (98.6\%)$$

The electrons and photons produced by the decay of muons, pions, and kaons, will go on to create small electromagnetic sub-showers within the hadronic shower. Since the products of hadronic interactions are much heavier than the electromagnetic components of the shower, there will be a hadronic core in the center of a hadronic shower with electromagnetic sub-showers spreading out from the core, as shown in Figure 1.8.
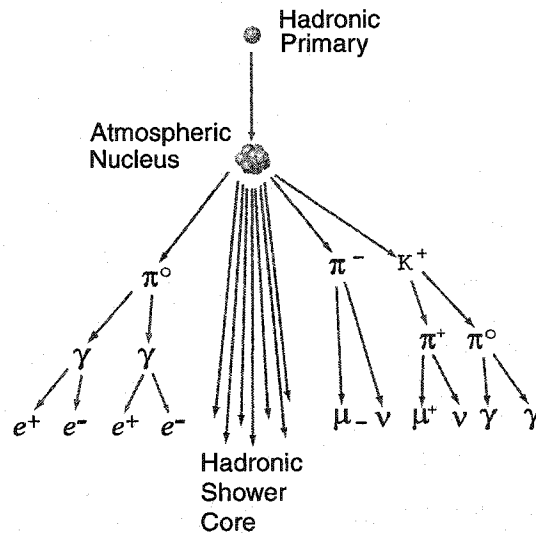
Figure 1.8: Simplified schematic of a hadronic shower

By the time the shower gets to ground level there is usually very little hadronic matter left in the shower as it has all interacted to produce photons, electrons, and muons. A very significant difference between hadronic showers and electromagnetic showers is the ratio of muons to other particles. Hadronic showers have a much higher ratio of muons than electromagnetic showers. This

detail will come up in the next section when we talk about non-random cosmic ray phenomena.

1.2.3   Other Shower Phenomena

Apart from the secondary particles of the air shower itself, there are two other physical processes that can be useful in the detection of cosmic ray air showers: Cerenkov radiation and nitrogen fluorescence.

Cerenkov Radiation

When charged particles pass through a medium faster than the speed of light in that medium, Cerenkov radiation is produced. Cerenkov radiation is the light equivalent of a sonic boom. When a jet flies through the air it causes the surrounding air molecules to oscillate. If the jet is moving faster than the speed of sound (the speed that those oscillations can propagate in air) then the oscillations will be able to constructively interfere, causing huge oscillations of the air molecules; a sonic boom. When a charged particle passes
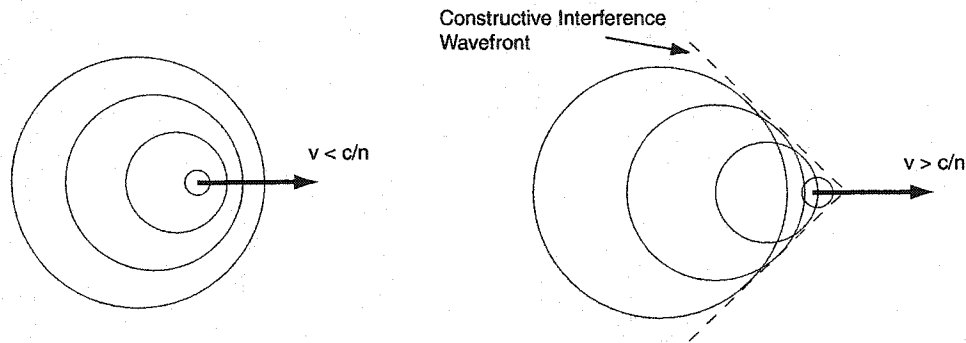
Figure 1.9: Schematic of a sonic boom or Cerenkov radiation

through a medium it polarizes the atoms as it passes them. The atom then quickly depolarizes, producing an electromagnetic wave. If the next atom in the path of the charged particle is polarized and depolarized before the wave from the previous atom reaches it then the two electromagnetic waves will be able to constructively interfere. Since the electromagnetic wave travels at the speed of light in the medium (c/n), if the charged particle travels faster than c/n than the next atom will be polarized and depolarized before the

16

electromagnetic wave reaches it. The constructive interference produces an observable electromagnetic wave which is the Cerenkov radiation, as shown in Figure 1.9.

When high energy charged particles of a shower pass through the atmosphere they produce Cerenkov radiation. Observing the Cerenkov radiation is one way of detecting air showers; even if the shower does not reach the ground, the Cerenkov photons might. So, Cerenkov radiation is a good way to detect air showers in the lower end of the energy spectrum.

Nitrogen Fluorescence

When an electron passes through a gas it excites atoms along the way, which then de-excite, emitting photons. This is the phenomena behind Cathode ray tubes, neon lighting, and the Aurora Borealis[2]. Nitrogen fluorescence is the same physical process. In the context of cosmic ray air showers it happens when a high energy secondary charged particle passes through the atmosphere exciting atmospheric atoms and molecules along the way. Since nitrogen is the most abundant element in the atmosphere, the phenomenon is called nitrogen fluorescence.

The amount of nitrogen fluorescence is proportional to the number of charged particles in the air shower. If you can observe the amount of nitrogen fluorescence along the path of the shower then you can determine where the shower reached its maximum number of secondaries. This is useful because heavier primaries penetrate deeper into the atmosphere before reaching their shower maximum, so the mass of the primary cosmic ray can be estimated.

1.3   Non-Random Cosmic Rays

It is generally believed that cosmic rays arrive at Earth randomly in time. However, there have been several experiments which show that there could be components of the cosmic ray spectrum that have non-random arrival times.

---

[2]The Aurora Borealis is created when solar wind electrons enter the ionosphere. They emit most commonly in the oxygen spectra at high altitude, but nitrogen emission lines can be seen if the electrons penetrate deep enough into the atomosphere.

Several different patterns have been observed, but none have been consistent enough to draw any definitive conclusions about their cause. The following sections describe two different, but possibly related, non-random phenomena that have been observed.

1.3.1 Cosmic Ray Bursts

During the analysis of a Cerenkov telescope experiment in 1980 Bhat *et. al.* [7] found an overall excess of events with time separations < 40 s. A histogram of the time difference between sequential showers required two exponential functions to fit; not one, as expected. One experiment, Badino *et. al.* [31], found a similar excess, while two other experiments, Smith *et. al.* [32] and Fegan *et. al.* [33], could not detect any such excess of showers < 40 s apart in the overall air shower arrival time spectrum.

In 1983 Fegan and Smith each published papers observing a slightly different phenomena. They both observed short term increases in the rate of the cosmic ray flux; cosmic ray bursts. Smith [34] observed a burst which occurred on January 20, 1981 at the Manitoba Air Shower Array. The array was composed of three 1 m^2 scintillator detectors in a triangle with 12 m sides. The array operated from October 1980 until April 1982, observing a total of roughly 150 000 showers with an estimated mean energy of 3×10^{15} eV. The average count rate being about 0.2 events/min. Beginning at 17:25 (local sidereal time) on January 20 a series of 32 showers were detected in a 5 minute interval. With an average event rate of 6.4 events/min (that's over 30 times the average count rate) the burst had a statistical probability of approximately 10^{-32}. This was the only burst observed in the lifetime of the experiment.

The Fegan [5] burst published in 1983, observed on February 25 1975, was observed at two stations simultaneously. The two stations were 250 km apart (in Dublin and Cork Ireland) and had relative timing accuracy of 1 ms. Each station consisted of four 1 m^2 scintillation counters, positioned to produce a lower limit on shower energy of 10^{14} eV. The system was operational from January 1975 until December 1977, a total of 807 days. The event of February 25 lasted 20 seconds. There was a 1.7-fold increase in the rate over the 20

second period. It was the only event of its kind observed in the 807 days of operation and had a calculated probability of 2.7×10^{-5} of being a statistical fluctuation.

The authors of both papers speculated on the possibility of these bursts being initiated by very high energy photons in a γ-ray burst (GRB). However, there is no definitive evidence that GRBs contain photons with enough energy to create an electromagnetic extensive air shower. GRBs are bursts of gamma-rays lasting anywhere from milliseconds to tens of minutes. The sources of GRBs are not yet known, as their arrival directions seem to be completely isotropic. For a review of present GRB knowledge see [35].

The biggest piece of evidence contradicting the GRB hypothesis was that the Vela satellite system did not detect a GRB at the time of either burst. The Vela satellite system was a U.S. military constellation of 4 satellites used to detect the γ emissions from nuclear detonations so that they could monitor nuclear testing and activity around the world. Nobody knew that GRBs existed when the millitary launched the constellation. They discovered that all 4 satellites would simultaneously detect γ-rays for no apparent reason. The Vela satellite system had accidentally discovered GRBs. While the Vela satellites were only capable of detecting gamma-rays up to 1.5 MeV, one could expect a high energy gamma-ray burst to be accompanied by a low energy tail.

More evidence suggesting that these cosmic ray bursts were not caused by GRBs came in 1998 from the Mitsuishi air shower array, Katayose *et al* [36]. The Mitsuishi air shower array is an array of 16 $1m^2$ scintillation detectors and an underground muon detector located near Mitshuishi, Japan. The muon detector has four layers of proportional chambers, so muon direction can be determined. The array covers approximately 2000 m^2 and has been in operation since 1961. 3.6 million events with estimated mean energy of 1.1×10^{15} eV were collected from January 1989 to October 1996 and were examined for periods of elevated count rates. Five such periods were found with probabilities less than 5×10^{-2}. The elevation in count rate occurred for different lengths of time, between 20 minutes and 40 hours, for each period. The evidence against the theory that GRBs caused these bursts is that there

was no decrease in the muon component of the burst showers, when compared to the 'ordinary' showers. As discussed in Section 1.2 a significant decrease in the density of muons is expected for showers produced by photons.

Recently, the LAAS (Large Area Air Shower) group in Japan analysed the arrival direction of roughly 1 million successive air showers [37] [8]. They seemed to see that the higher the rate of successive events the more the arrival directions correlated to the galactic plane. If there is a correlation pointing to the galactic plane, that would mean that the primaries causing the successive air showers could not have any charge. If they were charged, their paths would have been deflected by the galactic magnetic field.

The cause of these rarely observed cosmic ray bursts is still unknown. Even the question of their existence remains debated. Have the observations been simply random chance? With the low probability of the Fegan event and the very low probability of the Smith event, it seems very unlikely that the events are random chance. However, the only way to find out for sure is to perform additional observations using as many experiments and techniques as possible.

1.3.2 Correlated Cosmic Rays

Another non-random phenomenon in question is correlated cosmic ray air showers. The search for correlated cosmic ray showers is the primary objective of the ALTA experiment. A correlated air shower event could be created by the same processes that provide non-random events, or possibly a cosmic ray interaction that occurred far outside the Earth's atmosphere and produced a shower of particles hitting the atmosphere, as shown in Figure 1.10.

We've already seen one possible example of a pair of correlated events - the burst observed by Fegan *et al* [5] was observed at two stations simultaneously, 250 km apart. Unfortunately, the Fegan *et. al.* experiment did not have the directional information to determine if the events were arriving from the same direction. The only directional information they had was the field of view of the detectors at the time of the event.

In 1994 Carrel and Martin [3] published an observation of another possible correlated cosmic ray event. Carrel and Martin's detector consisted of four

Interaction creating
correlated primaries
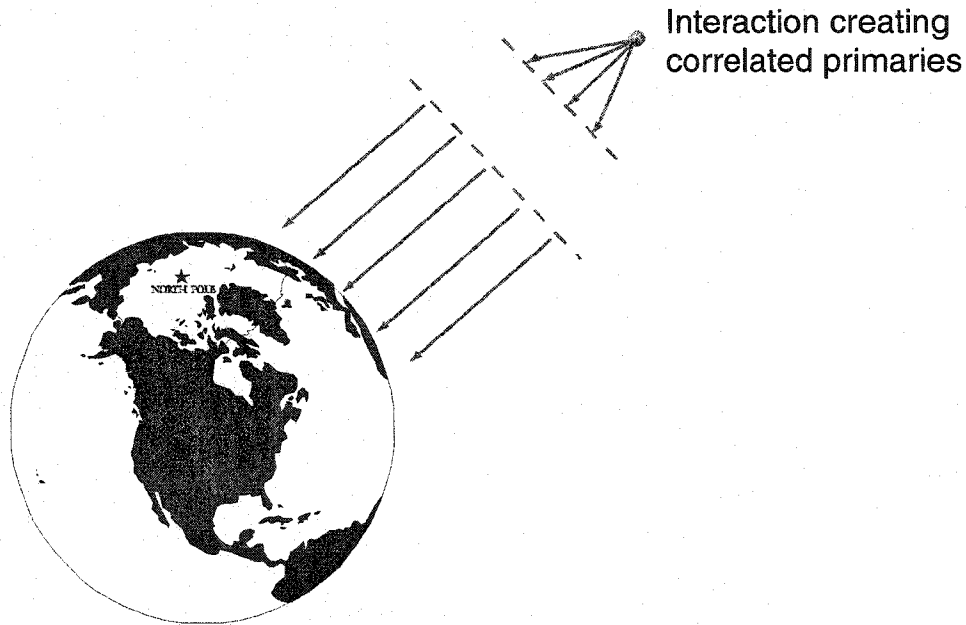
Figure 1.10: Hypothetical event creating correlated showers

sites, between 50 and 186 km apart, with 3 units of 3 stacked scintillators at each site. There was a 10 cm layer of lead between two of the scintillators to distinguish between muon and electron events. The potentially correlated event occurred between December 15th and December 22nd 1991, and consisted of a 4.8σ excess of quadruple electron hits over the expected random coincidences. A quadruple electron hit was defined as a signal in all four sites in the electron component of the detectors within 0.62 ms (0.62 ms is the light travel time for 186 km). The event was not observed in the muon component of the detectors. This implies that it was most likely caused by a photon primary. The probability of this excess being a statistical fluctuation was calculated to be less than 10^{-4}. The Carrel and Martin detector was not able to determine the direction of a shower incident on a site. This information could have provided valuable insight into the nature of the observed excess, and would have been instrumental in determining if the showers at the different sites were actually correlated.

Inspired by the Carrel and Martin observation, the LAAS group analysed 4 years of data for possible correlated showers [4]. Of the 2.6 million events analysed one pair of events produced a possible correlation. The two events

had a time difference of only 195 μs and occurred in stations 153 km apart. The arrival angles of the events matched within the angular accuracy of the arrays. The chance probability of this event was 0.16. Because the Crab Nebula was within the angular accuracy of the events, the LAAS group hypothesized that the event was caused by ultra-high energy gamma-rays from the Crab. Other physical processes that could create correlated showers include the disintegration of cosmic dust grains and a process known as the GZ effect.

GZ Effect

The GZ effect was first proposed by Gerasimova and Zatsepin [38], [39] in the 1950's. The effect was re-examined in a paper by A.A. Watson and G.A. Medina-Tanco in 1999 [40]. The GZ effect is the process of a heavy cosmic ray nucleus colliding with a solar photon and fragmenting, or photodistingrating, thereby producing fragments that could initiate extensive air showers on Earth. The most probable fragmentation is to a single nucleon and remainder of the nucleus. The fragments would be separated by the interplanetary magnetic field due to their difference in charge and mass. If both fragments hit the Earth, the air showers would be correlated in time and arrival angle. Figure 1.11 [40] shows some of the results of the Watson and Medina-Tanco work. In the figure the contour lines are the logarithm of the median separation of the air showers on Earth (in km), the shaded regions show the ratio of GZ events to unperturbed cosmic ray flux of Fe nuclei at 6×10^{17} eV, and the plot at the bottom shows a cross-section of the shaded regions with ϕ=0 being the direction of the sun.

It is clear from the figure that the highest flux of GZ events come from the direction of the sun with a flux ratio of $10^{-3.2}$. Unfortunately, these are also the most widely spaced showers with a median separation of around 1000 km. A median separation of about 100 km is found on the night side of the Earth, but here the flux ratio has gone down to $10^{-4.8}$. To make an estimate of the flux of GZ events Watson and Medina-Tanco used an incident Fe flux of $3.8 \times 10^{-12}\mathrm{m}^{-2}\mathrm{s}^{-1}\mathrm{sr}^{-1}$. Flux ratios of $10^{-3.2}$ and $10^{-4.8}$ would produce fluxes
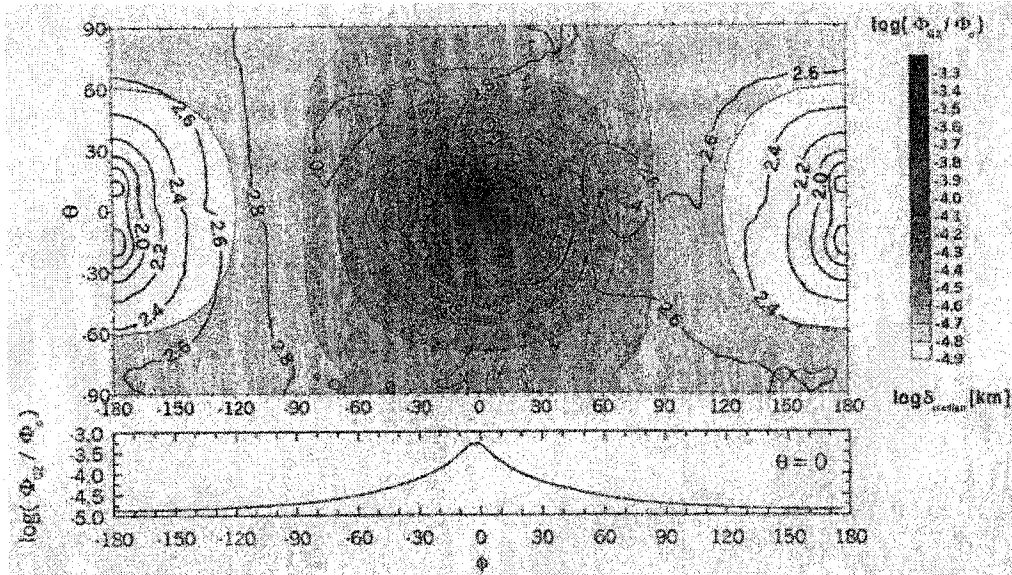
Figure 1.11: Fraction of GZ events for Fe nuclei at 6×10^{17} eV in ecliptic coordinates with the direction of the sun at the center of the plot.

of approximately 1500 and 40 GZ showers per year on 100 km^2. These seem like measurable fluxes, but remember, to detect a GZ event the experiment must detect both showers that are around 100 to 1000 km apart.

Another complication in the detection of the showers is the relative shower size. The most probable products of photodisintegration are a single nucleon and a nucleus with the remaining nucleons. So, if a 6×10^{17} eV Fe nucleus were to photodisintegrate into two fragments, the resulting showers would most likely carry 1/56 and 55/56 of the original energy, with the smaller shower being on the order of 1×10^{16} eV. For an array like the Pierre Auger Project (see Section 1.4), with an area of 3000 km^2 and a detector spacing of 1.5 km, the smaller shower would probably not even be detected as a shower, since it would not be large enough to hit more than one of the detectors.

Dust Grain Disintegration

Cosmic dust grains have long been considered a remote candidate for the originators of the largest air showers. Even recent studies show that there is a small possibility that the observed showers above 10^{19} are relativistic dust grains [41]. Berezinskiy [42] showed that as relativistic dust grains propagate

through the CMB and solar photon fields they gain charge as electrons are stripped from their surface. The dust grain will eventually disintegrate due to the large electrostatic forces caused by the build-up of charge. Dust grains with Lorentz factors greater than 30 disintegrate "especially effectively" [42] on solar photons within the solar system. If a relativistic dust grain were to disintegrate in the solar photosphere it would cause a shower of smaller dust grains that could be the originator of correlated cosmic ray air showers.

1.4 Cosmic Ray Experiments

In the century that physicists have been trying to unravel the cosmic ray mystery they have devised many different techniques to detect cosmic rays. The purpose of this section is to describe the basic techniques that are used today and present some of the experiments currently employing these techniques.

There are two basic types of experiments; direct detection experiments and ground based experiments. Direct detection experiments are high altitude balloon and space craft experiments that depend on the primary cosmic ray interacting directly with their detector. These experiments can determine the energy and composition of the primary cosmic ray with high accuracy. The disadvantage of these experiments is their size limit (they need to fit on a space shuttle or high altitude balloon). Since the flux drops exponentially with increasing energy, this small size (and mass) prevents them from detecting a significant number of high energy cosmic rays. Balloon experiments like JACEE are exploring cosmic rays with energies up to 10^{16} eV [43].

Ground based experiments[3] do not directly detect the primary cosmic ray, they detect some component of the air shower that was initiated by the primary. The three major components currently exploited are; Cerenkov radiation, nitrogen fluorescence, and the secondary particles of the air shower (see Section 1.2 for more about these processes).

---

[3]I use the term 'ground based' loosely to mean any experiment whose apparatus is located near the surface of the Earth. They could be underground or underwater.

Detectors that use Cerenkov radiation are called Cerenkov telescopes and Cerenkov arrays. STACEE [44] (Solar Tower Atmospheric Cerenkov Effect Experiment) is a Cerenkov array that uses a solar power testing facility in New Mexico. The solar power facility is an array of mirrors which can be controlled to focus to a point on top of a large tower nearby. A Cerenkov telescope like HEGRA [45] (High Energy Gamma-Ray Astronomy) images the Cerenkov light in a light collecting dish. Pictures of both experiments are shown in Figure 1.12.
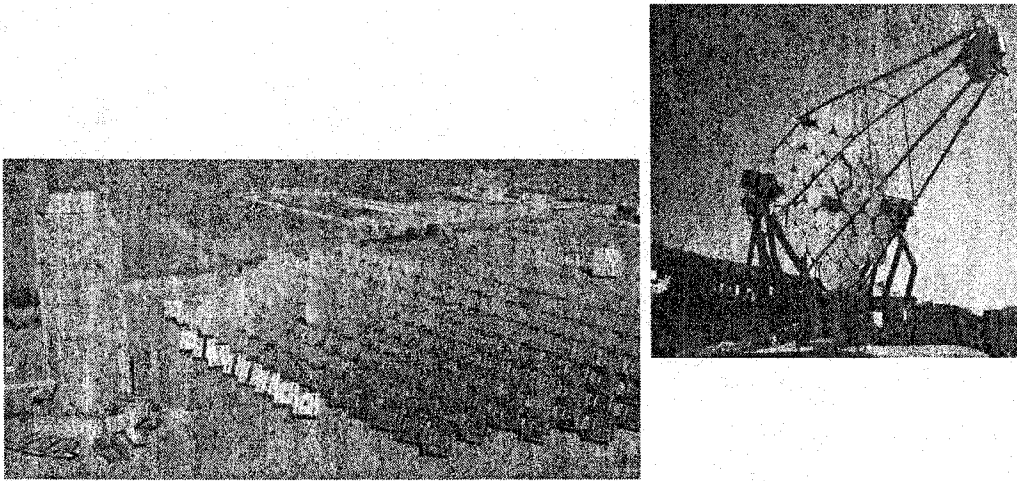
Figure 1.12: Photograph of the STACEE (left) and HEGRA (right) facilities

On clear moonless nights Cerenkov detectors can point toward sources of interest and gather information about the cosmic rays they produce. Cerenkov detectors excel at detecting photon primaries in the GeV and TeV energy range.

Experiments like HiRes (also known as Fly's Eye) look for streaks of nitrogen fluorescence in the night sky. The HiRes detector is basically a pair of hemispherical structures covered with mirrors that point outward, to the sky. Each mirror is monitored by several PMTs. The two 'eyes' of the HiRes detector allow for position resolution of the shower, as shown in figure 1.13.

The biggest advantages of a detector like HiRes is the huge area monitored and the ability to produce a plot of the longitudinal development (number of particles in shower as a function of depth in atmosphere). A plot of the longitudinal development can be used to estimate the mass of the primary
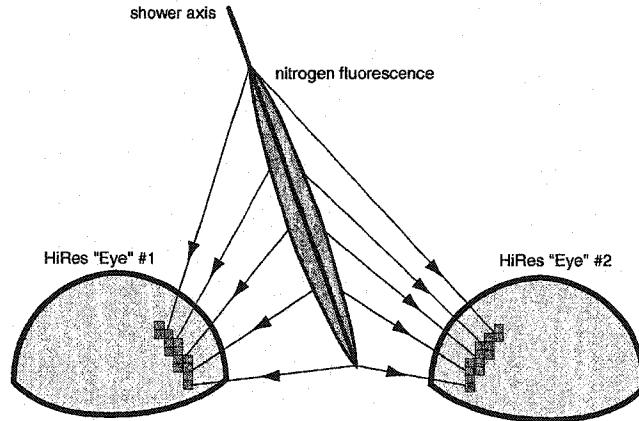
Figure 1.13: Diagram of a high energy cosmic ray event at HiRes

particle because heavier particles develop deeper in the atmosphere. Fly's Eye lays claim to the highest energy cosmic ray ever observed at 3×10^{20} eV [23].

A third type of ground based detector uses the distribution of secondary particles in the air shower to extrapolate primary particle information. In general, the larger the area covered by the footprint of the shower front, the larger the energy of the primary. By putting particle detectors in large arrays on and under the ground the size and density distribution of a shower front can be measured. With detectors placed underground, or under thick lead shields, the fraction of muons in the air shower can be determined. The muon fraction information can distinguish electromagnetic showers from hadronic showers.

AGASA (Akeno Giant Air Shower Array) is currently the largest air shower array. The array covers an area of 100 km^2 with 111 scintillator electromagnetic detectors and 27 shielded scintillator muon detectors. On December 3, 1993 they observed the second highest energy cosmic ray ever observed at 2×10^{20} eV [46].

The next generation in the evolution of the ground based cosmic ray detector is a hybrid detector called the Auger project [47]. The experiment is named in honour of Pierre Auger who discovered extensive air showers back in 1939 [48]. The Auger project will have two sites, one in the northern hemisphere (Utah) and one in the southern hemisphere (Argentina). Each site will have an area of 3000 km^2 and contain an array of 1600 Cerenkov water tanks and a nitrogen fluorescence detector. The site in Argentina is currently under

construction.

A cosmic ray experiment that is actively searching for correlated cosmic rays and non-random arrival time series is the Large Area Air Shower (LAAS) group in Japan [49]. The LAAS group consists of 9 stations of scintillator arrays. The stations vary primarily in the number of scintillation detectors, but most stations have about 5 detectors, ($50 \times 50 \times 5$ cm^3) each. The estimated mean energy of observed air showers is $(3\text{-}5) \times 10^{14}$ eV. Most stations are roughly 100 - 200 km apart and equipped with GPS for relative timing.

At the 2001 ICRC Villasenor *et. al.* [50] presented a plan for an international collaboration of cosmic ray detectors to search for time correlations and GRBs in cosmic ray air showers on an international scale. The plan includes the Chacaltaya (Bolivia), Cerro la Negra (Mexico), Auger (Argentina), and Milagro (USA) air shower arrays. The Cerro la Negra and Auger arrays are still under construction, while the Chacaltaya and Milagro arrays are currently in operation.

While the LAAS group's objectives are similar to the ALTA project, this new proposal's objectives are complimentary to the objectives of the NALTA (North American Large Area Time Coincidence Array) [10] collaboration. The NALTA collaboration is a group of ALTA-type experiments spread throughout North America. The NALTA collaboration currently includes: ALTA (Alberta, Canada), CHICOS (California, USA), CROP (Nebraska, USA), SALTA (Colorado, USA), and WALTA (Washington, USA). Locations in the development and planning stages include: Boston (USA), Mexico City (Mexico), Montreal (Canada), Morelia (Mexico), Ottawa (Canada), Puebla (Mexico), Vancouver (Canada).

Chapter 2

ALTA Systems

The purpose of this chapter is to discuss the apparatus of the ALTA experiment. Section 2.1 contains an overview of the system and its components, and the remainder of the chapter contains details of those components.

2.1 Overview

The goal of ALTA is to look for correlations and non-random time series in cosmic ray air showers. To accomplish this broad goal the experiment must be flexible and adaptable. The ALTA experiment is composed of many self-contained sites, spread throughout Alberta. Each site contains three scintillation detectors placed in the corners of an equilateral triangle of 10 m per side, an electronics crate to determine coincidences and energy loss information, a GPS antenna and receiver, and a PC with a software program to operate the electronics and temporarily store data from that site. Figure 2.1 is a basic schematic of the components of an ALTA site. Much of ALTA's flexibility comes from the fact that each site operates independently.

There are presently 6 operational sites. Figure 2.2 is a map of the sites in operation and those currently under construction. The sites are referred to by their name and/or site number, both of which are listed in the legend of Figure 2.2.

Each site is capable of detecting an Extensive Air Shower (EAS) with a minimum energy of about 10^{14} eV, pointing to the arrival direction of that shower within roughly $\pm 7°$, and timing the event relative to other ALTA sites
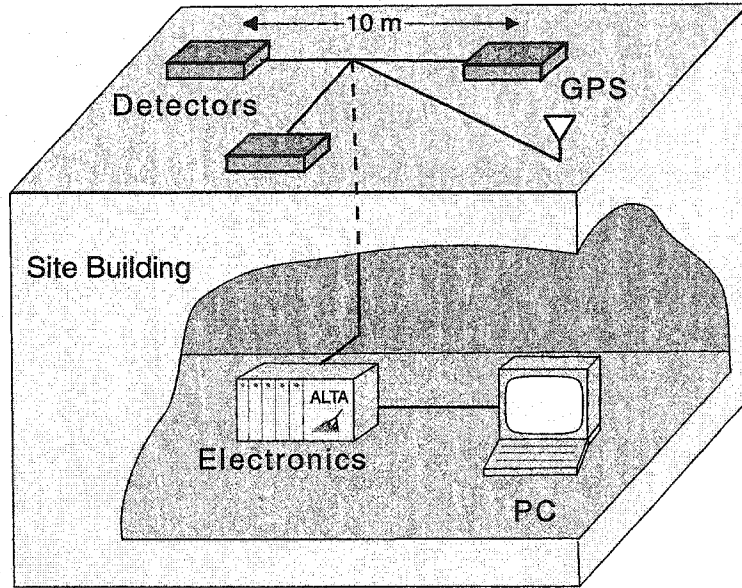
Figure 2.1: Basic schematic of ALTA system components

within about 16 ns (see Chapter 3 for more details on the energy, angle, and time resolution). Events from each site are recorded on the local site PC until they are downloaded, every night, to the central database at the University of Alberta. Each event contains the information necessary to determine when the event occurred, the arrival angle of the event, and a rough estimate of the density of the shower front.
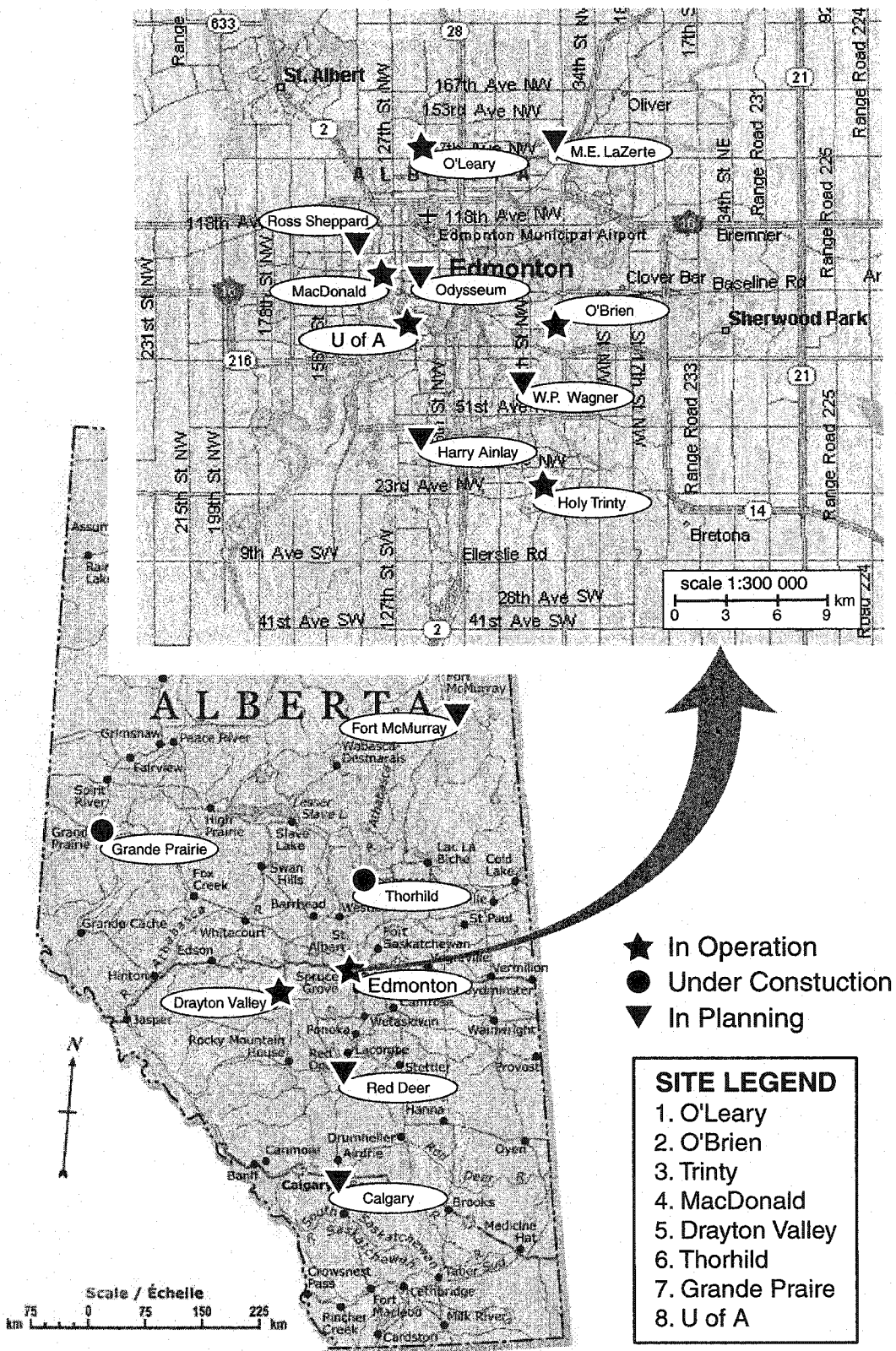
Figure 2.2: Map of ALTA sites currently in operation and under construction

The remainder of this section contains a synopsis of how the system attains all this information about an air shower. To simplify the explanation of how the arrival direction of the shower is determined in 3 dimensions, I'll use a 2-dimensional example. The 2-dimensional case is shown in Figure 2.3. If an air
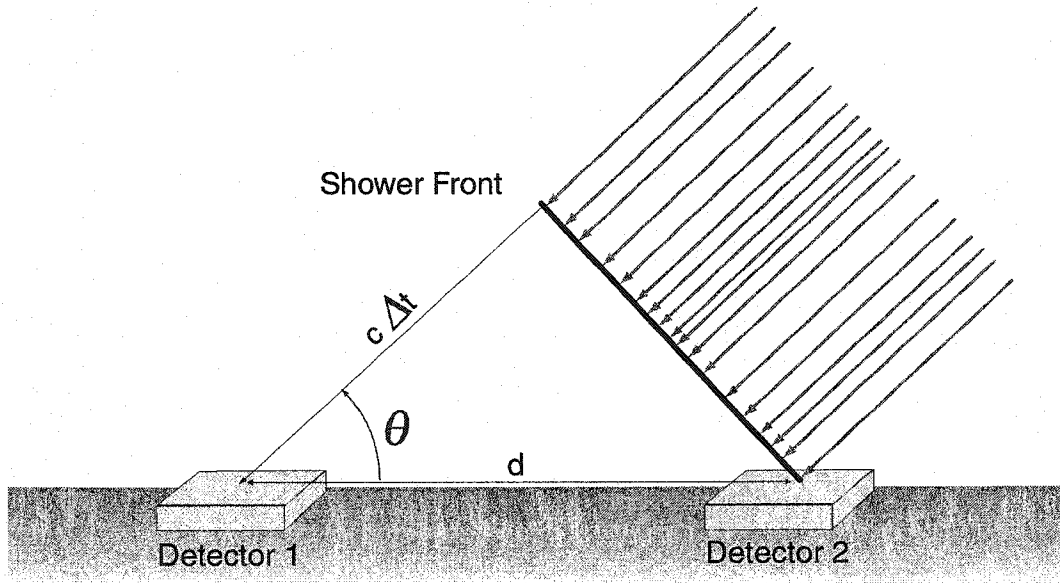
Figure 2.3: Schematic of determining shower arrival direction in 2 dimensions

shower hits a detector Δt seconds after hitting a detector d meters away, then the arrival angle can be calculated simply with the definition of the cosine.

$$cos\theta = \frac{c\Delta t}{d}$$

This requires three assumptions:

1. the shower front is planar

2. the shower front is traveling at c

3. the shower front is perpendicular to the shower axis

The electronics crate determines the relative arrival time of the shower front and the location of the detectors relative to each other is easily measured. In 3 dimensions the process is called *triangulation*, and 3 detectors are required. The details of the triangulation calculation are slightly more complex than the 2-dimensional case and are explained in Section 4.2.4.

Next, to determine the absolute arrival time of an event the GPS receiver and antenna are used. The GPS system is also used to determine the positions of the ALTA sites relative to each other. Details of the GPS system are discussed in Section 2.3.

You may have noticed that there are two time scales in this experiment; the relative time of arrival of the shower front on the detector triangle, and the absolute time reference used to compare sites to each other. To keep these clear, the term *local timing* will be used when referring to the relative timing in the detector triangle, and *global timing* when referring to the GPS timing between different sites.

The last major piece of information is the energy of the shower. To determine the shower energy with a ground based scintillation detector you need to determine the density of secondary particles as a function of distance from the shower axis. To get an estimate of how many particles passed through the detector (and hence an estimate of the particle density) the ALTA electronics crate determines the energy deposited in the scintillation detectors (see Section 3.1). But there are only three detectors at each site. This seriously limits the sample area for determining the shower's density distribution and means that all we can do is put a lower limit on the shower's energy. The lower limit of the shower energy is determined by finding the smallest energy that could reasonably fire all three detectors in the 10 m equilateral triangle using computer simulations. The energy limit for an ALTA detector is shown to be 10^{14} eV in Section 3.2. Correlations between sites by analysis of the GPS global times would indicate a much higher minimum energy or a physical process that generates correlated air showers.

So, in summary, the ALTA experiment is composed of many independent cosmic ray air shower detectors, each capable of determining the shower's arrival time and direction. The data will be searched in an effort to find non-random phenomena in the arrival of cosmic rays at different sites. The rest of this chapter contains the details of each of the components making up an ALTA site.

2.2 The Detectors

All of the ALTA detectors are composed of plastic scintillator viewed by a photomultiplier tube (PMT). A scintillator emits a small flash of light when a secondary cosmic ray passes through it and the PMT turns that flash of light into an electrical signal. The PMT signal is then sent to the electronics crate. The scintillator and PMT are both sensitive to their external environment so they need to be weather-proofed for operation on the roof of a building. To weather-proof the detectors we enclose them in water-tight, insulated wooden boxes that we call 'doghouses'. Inside each doghouse there is a temperature sensor, a temperature controller, and a strip of heater tape. The sensor turns the heater tape on when the temperature inside the doghouse drops below 0°C. The tape is turned off when the temperature rises above 10°C. This prevents the temperature in the doghouse from going below approximately -10°C.

The detectors are also equipped with an LED (Light Emitting Diode) to make sure that the PMTs are still working properly. The LED is glued into the scintillator plastic and can be pulsed at intervals that are controlled by the user via the calibration module in the electronics crate.

On the scale of most present day cosmic ray research ALTA is a fairly low cost experiment. We have benefitted greatly from the generosity of companies and other experiments. This has resulted in three different types of detector. All of the detectors installed thus far, except the one on the University of Alberta campus, are Bicron BC-408 plastic scintillator. The OPAL experiment (at CERN) has also donated 78 scintillator tiles and 48 photomultiplier tubes that will be used when all of the BC-408 scintillator has been used. Each of these detectors will be discussed in the following sections.

2.2.1 The Bicron Detectors

The ALTA detectors made from the Bicron donation are sheets of plastic scintillator that are 60 cm × 60 cm × 1 cm (detection area = 0.36 m^2). Figure 2.4 is a diagram of one of the Bicron detectors.

Bicron's BC-408 plastic scintillator is designed for fast counting, large area
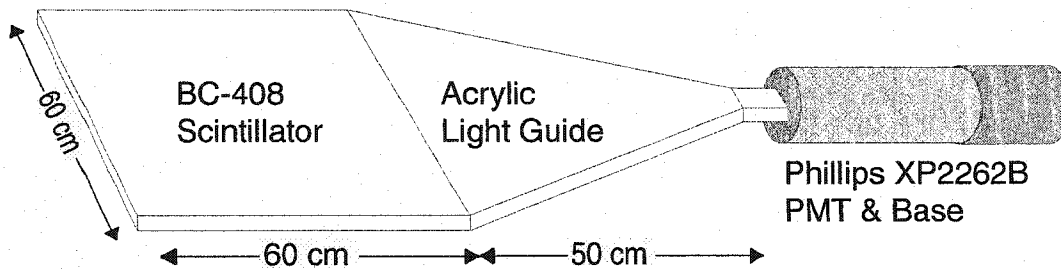
Figure 2.4: Basic schematic of bicron detectors.

detectors. With a signal rise time of 0.9 ns, and an attenuation length of 2.1 m [51], the BC-408 has timing and attenuation characteristics suitable for the experiment. The scintillators are connected to 2" Philips XP2262B photomultiplier tubes (PMT) via a triangular acrylic light guide. The XP2262B tubes are 12 stage tubes with a suggested maximum operating voltage of 2500 V. The tubes are operated between 1900 and 2100 V, a gain of about 10^7.

The emission spectra of the scintillator and the spectral sensitivity plot of the Philips PMT are shown in Figure 2.5 [51] [52]. You can see the emission spectra maxima matches the spectral sensitivity maxima at about 425 nm, the blue part of the spectrum.
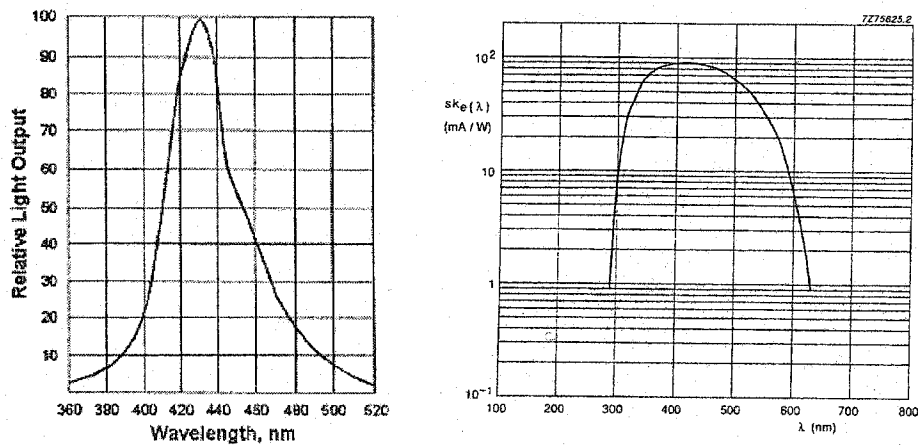
Figure 2.5: (a) Emission spectra of Bicron BC-408 plastic scintillator and (b) spectral sensitivity of Philips XP2262B PMT.

The efficiency of the Bicron detectors was examined with the setup shown in Figure 2.6. The trigger detectors used were made of 1 cm × 5 cm × 5 cm pieces of BC-408 scintillator coupled by optical grease to the face of a Philips
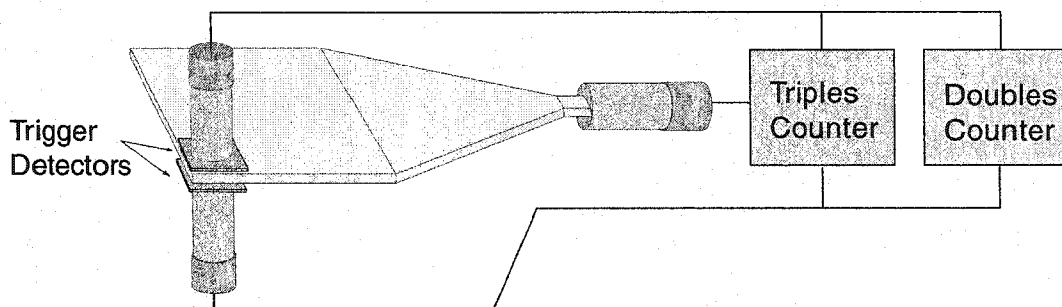
Figure 2.6: Experimental setup to test the efficiency of Bicron detectors

XP2262B PMT. The efficiency of the ALTA detector was determined by requiring a double coincidence between the trigger detectors and then comparing to see if a triple coincidence was also observed. The number of triples observed in the time that 100 doubles are observed is the efficiency that is shown in Figure 2.7.
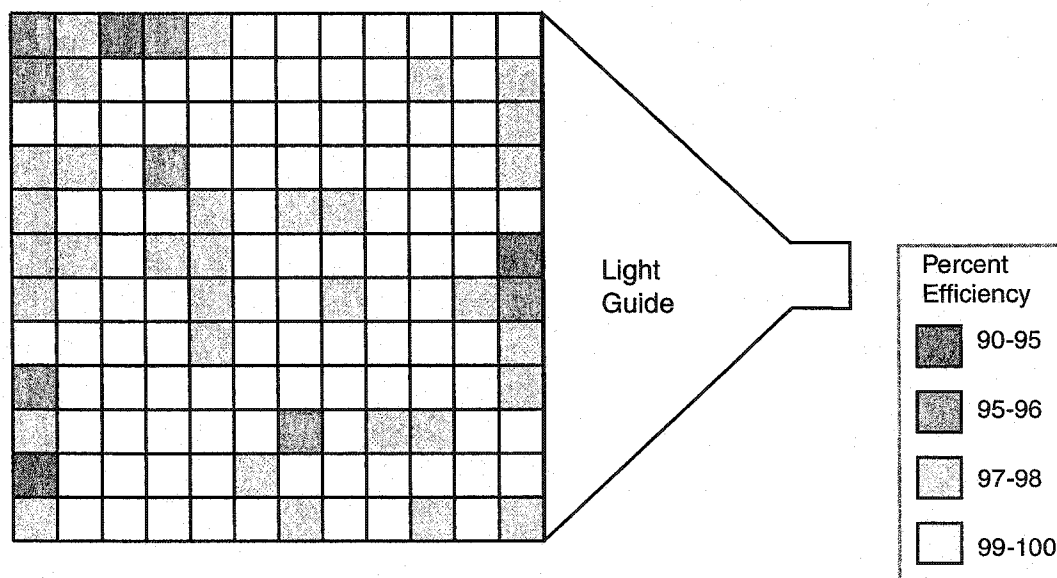
Figure 2.7: Typical results of the dependence of efficiency with position on the Bicron detectors

The Bicron detectors are currently installed at O'Leary, MacDonald, Drayton Valley, Holy Trinity, and O'Brien high schools. Bicron detectors are planned for installation at high schools in Grand Prairie, and Thorhild.

35

2.2.2 The OPAL Detectors

The OPAL detectors are composed of plastic scintillators with embedded wave-shifting fibers. Optical fibers are used to couple the wave-shifting fibers to the PMT. Figure 2.8 is a diagram of an OPAL scintillator.
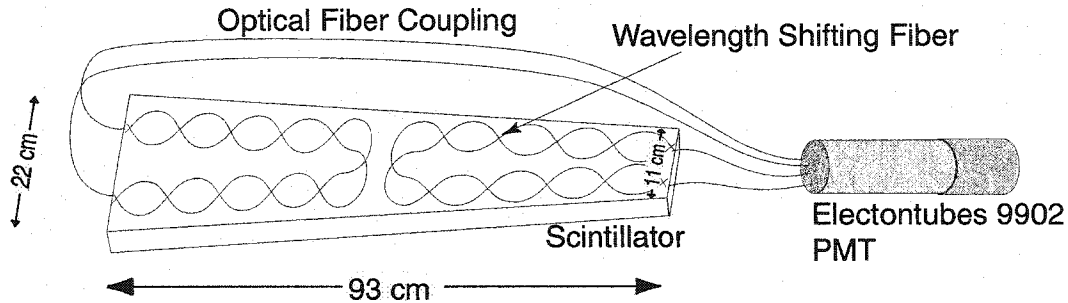
Figure 2.8: Diagram of an OPAL detector. Detection area is 0.16 square meters

Along with the scintillator tiles the OPAL experiment also donated 56 ElectronTubes 9902 PMTs. The 9902 series PMTs are 10 stage tubes with a maximum 1800 V recommended operating voltage. They are smaller than those used with the Bicron detectors, with a 1.5" diameter window. The OPAL PMTs were chosen by the OPAL collaboration to match the light output of the wave-shifting optical fibres. The fibers emit in the green part of the visible spectrum and the 9902 series PMTs are produced for green sensitivity. Figure 2.9 [53] shows a plot of the quantum efficiency of the PMT as a function of wavelength. While you can see the peak is not in the green part of the spectrum, the quantum efficiency is still around 15-20% at 500 nm.

The OPAL detectors have roughly half the detection area (0.16 m^2) of the Bicron detectors, so two OPAL detectors will be coupled to one PMT. Efficiency tests for the OPAL detectors have not yet been completed.

2.2.3 The U of A Detectors

The site on the U of A campus has detectors that were donated by the National Research Council. Figure 2.10 is a diagram of the U of A detectors.

The U of A scintillators are roughly 100 cm × 100 cm × 2 cm. They are diffusing scintillators with light attenuators placed on top of them. The inside
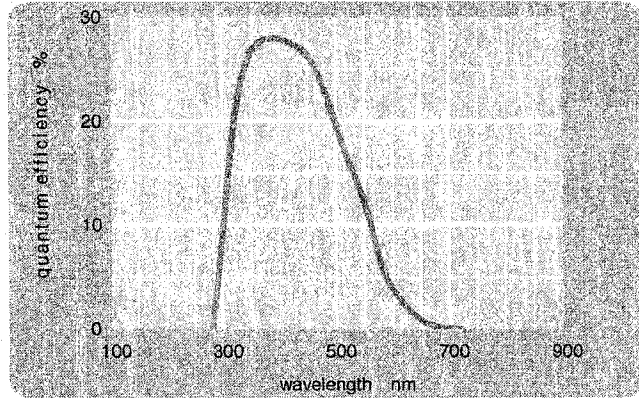
Figure 2.9: Plot of spectral sensitivity of Electrontubes 9902 PMT
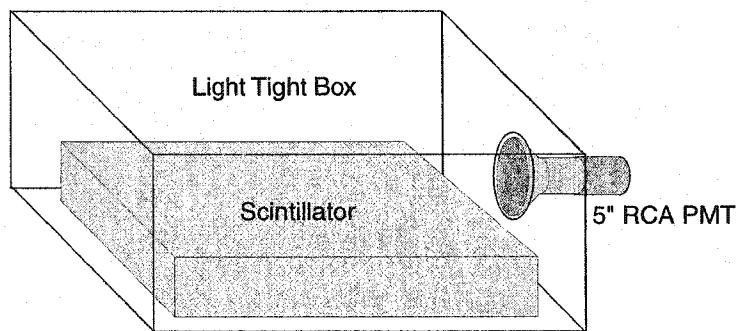
Figure 2.10: Diagram of U of A detectors

of the box is painted with reflecting paint. We do get a larger count rate and better energy loss resolution at the U of A site due to the larger size of the detector.

2.3 Global Positioning System

The purpose of this section is to review the basics of how the Global Positioning System (GPS), Section 2.3.1, works and to describe how the ALTA project uses GPS, Section 2.3.2.

2.3.1 How does GPS work?

GPS is a common enough technology that almost everyone knows its basic purpose - to tell you where you are on the Earth. Something that many people don't know about GPS is that it can also give you timing precision on the order of billionths of a second! It needs this sort of timing precision to determine

position accurately.

GPS is composed of a constellation of 24 satellites, 5 ground stations, and millions of GPS receivers. The satellites and ground stations are operated by the United States Department of Defense (DoD), while the receivers are operated by whoever wants to purchase one. The satellites orbit the Earth once every 11 hours 58 minutes at an altitude of 20,200 km (well above the Earth's atmosphere) in a pattern such that there are always at least five satellites visible from every point on Earth. Each satellite has an atomic clock on board so that it can maintain very accurate timing. How do the satellites, ground stations, and receivers work together to tell you your location on the Earth and what time it is?

The basic premise of GPS is triangulation - the same concept as ALTA's arrival angle calculation, just applied a little differently. If you know that the distance from you to one of the GPS satellites was 22,000 km, you would know that your position was somewhere on the surface of the sphere of radius 22,000 km that was centered on the GPS satellite. If you also know that you are 24,000 km away from a different satellite, you would have to be on that sphere too. In order for you to be on the surface of both of these spheres you would need to be somewhere on the circle that defined the intersection of those two spheres. Now, if you know the distance to just one more satellite you would narrow your position down to just two points on that circle. Generally, one of these points lies somewhere on, or near, the Earth's surface and the other lies somewhere very far away from the Earth's surface. Consumer GPS systems assume that you are near the Earth's surface, so you now know your position. This is all based on knowing the distance from you to one of the GPS satellites. How does GPS figure that out?

For now, let's assume that radio signals always travel at $c = 299,792,458 \, \text{m/s}$. Then if you could determine the time it took for a signal to travel from the satellite to your position, you would know the distance between the satellite and your position. To determine the travel time of the radio signal the GPS satellites transmit something called a pseudo-random signal. To explain how this works I'm going to use an analogy from a very good GPS website [54].

Say the satellite and receiver both started singing the "Oh Canada" at exactly the same time. When the receiver gets the satellite's anthem it will be slightly delayed because it had to travel from the satellite to the receiver. The amount of delay will be the travel time from the satellite to the receiver.

In the analogy, "Oh Canada" plays the part of the pseudo-random signal. The signal is called pseudo-random because it is very close to being random, but it is not absolutely random because it is reproduced by both the satellite and the receiver. So, the receiver just figures out how much delay there is between its pseudo-random signal and the satellite's pseudo-random signal, and BINGO you've got the travel time from satellite to receiver. All of this hinges on the fact that the receiver's signal starts at the same time as the satellite's signal.

To ensure that the receiver and satellite are synchronized GPS simply requires one extra satellite. To explain how it works I'm going to use 2 dimensions, instead of 3, to make the explanation easier to convey. If your receiver tells you that you are 5 seconds away from satellite A and 7 seconds away from satellite B, as shown in Figure 2.11, you would think that you were at point **x'**. In the figure the grey lines are your actual distance from the satellite, while the black lines are the distances that your receiver calculates before corrections. But what if your receiver was 1 second fast? That would mean that you are actually only 4 seconds from satellite A and 6 seconds from satellite B, at point **x**. With a third satellite, satellite C, your receiver can figure out how far out of sync it is. If your receiver tells you that you are 9 seconds away from satellite C, that would put you at three places at once: **x'**, **y'**, and **z'** - not a very likely scenario. The grey lines are our actual distances from the satellites, which all join at one point. Since all the satellites are in sync (with their on board atomic clocks), there is only one timing error: your receiver's. That means that there must also be just one timing correction that will make all three circles intersect at one position, point **x**. The receiver calculates this correction and applies it to the measurements, putting you finally where you actually are, at point **x**. In the 2-dimensional case you needed three satellites to get timing and position, so in 3-dimensions you will need four satellites to
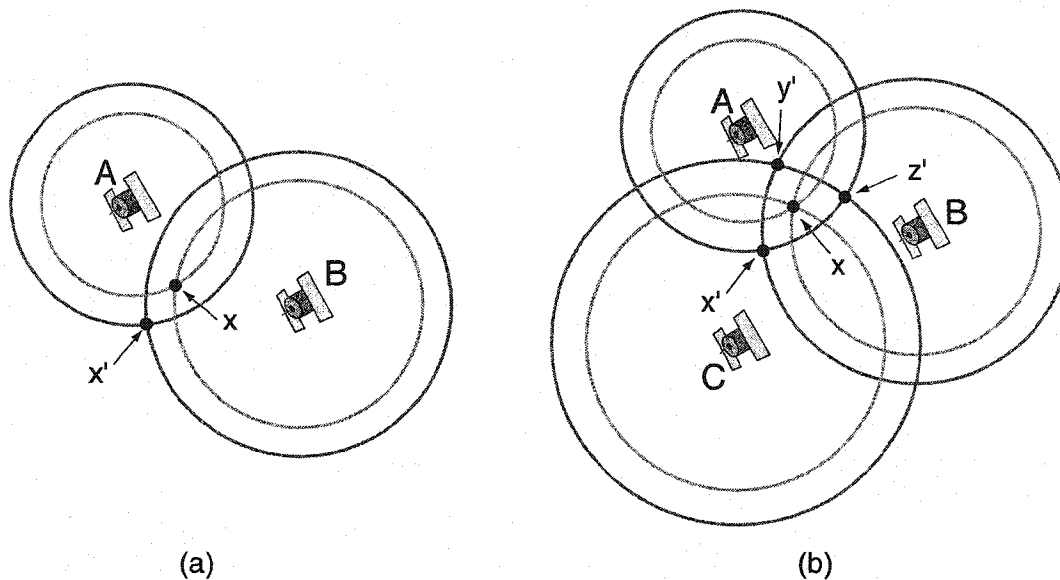
Figure 2.11: Determining location in two dimensions with uncertain timing using (a) two satellites (b) three satellites

do the same thing.

So that's the basics of how GPS works. Unfortunately, we have made some incorrect assumptions that simplify the matter quite considerably. The most obvious assumption being that the signal is not going to travel at c all the way from the satellite to the receiver, it must pass through the atmosphere. This is called propagation uncertainty. The most significant sources of propagation uncertainty are the ionosphere and the troposphere. The ionosphere is a layer of ionized gas 50 km to 500 km above the Earth. The ions alter the path and propagation speed of the electromagnetic signal. The troposphere is where most of our weather comes from, and so the density and moisture content of the air changes significantly with time. Changes in density and moisture content will change the index of refraction of the atmosphere. Both the ionosphere and troposphere are monitored and modeled to calculate these effects and then corrections are made in the signals via communication between the 5 ground stations and the satellites. The accuracy of the modeling is the limiting factor in the corrections.

Another source of error in the signal propagation is multipath error. Multipath error is caused by a GPS signal reflecting off of some structure on the

Earth's surface, like a building or a mountain. This would make the travel time of the signal not equal to the shortest path length from the satellite to the receiver. In the ALTA experiment multipath errors are minimized by installing all of our antennas on the roofs of buildings.

There are many more sources of uncertainty, each varying in magnitude and complexity, some being easier to fix than others. For more information I will refer the curious reader to [54], and an interesting paper explaining the need to account for both special and general relativity in GPS technology [55].

2.3.2 What does ALTA do with GPS?

ALTA uses GPS to determine each site's longitude, latitude, and altitude, and to determine each event's arrival time, or *time tag*. Since the time tag is generated in the electronics crate it will be discussed in Section 2.4. This section contains an outline of what the GPS system needs to send in order for the electronics crate to generate the time tag. Figure 2.12 is a schematic of the GPS system at an ALTA site.
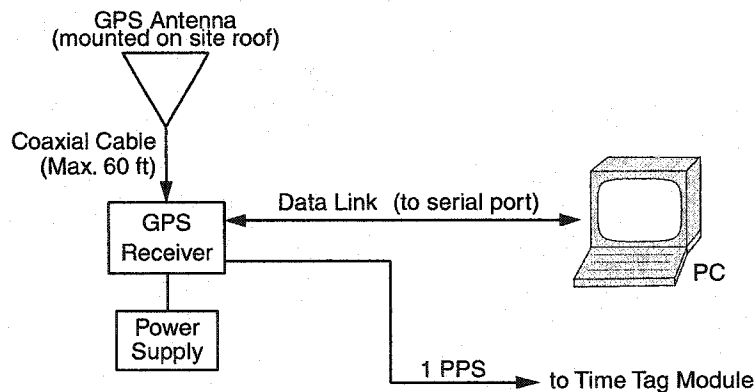
Figure 2.12: Schematic of GPS system at an ALTA site

The antennae are Micropulse (now a division of Andrew Corp.) models 19300 and 2640NW. All of the sites currently in operation have model 19300 antennae, while all new sites will have model 2640NW antennae. The change in antennae model was forced by lack of supply. The receivers are all Motorola UT+ Oncore receivers.

The receiver sends a pulse every second to the time tag module in the

electronics crate. This pulse, called the PPS (pulse per second) pulse, is one of the pieces of information used to time tag an event.

The receiver also communicates with the computer via a bi-directional data link to the serial port. The computer can run one of two programs to communicate with the receiver; the ALTA program, or a program called TAC32 (Totally Accurate Clock, produced by CNS Systems Inc. [56]).

TAC32 is used primarily to initialize the reference location of the antenna. TAC32 is operated in *navigation* mode for an extended period of time (on the order of days) to determine the location of the ALTA site. The TAC32 program is also used to initialize some receiver parameters and to diagnose suspected problems in the GPS system.

After the TAC32 program has been stopped the ALTA program can initialize the receiver to run in *precision timing* mode. In precision timing mode all of the satellites are used to maximize timing accuracy. No satellites are 'wasted' on position measurements, since the position is already known. The ALTA program then reads the date, time, and something called the *sawtooth correction* from the receiver once every second. The sawtooth correction is a timing correction for the PPS pulse. The sawtooth correction ranges from -50 ns to +50 ns since the receiver sends the PPS on the edge of an internal oscillator that is not synchronized with the satellites.

During the summer of 2001 GPS tests were completed to determine the resolution of the GPS timing system. A resolution of 16 ns is achieved when comparing two sites that are observing the same satellites (at least ∼4). This same satellite approximation is valid for sites up to about 2000 km apart. These tests are discussed in detail in [57].

2.4   The Electronics Crate

This section contains a description of the major components and functions of the ALTA electronics crate. The electronics crate contains seven modules, plus high and low voltage power supplies. Each module has a specific function that will be discussed in detail in this chapter. All the modules were designed

and constructed in the physics electronics shop at the U of A. The crate housing is a 6U Eurocrate (6U refers to the height of the crate). Figure 2.13 is a picture of an ALTA electronics crate. Figure 2.14 is a schematic of the crate and its components.
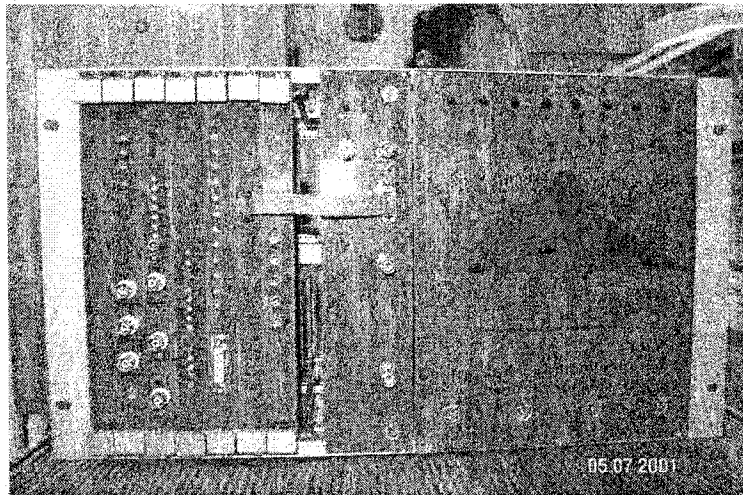
Figure 2.13: Photograph of ALTA electronics crate
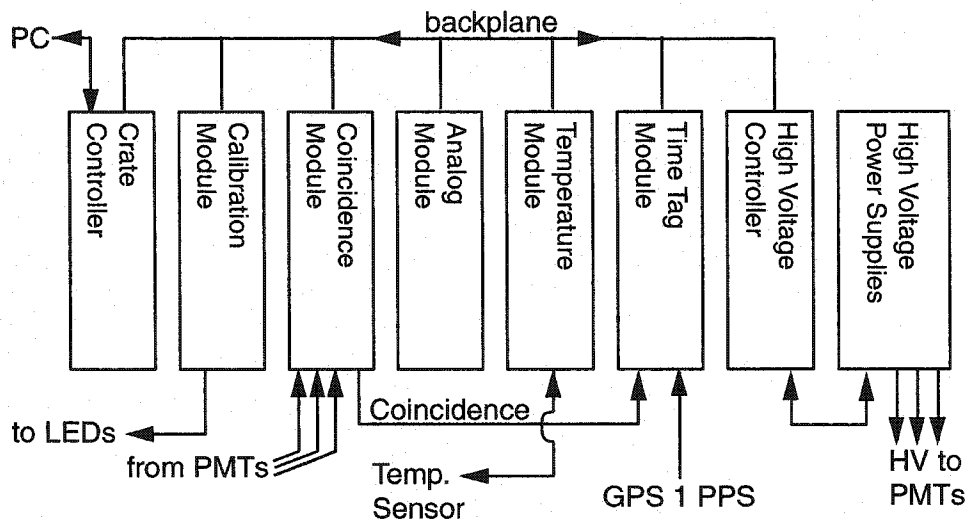
Figure 2.14: Schematic of ALTA electronics crate

The function of each of the modules is outlined in the following sections. The coincidence, analog, and time tag modules are explained first, since they are fundamental to understanding what the electronics crate does.

43

2.4.1 The Coincidence Module

The coincidence module has two functions. First, it determines when all, or a subset of, the three PMTs fire within 120 ns, called the coincidence window. The second part of the coincidence module's job is to determine the time differences between the coincident PMT signals. This is the *local timing*. The coincidence module can run in three different modes:

Singles Mode A signal from any 1 PMT will create an event.

Doubles Mode A signal from any 2 PMTs within the coincidence window is required to create an event.

Triples Mode A signal from all 3 PMTs is required within the coincidence window to create an event.

The output signals from the 3 PMTs are fed directly into the coincidence module. The PMT signals are shown coming into the coincidence module on the left hand side of Figure 2.15. This diagram shows the circuit for only one of the three channels, since the other two circuits are identical.
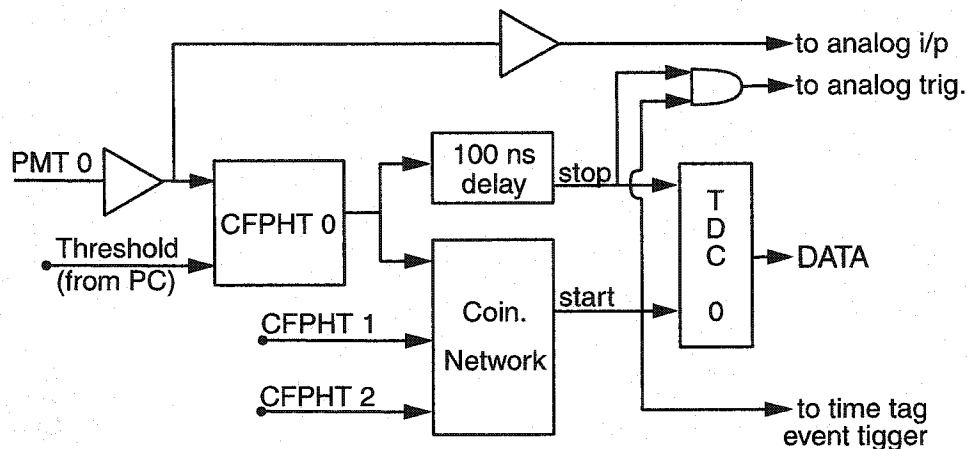
Figure 2.15: Block diagram of coincidence module

The operational amplifiers (large triangular symbols) act as amplifiers to increase the amplitude of signals and as buffers to electronically separate two different sections of circuitry. After passing through the op amp the signal is fanned out to two places. One signal goes directly to the analog module

44

(which will be discussed in Section 2.4.3) and the other goes to the constant fraction pulse height trigger (CFPHT).

The CFPHT is a discriminator which triggers on a constant fraction of the input signal's amplitude [58]. They are commonly used for accurate timing applications. In a CFPHT the input is fanned out to three signals[1]; one signal (call it signal A) is attenuated by the desired fraction of input signal amplitude, the second signal (B) is inverted and slightly delayed, and the third signal (C) is sent to a comparator. Signals A and B are summed and presented to the input of a zero-crossing discriminator. Using a positive CFPHT input signal as an example; as signal A comes into the zero-crossing discriminator the signal goes slightly positive, but when signal B arrives the signal is sent negative and crosses zero with a steep slope. The signal always passes zero at the same fraction of the input signal's amplitude because signal B was attenuated by that fraction. Signal C, which was sent to the comparator, is used to determine if the pulse amplitude was above threshold. The threshold of the CFPHT is defined by the user with the ALTA software. When a pulse above threshold is input to the CFPHT a 120 ns wide pulse is produced by the CFPHT.

The output of the CFPHT is fanned out into two signals. One signal goes to a 100 ns passive delay. The second signal goes to the coincidence network that acts as an AND gate for the three CFPHT output[2]. Coincidences up to 120 ns are passed by the coincidence network, so the coincidence window is said to be 120 ns. The user cannot adjust the width of this coincidence window. The coincidence network produces an output signal when the last CFPHT signal arrives. The output of the coincidence network is another 120 ns pulse.

The output of the coincidence network is fed to the 'start' input of that channel's TDC (Time to Digital Converter)[3]. When the TDC receives the start signal from the coincidence network it begins collecting charge. The TDC stops

---

[1]The details of the CFPHT are not shown in the figure

[2]The coincidence network is the only component shown in Figure 2.15 that is common to all three channels, ie. every other component shown has one for each channel

[3]The TDC is actually 3 TACs (Time to Analog Converters) which are multiplexed to a single 12 bit ADC (Analog to Digital Converter

collecting charge when the delayed CFPHT signal arrives (remember that the output of the CFPHT was fanned out, and one signal went through a 100 ns delay). The TDC then converts the charge into a digital value proportional to the amount of charge.

This means that the count value in the TDC is proportional to 100 ns minus the time difference, $\Delta time$, between the last signal to arrive and the signal of whichever channel the TDC is in;

$$TDC \propto 100\,ns - \Delta time$$

To be sure this is clear I'm going to use an example. Let's say a shower passes through all three detectors, first hitting detector 0, then 20 ns later hits detector 1, then, 60 ns after hitting 0, it hits detector 2. When the last signal arrives (from detector 2) the coincidence network determines that there was a coincidence and sends a start signal to the TDC. TDC channel 0 gets a stop signal 40 ns later $(100 - 60 = 40)$, TDC channel 1 gets a stop signal 80 ns later $(100 - 20 = 80)$, and TDC channel 2 gets a stop signal 100 ns later $(100 - 0 = 100)$. So the last signal to arrive will always register in the TDC bin representing 100 ns. The TDCs in the ALTA coincidence modules have been calibrated so that 1 TDC bin is equivalent to 25 ps.

In the spirit of simplicity I have neglected a signal delay caused by the coincidence network. It actually takes about 8 ns for the network to determine if a coincidence occurred, so the output of the coincidence actually comes about 8 ns after the arrival of the last signal. This means that the delay is effectively only 92 ns, not 100 ns, and so the coincidence window is actually only 92 ns.

2.4.2 The Time Tag Module

The purpose of the time tag module is to determine the arrival time of the shower in GPS time, the *global timing*. As seen on the left side of Figure 2.16 the time tag module requires two inputs, the event trigger from the coincidence module and the GPS 1 pulse per second (PPS).

The time tag module contains a 100 MHz oscillator (MTI-Milliren series

46
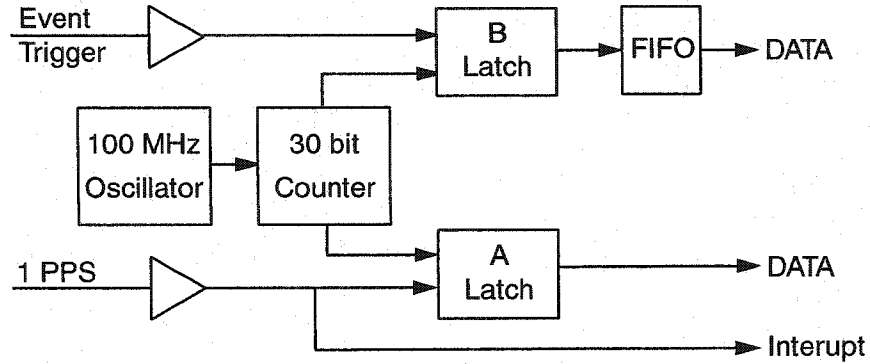
Figure 2.16: Block diagram of ALTA time tag module

OCXO 210) which toggles a 30 bit counter. When a GPS PPS is received it is given an "A latch" value. The A latch value is simply the value of the 30 bit counter at the time the PPS is received. The PPS is also sent to the computer as an interrupt, a message telling the computer to read the data from the crate. Therefore, data from the crate gets read by the computer once every second.

The event trigger goes through a similar process. When the event trigger is received it is given a "B latch" value. The B latch is just the value of the counter when the event trigger was received. Since there can be more than one B latch value in a second the data must be stored temporarily in the module. The data is stored in a FIFO (First In First Out) memory device until the computer receives the interrupt and reads the data. The FIFO can hold 42 events.

By looking at which second an event from the FIFO is read out we can tell the arrival time of the shower accurately to one second. To get more accurate timing we can look at the relative values of the A and B latches. This works because they are both read from the same counter. Since the interrupt is synchronized to the A latch, the data read out every second will be the A latch value for that second and the B latch values for the *previous* second. For example, if the GPS second of an event is 43 the event actually happened some time in the 42nd second (ie. 42.387... seconds).

The equation to determine the time of arrival of an event from the A latch, B latch, GPS time, and sawtooth correction (see Section 2.3.2) is:

$$Event\ Time = GPS\ Second + \frac{(Blatch - Alatch)}{Oscillator\ Frequency} + \frac{Sawtooth\ Correction}{10^9}$$

2.4.3   The Analog Module

The purpose of the analog module is to determine the size of the PMT pulses. It is important to understand that the size of the PMT pulses is proportional to neither the energy of the cosmic ray shower nor the energy of the particle which passed through the scintillation detector. The size of the pulse is proportional to the energy that the incident particle(s) deposited in the detector. This topic is discussed in more detail in Section 3.1.

The heart of the analog module is the integrator / discriminator chip pair, donated by the University of Penn State, designed for Sudbury Neutrino Observatory (SNO). The basic function of the integrator is to take the input PMT pulse from the coincidence module and determine the total charge (the integral) of the pulse or pulses. This is a measure of the size of the pulse. The block diagram for the analog module is shown in Figure 2.17.
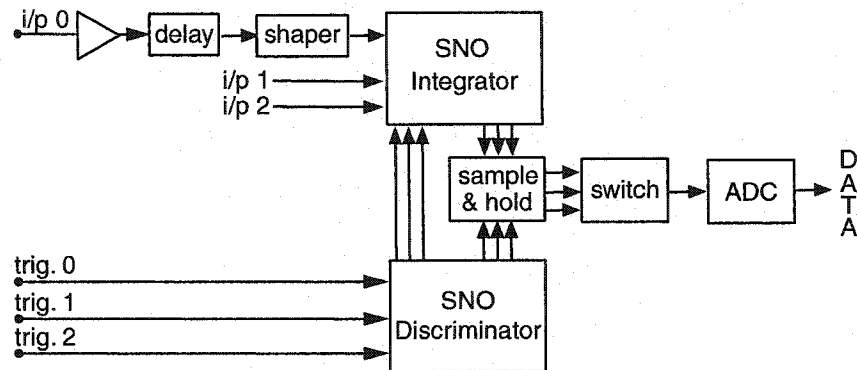
Figure 2.17: Block diagram of ALTA analog module

The 'i/p' (input) and 'trig.' (trigger) inputs on the left side of the figure come from the coincidence module. The i/p pulse is first delayed by 125 ns and then 'shaped' to reduce noise in the signal. The trigger pulse is fed to the input of the SNO discriminator. The SNO discriminator sends a 'start' signal to both the SNO integrator and the sample & hold when it receives a trigger from the coincidence module. The integrator begins building up charge

proportional to the charge of the i/p input when it receives the 'start' from the discriminator. That's why the i/p signal was delayed - the integrator must be told to 'start integrating' before the pulse arrives at its input. The sample & hold reads the output of the integrator for 600 ns after receiving the 'start' from the discriminator. After 600 ns the charge from the sample & hold is sent to a multiplexing switch and then to a single ADC (Analog to Digital Converter)[4]. The ADC value is then given to a FIFO circuit in the FPGA, where it is stored until read out into the data. The ADCs are calibrated so that 1 ADC bin corresponds to about 0.4 pC of charge.

2.4.4 The Calibration Module

The calibration module is primarily used to setup and debug the rest of the electronics. The module also controls the blue[5] LEDs that are mounted in the scintillators. The LEDs are fired once every second as a test to ensure the detectors are operational.

2.4.5 The Temperature Module

The temperature module reads the temperature sensors and programs the temperature controllers in the doghouses. As discussed before, the minimum temperature of the doghouse can be controlled by turning on the heater tape when the temperature is below some arbitrary value. The temperature module also records the temperature inside the electronics crate so that we can determine if problems with electronics are due to overheating.

The temperature sensors used in the doghouses are Dallas Semiconductor DS1621 digital thermometers. The sensors are read out sequentially in sync with the GPS 1 second pulse, so the temperature of each detector is read every 4 seconds.

---

[4]The switch is used so that only one ADC is necessary, not three

[5]Blue was chosen to match spectral sensitivity of PMTs

2.4.6 High Voltage Control Module

The high voltage control module controls the high voltage used by the PMTs. It converts user input at the PC from a digital signal to an analog voltage that controls the power supplies. The module also reads the high voltage and displays the value for the user.

2.4.7 The Crate Controller Module

The crate controller is the communication link between the crate and the PC. The controller communicates with the crate via a 7 slot backplane. The current model of the crate controller uses a 16 bit parallel connection to communicate with the computer. It is likely that the connection will be switched to a USB connection in the future, since this will provide more readily available hardware and accept a higher data rate.

2.5 The Software

This section is a "how-to" guide for the ALTA data acquisition and control software. It is not meant to explain the code used to create the program. The software was written by Bill Burris in Microsoft C# to work in Windows 2000 and XP environments. Figure 2.18 is a screen shot of the main display screen. The important features of the ALTA software are numbered in Figure 2.18. Each feature is explained in the list below.

1. **Event Status**: The event status light will flash green whenever there is a 'good' event, red when there is a 'bad' event, and will stay black when there is no event. A 'good' event is one that has three ADC and three TDC values for each B-Latch. A 'bad' event is one which created a coincidence but somehow has a zero in one or more of the ADC and TDC values.

2. **GPS Date/Time**: This is the GPS date and time. GPS time is Universal Coordinated Time (UTC). UTC is approximately the same as

50
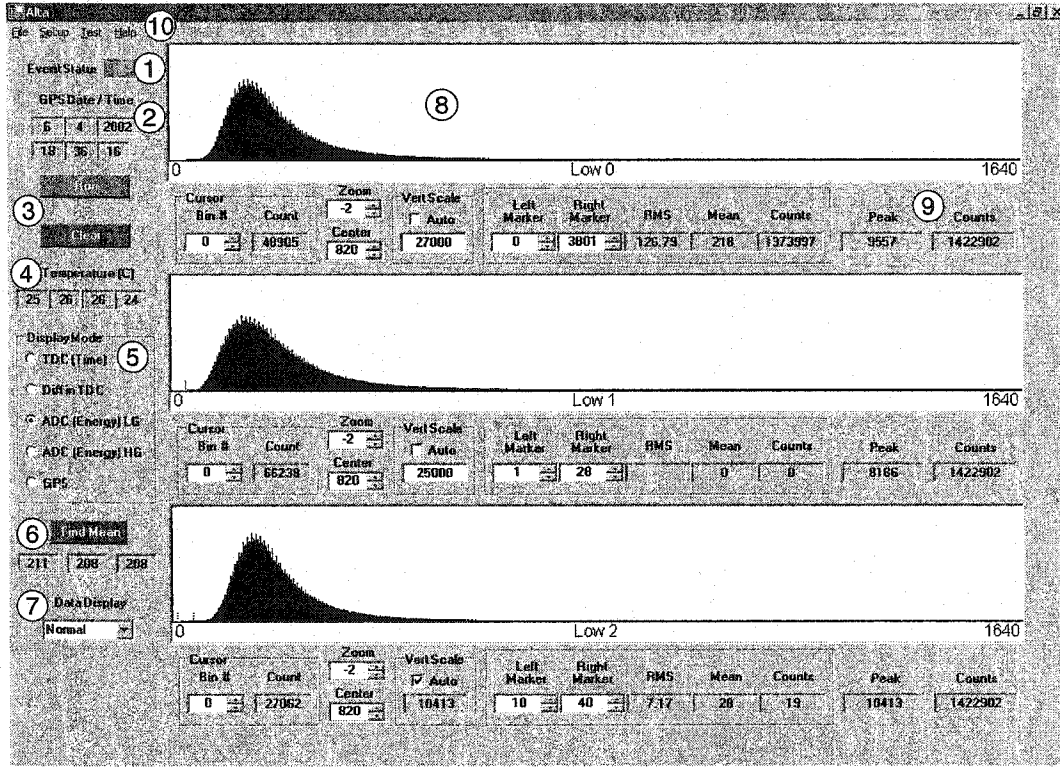
Figure 2.18: ALTA software main display

Greenwich Mean Time. The GPS time will only be updated on the screen when the program is running.

3. **Run/Stop/Clear**: Pressing "Run" will start the program running (ie. collecting data). When you press the "Run" button it will disappear and a "Stop" button will appear. The "Clear" button will clear all of the data from the histograms on the screen. If either the "Clear" or "Stop" buttons are pressed a new data file is written.

4. **Temperature**: This displays the temperature of doghouses 0, 1, 2 and the electronics crate - in that order.

5. **Display Mode**: The "Display Mode" box allows you to choose which data you wish to display on the screen. Each selection is described below.

TDC (Time) The TDC mode displays the value of the Time to Digital Converter for each channel. This gives the relative time of arrival of the three signals in units of TDC bins. To convert to actual time;

51

one bin equals 25 ps, or there are 40 bins per ns. The last signal to arrive is always put in the *last* bin, roughly bin number 3750, and the previous signals are put in corresponding lower bins.

Diff in TDC This mode displays the time differences between the three channels in units of TDC bins. The three histograms are for the three possible combinations of time difference: last-first, middle-first, last-middle.

ADC (Energy) LG This mode displays the value of the Low Gain ADC for each of the three channels, so the horizontal axis is energy in units of ADC bin. The energy here is the energy that was deposited in the detector, not the energy of the incident particle or the energy of the shower. The conversion of this histogram to actual units of energy depends on the gain of the PMT in that channel, so it differs for every site.

ADC (Energy) HG We no longer have a High Gain ADC, so it will be taken out of the software when the next version is released.

GPS This mode gives information about the performance of the GPS system. The three histograms are: A latch value, A latch value with sawtooth correction, A latch minus B latch value.

6. **Find Mean**: Pressing the "Find Mean" button will make the program calculate the mean value of whichever histograms are currently displayed.

7. **Data Display**: In the "Data Display" pull down you have a choice of "Normal" or "Filtered". "Normal" will display all "good" and "bad" events, while "Filtered" will only display "good" events.

8. **The Histograms**: There are three histograms, one for each detector 0, 1, and 2, in order from top to bottom of the display. The horizontal axis is defined by your choice of "Display Mode", and the vertical axis is always the number of counts in the specified bin.

9. **View Control**: Under each histogram is a bar that allows you to control

the view of the histogram and investigate statistics of different parts of the histogram.

Cursor The "Cursor" box allows you to place a cursor in any bin and reads the number of counts in that bin.

Zoom The "Zoom" button allows you to select the horizontal zoom of the histogram. When changing the zoom the histogram will automatically center on the peak value of the histogram.

Center This allows you to manually chose the position of the center of the histogram, in other words, it scrolls you across the histogram.

Vert Scale This sets the vertical scale. When the "Auto" selection is checked, the histogram will scale to the same size as the peak value in the histogram. To manually select the scale just type in the number of counts you would like to correspond the top of the histogram box.

Statistics Box The next box can be used to help the user determine statistics about the histogram. The "Left Marker" and "Right Marker" tabs allow you to specify which part of the histogram you would like statistics in. The following three boxes are the statistics for the bins between the markers. "RMS" gives the root mean squared deviation (or standard deviation) of the bins, i, between the cursors:

$$RMS = \sqrt{\frac{\sum_i (n_i x_i^2) - \frac{1}{N}(\sum_i n_i x_i)^2}{N}}$$

where n is the mean value of the bin (equal to the bin number for all of the ALTA histograms), x is the number of counts in the bin, and N is the total number of counts between the cursors. The "Mean" gives the mean value between the cursors, and "Counts" gives the total number of counts between the cursors.

Peak This box displays the number of counts in the bin with the largest number of counts (the peak).

Counts This box gives the total number of counts in the histogram.

10. **Menu Bar**: The menu bar in the ALTA software currently has four menus; "File", "Setup", "Test", and "Help". The "File" menu contains the commands "open", "save", "clear", and "exit". The "open" command allows you to open a previous .alta file, the "save" command allows you to save the histogram data as a text file, the "clear" command operates the the same as the "Clear" button, and the "exit" command closes the ALTA program. The "Test" is used for the remote interface application, and the "Help" menu currently contains nothing. The "Setup" menu contains several commands that allow the user to change things like the voltage of the PMTs, the threshold of the CFPHTs, and the coincidence mode. I will discuss each of these options individually below.

The "Setup" menu contains 8 options, divided into two groups. The first group contains the options "FPGA", "Initialize Hardware", and "Restore Settings Files". The "FPGA" command brings up a pop-up window (not shown) that allows you to load the control programs into the FPGAs (Field Programmable Gate Arrays) in the crate. You can do them all at once or select them individually. The FPGAs must be loaded every time the power to the crate is turned on. The FPGAs are like the brains of each module, but they have a volatile memory so they don't 'remember' anything after being powered off. The "Initialize Hardware" command puts the hardware (PMT voltage, coincidence mode, etc.) back to the last values set. The "Restore Settings File" replaces the settings files with ones in the C:/alta/settings directory. This can be done locally or remotely.

The second group of options contains; "Coincidence", "High Voltage", "Temperature", "Analog", and "Calibration". These are the options that will be most often used when modifying the ALTA system, and are discussed in the Figures below.
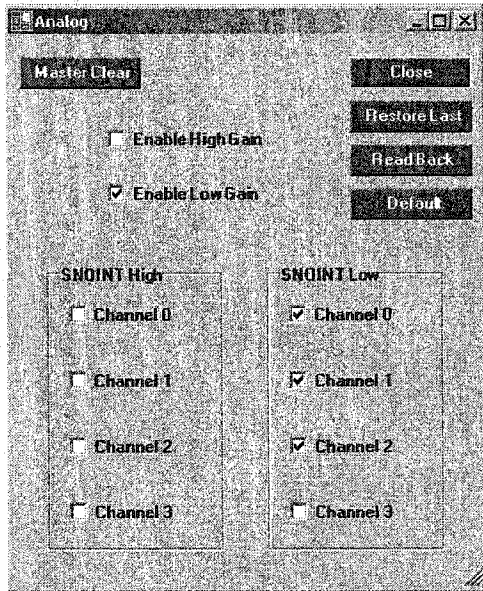
The analog pop-up allows you to chose which channels of the analog module that you would like to enable. Normal operating mode is in Low Gain enabled with channels 0, 1, and 2 checked. Since the High Gain channel has been permenently disabled the "Enable High Gain" check box does nothing. This will be taken out in the next version of the software. The check boxes for Channel 3 do nothing.
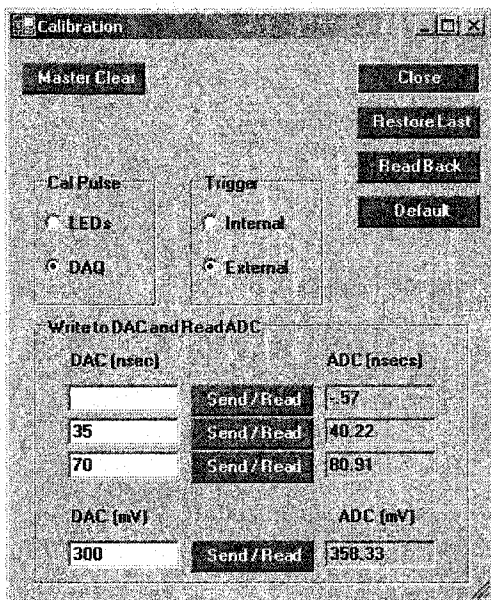
The calibration pop-up is used for debugging the system. It will not be used in regular operation very often. There have been some changes to the hardware that will change the options available in this window when the next version of the software is complete.
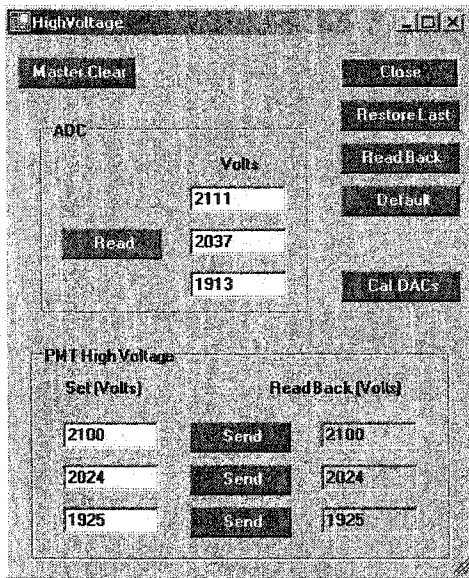
The High Voltage pop-up allows you to change the high voltage of the PMTs. In the "PMT High Voltage" box, typing the desired voltage (in Volts) into the "Set" text boxes and pressing "Send" will set the voltage of the PMT. The text boxes are ordered detector 0, 1, 2, from top to bottom. The "Read Back" boxes display what value was sent to the power supplies. Pressing "Read" in the "ADC" box will read the voltage from the PMTs. The "Cal DACs" button allows you to calibrate the digital to analog converters which control the voltage on the PMT.
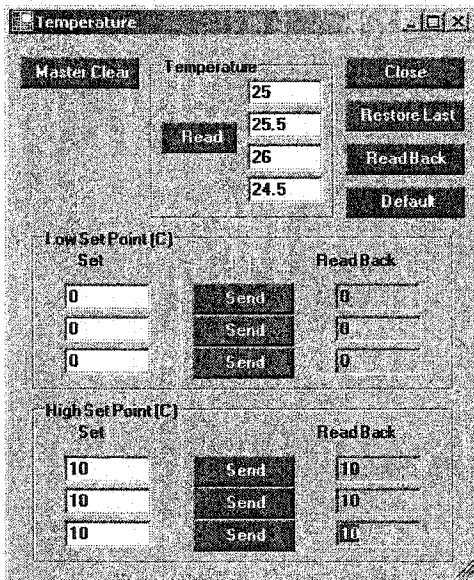
The Temperature pop-up allows you to control the high and low limits of when the heat tape is turned on and off. It also allows you to manually read the temperatures. In the "Temperature" box the temperatures of detector 0, 1, 2, and the crate are listed from top to bottom, respectively. In the "Low Set Point" box you can input the value that you would like the heat tape to turn on in the "Set" box. Pressing "Send" will apply the change. The "High Set Point" box works the same way, except that it is the temperature at which the heat tape will turn off.

Chapter 3

System Calibrations and Uncertainties

This chapter is devoted to explaining the calibration procedures for the system and detailing the uncertainties in the data and quantities derived from the data. The data includes the ADC data (energy), the TDC data (local timing), and the GPS data (global timing). Quantities derived from the data include arrival angle and a lower limit on the energy of the primary particle.

3.1   Deposited Energy

'Deposited energy' is the amount of energy lost (deposited) by the secondaries of a cosmic ray shower as they pass through the scintillators. The energy lost by the secondary particle is proportional to the amount of light created in the scintillator (typically, plastic scintillators emit 1 photon per 100 eV deposited [59]). The amount of light produced is proportional to the size of the PMT pulse. The ADC value of an event is proportional to the size of the PMT pulse, so the ADC value is proportional to the amount of energy lost by the secondary particles as they pass through the scintillator.

This information is useful if the particles passing through the scintillator are minimum ionizing particles (MIPs). A MIP is a heavy (compared to an electron), singly charged subatomic particle with an energy $\gtrsim$ 1000 MeV for protons and $\gtrsim$ 100 MeV for muons. Other heavy subatomic particles have minimum ionization thresholds in the same order of magnitude as protons and

muons. The important thing about MIPs is that they lose about the same amount of energy per amount of material that they pass through ($\frac{dE}{dx}$). For MIPs $\frac{dE}{dx} \approx 2$ MeV/(g/cm^2) (the unit g/cm^2 is a measure of the amount of material a particle passes through, derived from density × length). So, for example, a MIP passing through 1 cm of material with a density of 1 g/cm^3 would lose about 2 MeV. It is important to note that the amount of energy lost is not dependent on the energy of the MIP.

Considering the ALTA detectors, if only one particle passes through the energy deposited will depend on the path length of the particle in the detector. This means that particles that arrive vertically will deposit the least energy. Since a majority of cosmic ray showers detected are roughly vertical, the majority of events will have pulses which correspond to the energy deposited by a MIP traveling through the vertical thickness of the detectors. The detectors (except for the U of A detectors) are 1 cm thick and have a density of approximately 1 g/cm^3, so most events will deposit 2 MeV in the detector, producing $\sim 20,000$ photons[1]. A typical MIP peak in an ADC histogram is shown in Figure 3.1, along with the ADC pedestal, which is discussed below. The horizontal axis of this histogram is the ADC value of the channel, which is of course proportional to the energy deposited in the detector.
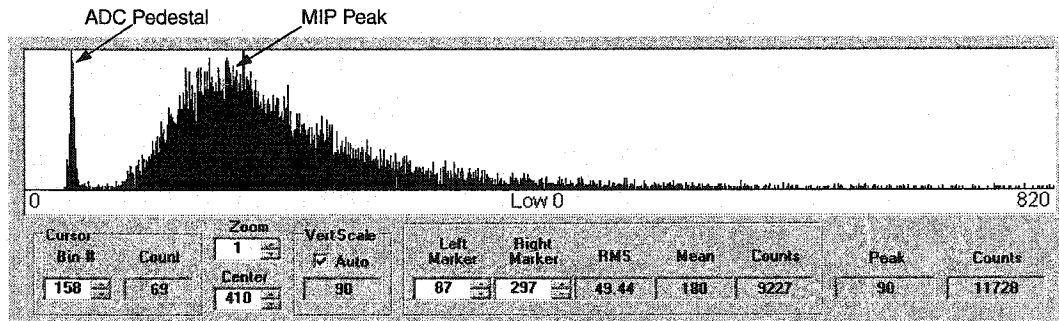
Figure 3.1: A typical MIP peak and ADC pedestal.

To determine the amount of energy deposited at any point other than the MIP peak, the ADC value corresponding to zero energy deposited must be known. Then, a linear correlation between energy loss and ADC value can

---

[1] While 20,000 photons are produced, only about 25 photons are actually converted to photo-electrons at the PMT face.

be derived. This is called *energy loss calibration*. To determine the ADC value that corresponds to zero energy (called the ADC *pedestal*) we simply run the analog module with no input in one of the channels. The detectors are run in normal operating mode (triple coincidence) to get a MIP peak. Figure 3.1 shows an ADC pedestal along with the corresponding MIP peak for that channel. A user would not see the ADC pedestal in normal operation since it is cut out by the triple coincidence requirement. To get the MIP peak and ADC pedestal on the same histogram the detectors were run in normal operating mode and then the input for channel 0 (the channel displayed in the histogram) was disconnected and the input was disabled in the 'Coincidence' pop-up window.

The largest adjustable factor in the energy loss calibration is the PMT voltage. Changing the voltage changes the gain (number of electrons produced at the anode per incident photon) of the PMT. Changing the gain changes the proportionality constant between light produced in the scintillator and size of PMT pulse, which therefore changes the proportionality between energy loss and ADC value. All PMTs have slightly different gains, even if they are the same model from the same manufacturer. So, the gain of the PMT is a very important part of the energy loss calibration.

When setting the gain of the PMT you want to be sure to set it so that you can see as much of your energy loss spectrum as possible. If your gain is too low then events will fall into the pedestal, and if your gain is too high events will overflow the ADC. The gain of the ALTA PMTs is set to the voltage that places the MIP peak at 100 ADC counts above the pedestal. Since each channel has a different pedestal, each MIP peak should have a different value. However, the linear relationship between energy and ADC count should be the same with the exception of an additive constant (equal to the difference in the ADC pedestals).

As you can see in Figure 3.1 the MIP peak is very broad. This makes the position of the MIP peak the major source of uncertainty in the energy/ADC linearization. Typical pedestals and MIP peaks are around 30 and 130 ADC

counts, respectively, so a typical energy loss calibration equation would be

$$[Energy\ Loss\ (in\ MeV)] = 0.02[(ADC\ Value)] - 0.6 \qquad (3.1)$$

A conservative estimate of the uncertainty in the MIP peak determination would be about 30 ADC counts, the uncertainty in determining the ADC pedestal is then negligible. A 30 count uncertainty in the MIP peak would result in a 30% uncertainty in the slope of the energy loss calibration.

But what does all this tell us about the density of particles in the shower front? After all, that is why the energy loss calibration is being done. A very rough approximation of the number of particles can be easily attained by simply dividing the energy calculated from Equation 3.1 by 2 MeV. This approximation is very rough for several reasons. Firstly, the ADC distribution is very wide. This is due to the statistical fluctuations in the number of photo-electrons created in the PMT. Secondly, the ADC distribution is also asymmetrical. The asymmetry is due to secondaries arriving at non-vertical angles - therefore having a path length longer than 1 cm in the detector. Figure 3.2 shows the results of a CORSIKA [60] (see Section 3.2 for a brief description of CORSIKA) study of the incident angles of secondary particles as they hit the detector level; using vertical, 10^{14} eV, proton primaries.

The figure shows that the incident angle of most of the secondaries is confined to a roughly 10° of the shower axis. If primaries with zenith angles up to 30deg are considered, then the path length of the secondaries will be up to 1.3 times as long. This would produce a tail on the high energy side of the ADC distribution, making an asymmetry on the order of 1.3 × MIP peak in the high energy direction. This asymmetry can be seen in Figure 3.1.

So, there's a calibration equation that is uncertain to about 30%, an ADC distribution whose width is larger than the average energy deposited by one particle, and an asymmetry in the ADC distribution on the order of 30%. All these uncertainties combined make the calculation of the number of particles passing through the detector a very rough approximation. What the ADC information *will* tell us is the order of magnitude of the density of particles passing through the detector. An energy loss near 2 MeV means that roughly
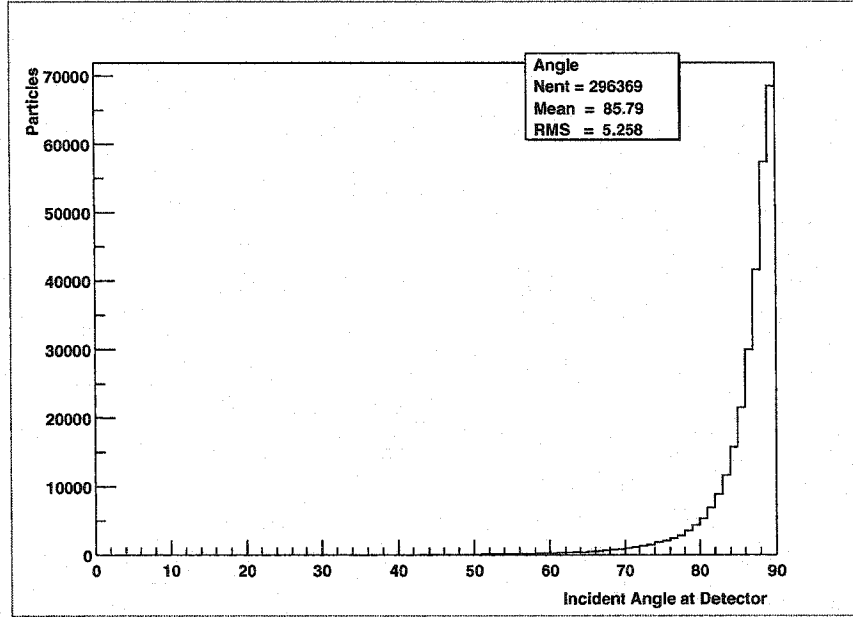
Figure 3.2: Angle of arrival of secondary particles from 100 vertical showers

one particle passed through, while an energy loss of roughly 20 MeV means that roughly 10 particles passed through the detector. It is also important to look at the energy of each channel in an event. If a large shower hit the site, then a large energy loss would be expected in every channel. If a small shower hit the detector and, for example, one particle happened to stop in one of the detectors ($\frac{dE}{dx}$ is very high when particles stop in a detector), then that would create a large energy loss in one channel with small energy loss in the others.

3.2 Primary Energy

The primary energy calibration is the process of determining the energy of the primary cosmic ray by sampling the density distribution of the secondary particles. To figure out the density of particles that would hit the ALTA detectors for different shower energies we have used the Monte Carlo air shower simulation program CORSIKA [60] (version 6.016 using the QGSJET hadronic interaction model). The goal of this simulation is to determine the minimum energy shower that our sites can reasonably detect.

The simulation consisted of 10 runs of 100 showers each. The showers had proton primaries with energies ranging from 1×10^{14} eV to 1×10^{15} eV in

61

10^{14} eV increments. The showers were all dropped vertically directly above the detector. The showers were sampled at 700 m above sea level, the altitude of Edmonton. The first interaction altitude of each shower was determined by CORSIKA.

CORSIKA gives the user the ability to set the kinetic energy cuts for hadrons, muons, electrons, and photons. As discussed in the previous section our secondary energy loss distribution is well defined by a MIP peak near the low end of the spectrum with a long tail following at the high end. I've defined the energy cuts for the CORSIKA simulations to be the MIP energy (2 MeV) of the corresponding particle. For protons MIP energy is greater than 1000 MeV, and for muons MIP energy is greater than 100 MeV [61], so the energy cuts used for hadrons and muons were set at 1000 and 100 MeV, respectively.

The energy cut for electrons and photons is slightly more complicated than for hadrons and muons. To determine the energy cut for electrons I assumed that the electrons were highly relativistic. Low energy electrons incident on the scintillator can deposit 2 MeV, or more, in the detector since the $\frac{dE}{dx}$ for collision loss increases at low energy, but they are not likely to be part of the shower front in a cosmic ray air shower. So, on the assumption that we only want to see the shower front, I can use the exponential radiation loss relationship:

$$E = E_0 e^{-x/x_0}$$

where E is the energy of the electron after passing through x thickness of material of radiation length x_0, and E_0 was the initial energy of the electron. Using the above formula, for an electron to deposit 2 MeV into 1 g/cm^2 of scintillator ($x_0 = 43 g/cm^2$) it would need an initial energy of approximately 90 MeV. Since the electron must also pass through the roof of the doghouse, I rounded the energy cut for electrons up to 100 MeV.

The probability of a high energy photon to be detected in the scintillator is negligibly small. But there is a non-negligible probability for a photon to pair produce in the roof of the doghouse, creating a detectable electron signal. The photon must create an electron pair with at least 100 MeV for the electrons to

leave a MIP signal, so the photon must have at least 100 MeV. On the order of 5% of 100 MeV photons will pair produce in the $\sim$3 g/cm^2 of the doghouse roof. This is assuming the mean free path of 100 MeV photons is 60 g/cm^2 [59] (Z$\simeq$6) in the doghouse roof. With an energy cut of 100 MeV on photons roughly half the particles reaching the detector altitude are photons. Since the detected photons would only make up on the order of 2.5% of detectable particles, all photons are being considered undetectable.

Since the threshold for firing an individual detector is a single MIP, a shower with a density of 1 particle per detector area at 4.5 m from the shower core should reasonably be detected. Since the detector area is 0.36 m^2, the density to get 1 particle per detector area is 2.8 particles per m^2. Figure 3.3 shows the distance from the shower core that the density drops to 2.8 particles per m^2. Using the quadratic fit to the points the energy at which there is a
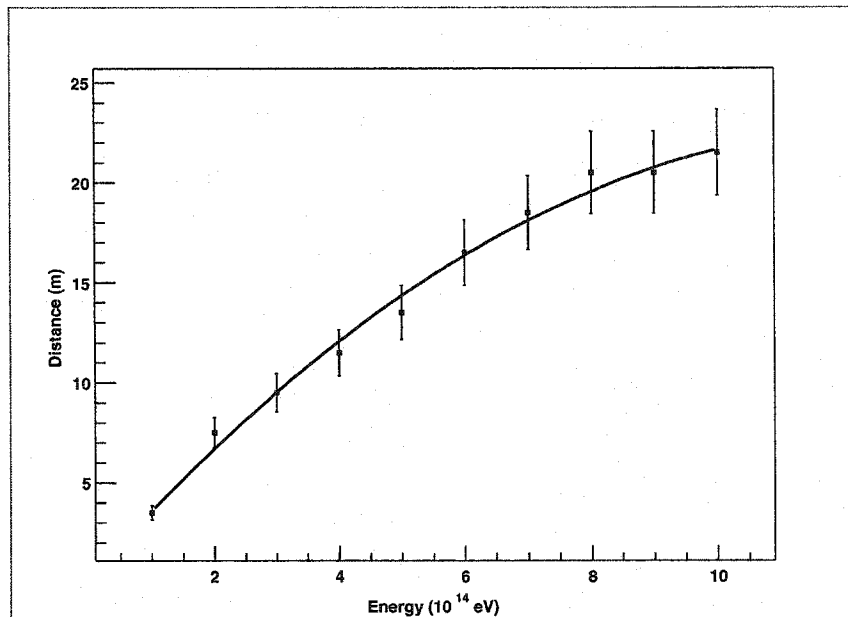
Figure 3.3: Distance from shower core that density reaches 2.8 particles per m^2 as a function of shower energy. The curve represents a fit to a quadratic.

density of 2.8 particles per m^2 at 4.5 m from the shower core is 1.3×10^{14} eV. Therefore, the lower limit on the primary energy for a shower detected by an ALTA site is approximately 1×10^{14} eV.

3.3 Global Timing

Global timing is the arrival times of air showers in Universal Coordinated Time. When determining the resolution of the global timing in the ALTA experiment, it is important to note that the absolute time of the event does not need to be known with much precision. Since the primary goal of the global timing is to compare the arrival times of events at two different sites, it is the relative time of two events that must be known to high precision. This, in combination with the fact that GPS satellites orbit more than 20,000 km above the Earth's surface, works to our advantage. Any two points on the Earth within about a thousand kilometers of each other will always be able to see roughly 5 GPS satellites in common. Therefore almost all of the GPS timing errors that are a result of satellite timing, and some from propagation errors, are canceled out when relative timing is considered.

Testing the relative timing of the ALTA GPS systems was done by comparing the PPS (pulse per second) times of two isolated ALTA systems. Details of the testing procedures and analysis of those results is given in [57]. The testing concluded that there was a 16 ns resolution in the relative timing of the ALTA global timing system.

3.4 Local Timing

Understanding the uncertainties in the local timing is very important since the local timing is used to determine the shower's arrival angle. The following subsections outline the studies that have been completed on the prominent sources of uncertainty in local timing. These studies are preliminary studies which will be followed by more extensive measurements and simulations. The measurements will be completed by superimposing one ALTA site onto another ALTA site. The two sites will be completely independent. Within the statistical fluctuations of the shower front, both sites will observe the same showers. The difference between the arrival angles calculated by the two sites will give a measure of the uncertainty in arrival angle. More extensive simula-

tions will be completed by combining the GEANT detector simulation package
[62] with CORSIKA.

Shower Dimensions

Air showers are not perfectly planar. They have some width. The ALTA
system can not directly measure the dimensions of the shower, so we must rely
on Monte Carlo simulations to give us an understanding of this uncertainty
in our local timing due to the thickness of the shower. Another CORSIKA
simulation was executed, this time with 100 proton showers of fixed energy
(1.3×10^{14} eV) and fixed first interaction height (22.6 km). The first interaction
height was chosen to be 22.6 km because that was the average height of the
1×10^{14} eV showers dropped in the primary energy simulation. Figure 3.4
shows the time distribution of particles arriving at the 700 m detector altitude
between 4 m and 5 m of the shower core[2]. Since the distribution is clearly not
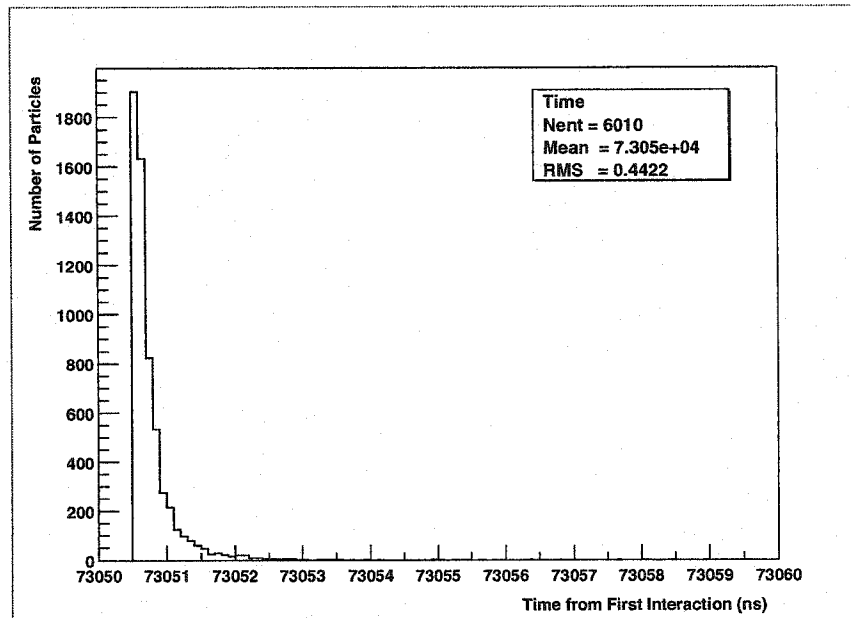
Figure 3.4: Time distribution of particles arriving at 700 m detector altitude
within annulus of 4 m and 5 m from shower core.

a Gaussian distribution, the uncertainty must be estimated on less rigorous

---

[2]The annulus between 4 m and 5 m was chosen because the detectors are all contained
within that annulus if the shower is incident on the center of the detector.

grounds. Since a majority of the particles come within 1 ns, δt_{shower} can be conservatively estimated to be 1 ns.

Scintillator Area

When a particle hits a scintillator there is no way of knowing where it hit on the detector. A particle that hits close to the PMT would show an earlier signal than a particle that hit far from the PMT. This uncertainty due the size of the detector can be determined by setting up a simple test using a small coincidence detector. Figure 3.5 shows the basic setup of the test.
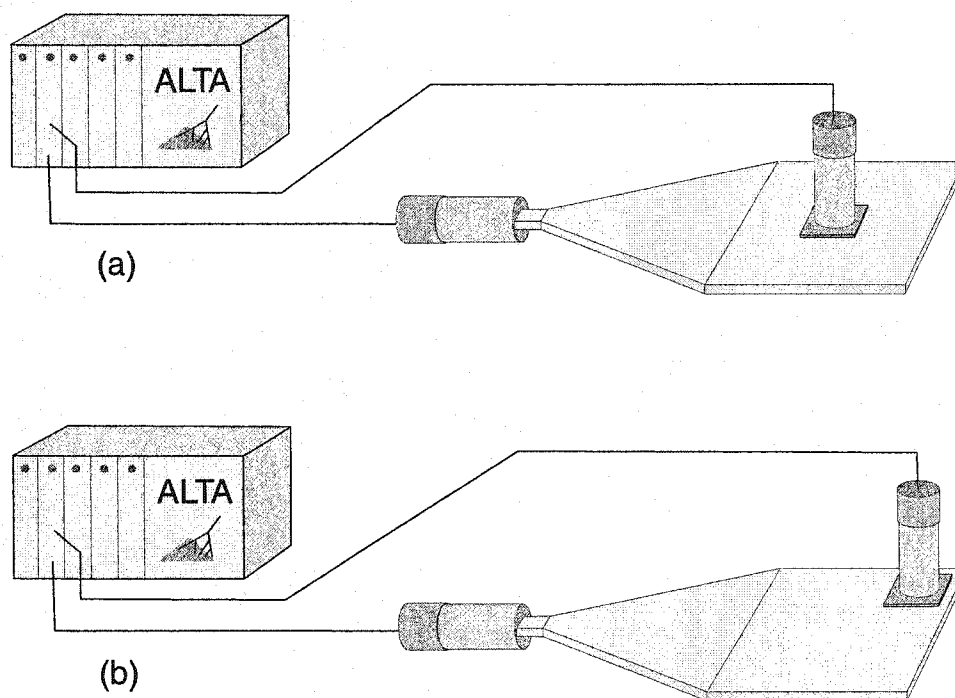
Figure 3.5: Detector Size Test (a) test detector at center (b) test detector at corner

First the test detector is placed at the center of the ALTA detector, and events are collected in double coincidence mode. Then the test detector is placed at the corner of the ALTA detector, and events are again collected in double coincidence. The signal cable of the test detector is slightly longer than the signal cable of the ALTA detector to ensure the test signal always arrives last. Figure 3.6 shows the plots of the arrival times of the ALTA detector signals, in units of TDC counts. The difference between the mean of these

two plots is equal to the uncertainty in our local timing due to the size of the detector.
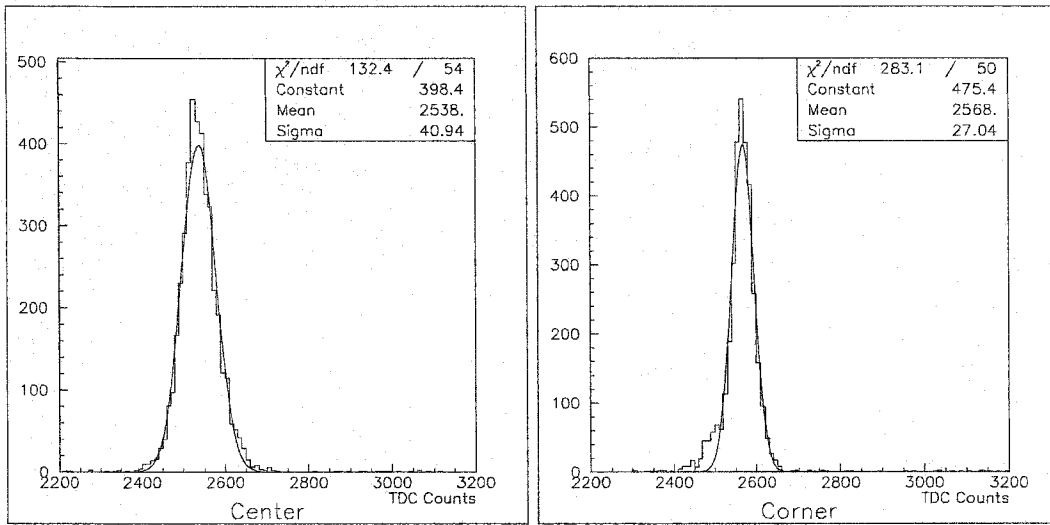
Figure 3.6: Detector size test results

The difference in the mean value of the two plots is 30 TDC counts. 30 TDC counts is equivalent to 0.75 ns, since there are 40 TDC counts per nanosecond. Therefore, the timing uncertainty due to the size of the ALTA detectors is $\delta t_{area} = 0.8$ ns.

You might have noticed a slight difference in the width of the two peaks, the "Center" plot having a sigma of 41, and the "Corner" plot having a sigma of 27. I believe that this is caused by the difference in signal shape that would result from the difference in the test detector's location. With the test detector at the center of the ALTA detector the light emitted has many different paths to travel to the PMT, while with the test detector in the corner of the ALTA detector there are fewer paths for the light to travel in the scintillator. Fewer paths to travel would mean a sharper signal with a faster rise time which would result in more precise timing, as indicated by the smaller sigma in the "Corner" plot.

Signal Delay

A signal delay is the delay that cables and PMT's put into the signal. The PMT's delay is dependent on its HV, threshold, and orientation in external

magnetic fields. Cable delay is dependent on the cable's length, type, and condition. For local timing it is not important to know the actual delay in a channel, it is only important to know the relative difference in delay between channels.

To determine the relative signal delay a calibration procedure was constructed. The calibration measures each detector's timing relative to a small ($\simeq 0.06$ m^2) reference detector. The reference detector is a piece of the scintillator donated by OPAL with an OPAL PMT coupled via optical fibers. The reference detector has a 15 m signal cable and 15 m HV cable that are used in every calibration so that the delay of the reference system did not need to be calculated.

Since this calibration needs to be done on site we needed to know how sensitive the reference detector was to changes in voltage and changes in orientation of the Earth's magnetic field. Figures 3.7 and 3.8 show the results of these two tests. Since we can keep the voltage of the reference detector con-
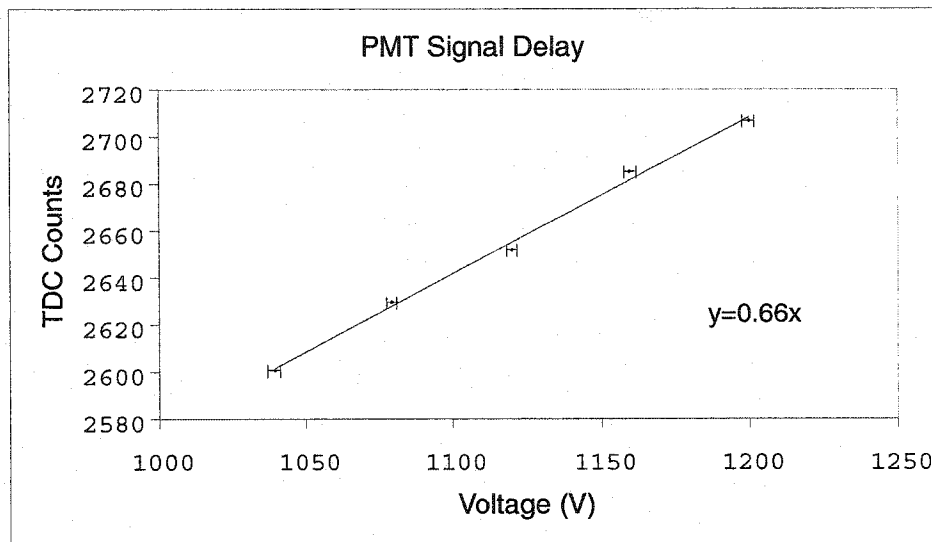
Figure 3.7: A plot showing the dependence of voltage on the timing of the reference detector at 30 mV threshold. The linear fit has a slope of 0.66 TDC counts per Volt.

stant within $\sim$1 volt Figure 3.7 shows that the timing of the reference detector due to voltage fluctuations will be constant to within 1 TDC count (25 ps). This uncertainty is small enough to be ignored.
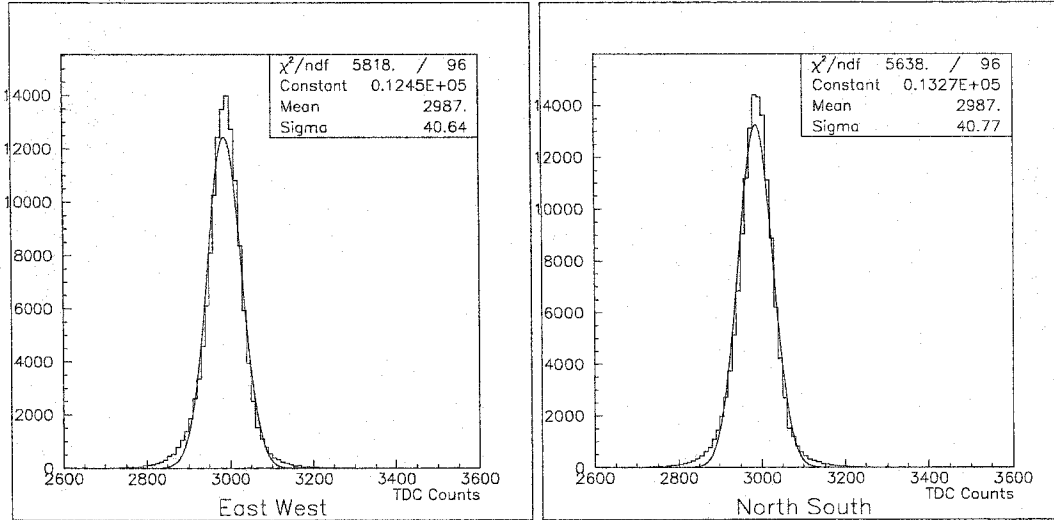
Figure 3.8: Histograms comparing the timing of the reference detector as it is oriented north-south and east-west.

Figure 3.8 shows no dependence of timing on the orientation of the PMT in the Earth's magnetic field. This is likely due to the magnetic shielding placed around the PMTs.

The calibration then proceeded by placing the reference detector on a scintillator and connecting the HV and signal cables to another detector at the site via the 15 m reference cables. The system was then set to count double coincidences between the reference detector and the one being tested. TDC data was collected for $\sim$10,000 cosmic ray counts. The difference between the TDC peaks in the two channels is equal to the difference between the signal delays of the reference and tested detectors. Figure 3.9 shows a typical result of the difference in TDC counts between the reference and a test detector.

The difference between the mean of each of the three test detector's histograms is equal to the relative time difference between the signal delay of each channel. These time differences will be accounted for when determining the local timing. Table 3.1 shows that the typical result of the signal delay test is a correction $\sim$ 1 to 3 ns (40 to 120 TDC bins) to the local timing.

The uncertainty in the signal delay correction comes primarily from the width of the Gaussian in Figure 3.9. The results in Table 3.1 come from the difference of two such Gaussian, so the uncertainty of the result is the quadratic
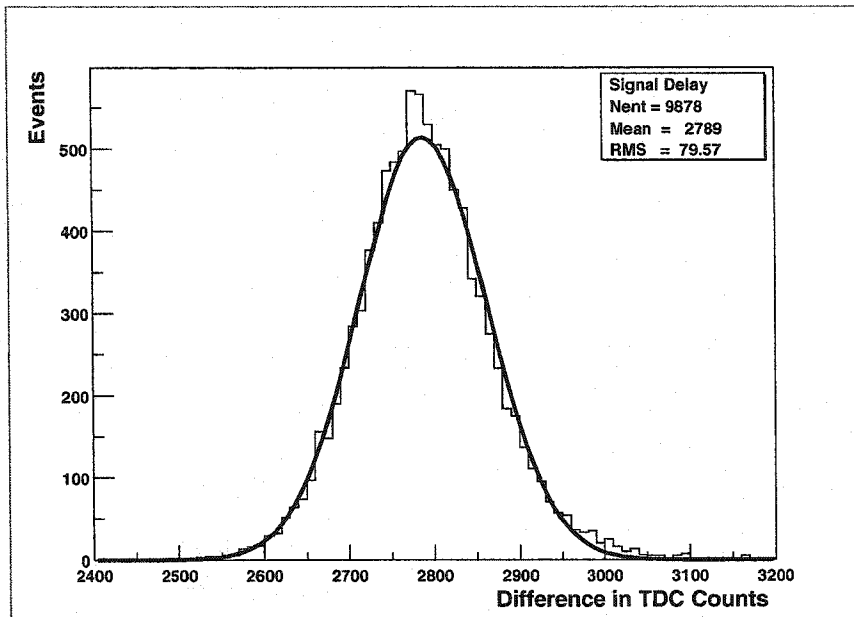
Figure 3.9: Typical TDC difference between reference and test detector in signal delay test

Channels	Result (TDC bins)
TDC(2)-TDC(1)	43
TDC(2)-TDC(0)	-82
TDC(1)-TDC(0)	-113

Table 3.1: Result of signal delay test at MacDonald site

sum of the RMSs. This gives an uncertainty in the signal delay correction, $\delta t_{signal} = 2.5$ ns.

TDC Calibration

To calibrate the TDCs a signal from a pulse generator is fanned into three signals and one or two of the three are delayed by known lengths of time. The scale of the TDC is adjusted so that a signal delayed by 80 ns will produce a TDC value of 3750 while the undelayed signal will produce a TDC value of 550. This means that there are 3200 TDC bins in 80 ns, so there are 40 bins per nanosecond or 25 picoseconds per bin. The TDC is very linear in this 80 ns region. It is not necessary to guarantee linearity past 80 ns since detectors would need to be spaced nearly 30 m apart for a valid shower to

register 80 ns.

The uncertainty in this calibration is dominated by the width of the peaks at bins 550 and 3750. Figure 3.10 shows a typical histogram of the TDC calibration process. The ALTA program is in "TDC Difference" mode, so the display shows the difference between the TDC values. The coincidence module is being pulsed with signals that were fanned out from a signal generator with one signal going through an 80 ns passive delay before reaching the coincidence module. The RMS value of the peak (a typical result for the calibration procedure) is 1.35, as seen in Figure 3.10. This shows that the uncertainty of the calibration is on the order of 1.5 TDC bins, or 40 ps, negligible when compared to the other local timing uncertainties.
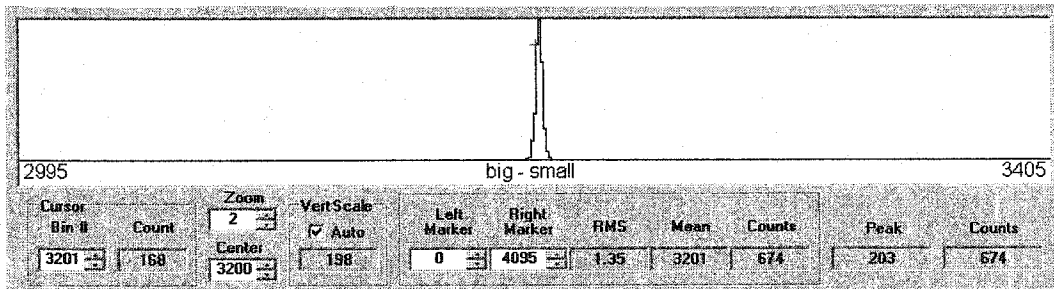
Figure 3.10: A typical display of a TDC calibration

Sum of Local Timing Uncertainties

When all of the local timing uncertainties are added in quadrature;

$$\delta t_{local} = \sqrt{\delta t_{shower}^2 + \delta t_{area}^2 + \delta t_{signal}^2} \tag{3.2}$$

$$= \sqrt{1^2 + 0.8^2 + 2.5^2} \tag{3.3}$$

$$= \pm 3 \; ns \tag{3.4}$$

Therefore the total local timing uncertainty is 3 ns. Since all of these uncertainties are independent of each other no correlation effects need to be taken into account.

3.5 Uncertainties in Arrival Angle

Triangulation is the process of converting the local timing information to an air shower arrival direction in the horizon coordinate system. For an explanation of the horizon system see Section 4.2.3. The uncertainties in the arrival angles altitude, θ, and azimuth, ϕ, with respect to errors in the local timing can be determined by running a simulation with the triangulation routine and plotting the change in angle versus angle for each TDC bin.

For θ, a $\kappa/sin(\theta)$ dependence is expected. To test this, a simulation was done where the value of TDC 0 was kept constant at 3786 while the values of TDC 1 and 2 were varied in increments of 1 from 2631 to 3786. In the simulation detectors 1 and 2 were on an east-west baseline and detector 0 was directly north of the midpoint between 1 and 2. This setup gives the maximum angular uncertainty since it uses the smallest possible detector baseline (8.66 m). Longer baselines will provide a maximum of 12% lower uncertainty. This dependence on ϕ has been ignored. Figure 3.11 shows the change in θ for every increment of TDCs 1 and 2. The dependence of uncertainty on altitude was fit to the function $\kappa/sin(\theta)$, as can be seen in Figure 3.11. The fit gave $\kappa = 7.956 \times 10^{-4}$ radians per TDC bin, which corresponds to $1.82°/ns$. So the uncertainty in altitude is:

$$\frac{\delta\theta}{\delta t_{local}} = \frac{1.8°/ns}{sin(\theta)}$$

Since the uncertainty in local timing, δt_{local}, is 3 ns:

$$\delta\theta = \frac{5°}{sin(\theta)}$$

For the uncertainty in ϕ a similar simulation was completed, this time varying the TDC value of each detector independently. This produced three functions for the uncertainty in ϕ due to the δt_{local}, one for each detector. Figure 3.12 shows three plots, one for each detector. The quadratic sum of these three functions is a constant value for all azimuth angles:

$$\frac{\delta\phi}{\delta t} = 2.4°/ns$$

Since the uncertainty in local timing is 3 ns:

$$\delta\phi = 7°$$

72
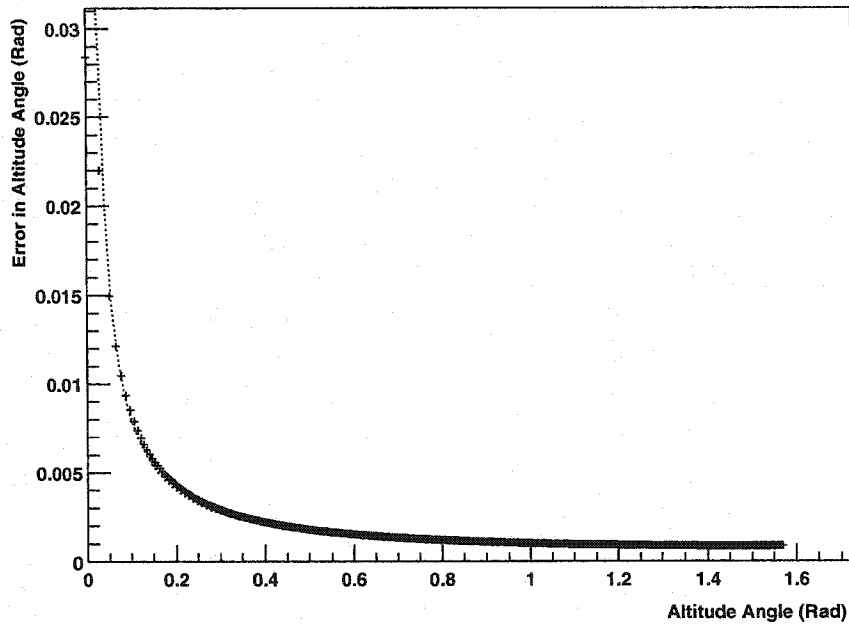
Figure 3.11: Plot of uncertainty in altitude angle as a function of altitude angle (crosses are data points, dotted curve is fit)
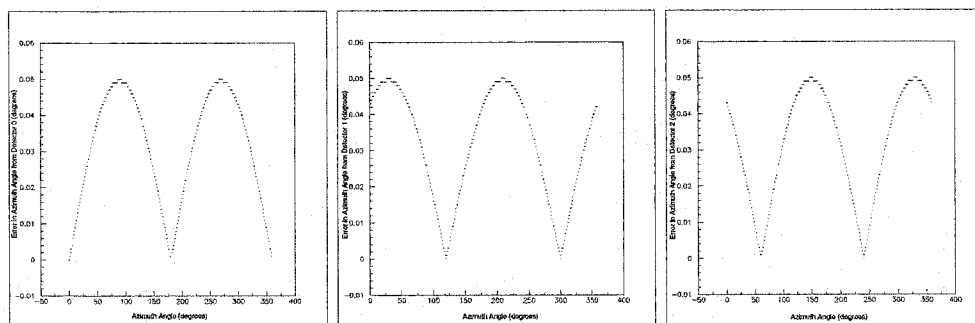
Figure 3.12: Plots of uncertainty in azimuth angle as a function of azimuth angle for varying TDC values in detectors 0, 1, and 2

Chapter 4

Analysis

The first step in analysing any data is organizing it. I'll begin this chapter by explaining how the data is organized, where it is stored, and how it is accessed. The latter sections of the chapter will describe the coordinate systems and analysis routines used to look for correlated and non-random cosmic ray arrival times.

4.1 Data Structure and Organization

Data collected by the electronics crate is read by the site's computer once every second. Each hour of data is written to binary files with an '.alta' extension. The file name is composed of the name of the site followed by the GPS time that the file started in the format 'NAME$yyyymmddhhmmss$'. The data is stored on the hard drive of the site computer until it is downloaded via a modem connection to a storage drive at the University of Alberta every 24 hours. The storage drive is currently a hard-drive on a computer, but will soon be a 600 GB Raid3 storage drive.

Each second of data has the block structure shown in Table 4.1. The .alta files are composed of the data from each second in sequential order. After being downloaded to the University the .alta files are read into the database, also to be located on the Raid3 storage drive. The structure of the database is shown in Table 4.2, and is currently being constructed.

All of the database information will be referenced by the site ID and the GPS time to the second. The "Raw Data" data block will also be referenced

Word Number	Description
1	site id number
2→5	used for debugging
6→8	GPS date (month, day, year)
9→11	GPS time (hours, minutes, seconds)
12	GPS sawtooth correction
13	number of b-latch values in the second, (i)
14	number of analog values in the second, (j)
15	number of coincidence values in the second, (k)
16	the a-latch value of the second
17→20	temperature readings (det0, det1, det2, crate)
21→21+i	b-latch values of the second from Time Tag Board
(21+i)→(21+i)+j	analog values of the second from Analog Board
(21+i+j)→(21+i+j)+k	coincidence values of the second Coincidence Board

Table 4.1: Word structure of ALTA binary data. (1 word = 32 bits)

by an *event number* which differentiates multiple events in a single second. Data will be retrieved from the database and calibration corrections applied during extraction. After the extraction a summary routine is run on the data to convert the data into a usable format. The summary routine converts A and B latch values to fractions of seconds, and converts TDC information to arrival angle in horizon, celestial, and galactic coordinate systems. The code for the summary routine is given in Appendix A.

4.2   Coordinate Systems

In order to compare the data from one site to another we must define some meaningful coordinate systems. The first is the site coordinate system, how the detectors are oriented at the site. The next is the coordinate system to relate site to site, and the final step is the coordinate systems used to point in some direction in the sky and universe.

4.2.1   Site Coordinates

The positions of the 3 detectors at a site must be clearly defined in order to derive any useful information from the local timing. As shown in Figure

Data Block	Contents	
Raw Data	sawtooth	B-A
	frequency	temperature[4]
	TDC[3]	ADC[3]
Timing Data	TTAGflag	DataType
	counter	CalBits
	sawtooth	temperature[3]
	ALatch	BLatchCnt
	ADCCount	TDCCount
Calibration Data	ADCPed[3]	MIPpeak[3]
	SignalDelay[3]	
Settings Logfile	StatusWord	CoinLevel
	Threshold[3]	HV[3]
	CalibOffset[3]	CalibVoltage
	Coin(ADC-DAC)[3]	HVScale[3]
	HV(ADC-DAC)[3]	
Static Input	Latitude	Longitude(λ_g)
	Altitude	GPSOffset
	SiteX[3]	SiteY[3]
	DAQVersion	HVSupply
	PMTType	ScintType
	CrateNumber	BoardNumber[7]
	IOBoardNumber	
Dynamic Input	StatusWord	RunDescription

Table 4.2: Block structure of ALTA database

4.1 the detector positions are described by their x and y coordinates in the frame with the GPS antenna at the origin, the $\hat{y}$-axis pointing to celestial (or geographic) north and the $\hat{x}$-axis pointing East. The GPS antennae are about 2 m above the plane of the detectors; this small correction is ignored.

The most challenging part of determining the detector positions in this coordinate system is determining what direction is north. It seems like a very simple problem and to 4 or 5 degrees of accuracy it is. Unfortunately getting much more accuracy than that is a more difficult problem. A magnetic compass measurement depends on two factors; the local magnetic field, and the conversion from magnetic to geographic north. Since the sites are on top of buildings, the local magnetic field can vary by tens of degrees depending on your position on the roof. A measurement with the GPS system is not
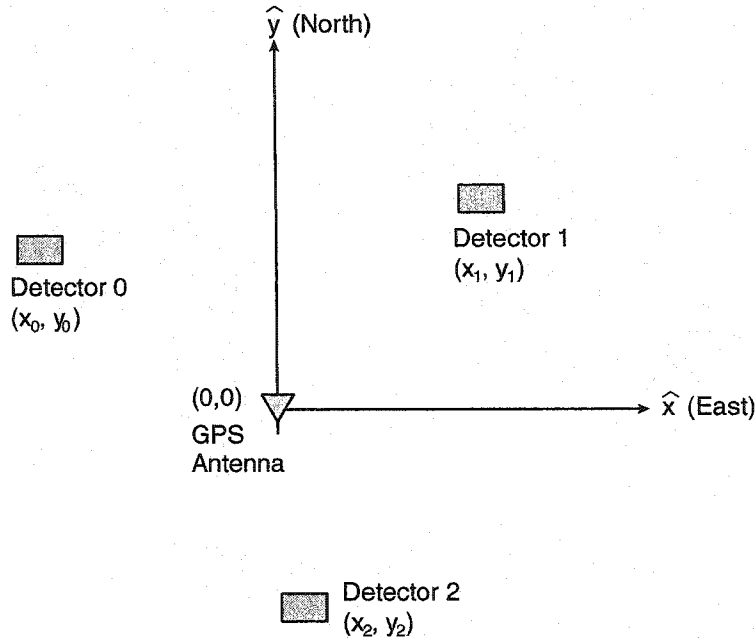
Figure 4.1: Coordinate system used to describe the positions of the detectors at a site

very accurate because the uncertainty in our GPS position is on the order of meters, while the baseline to compare two measurements is restricted to the roof of the building on the order of tens of meters. So there's also a significant uncertainty in this measurement.

The technique we have decided to use to determine the direction of geographic north is a solar compass. At local noon[1] (half way between sunrise and sunset) the sun will be directly south. The shadow of a vertical pole or plumb line will then point toward geographic north at local noon. The disadvantage of this measurement is the short baseline of the shadow. This can be overcome by making the pole or plumb line very long or by marking the location of the shadow near sunrise and then again near sunset - giving you an East-West baseline rather than a north-south one. To use this second method correctly you must be sure to use the shadow from the same point on the pole each time and be sure that the two measurements are taken at equal lengths of time before and after local noon.

---

[1] The website http://aa.usno.navy.mil/data/docs/RS_OneDay.html will calculate local noon to the minute for any latitude and longitude

Using the solar compass technique we can determine the direction of geographic north to within 2 degrees. The (x,y) positions of the detectors are determined to within 5 cm.

4.2.2 The Earth's Coordinate System

In order to compare one site to another we obviously need to determine their relative positions. We use the Earth's coordinate system of longitude, ρ, latitude, λ, and altitude to describe the sites' positions relative to each other. This seems easy enough, but there are some details that I would like to be sure are clear.

Geodetics is the science of defining the shape of the Earth. GPS uses a convention known as the World Geodetic System - 1984 (WGS84) to define the basic shape of the planet. WGS84 defines the Earth as a spheroid, an ellipse rotated about its minor axis. Figure 4.2 is a schematic of the Earth with the relavent WGS84 parameters.
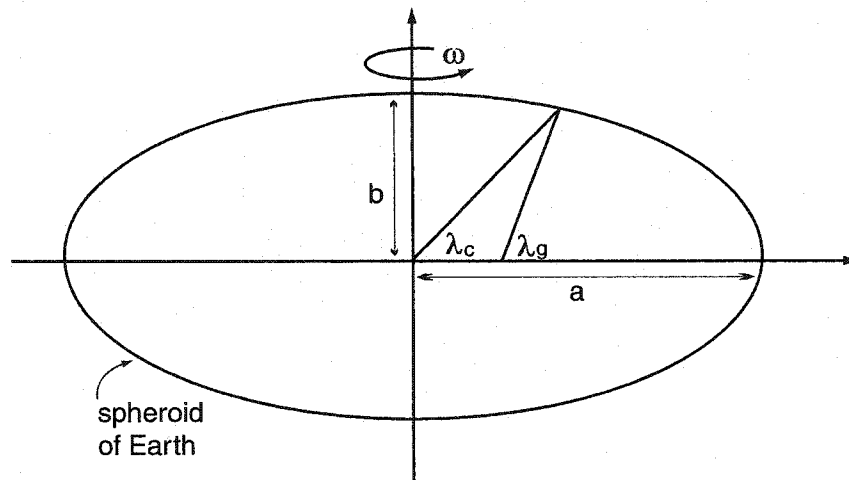
Figure 4.2: WGS84 parameter definitions.

Table 4.3 is an summary of the values of these parameters.

You may noticed that Figure 4.2 also includes two angles λ_c and λ_g. These angles are the *geocentric* and *geographic* latitudes, respectively. The geocentric latitude (λ_c) is the latitude we normally think of when we think latitude - the angle between our position, the center of mass of the Earth, and the equatorial

78

Parameter	Description	Value
GM_e	Earth Mass	$3.986004418 \times 10^{14} m^3/s$
w	Earth Rotation Rate	$7.292115 \times 10^{-5} rad/s$
a	Equatorial Radius	$6378137m$
f	Flattening, f=(a-b)/a	$1/298.257223560$

Table 4.3: WGS84 parameter values

plane. The geographic latitude (λ_g) is the angle between the line perpendicular to the Earth's surface at our position, and the equatorial plane. Why does geographic latitude exist? Because that is all that we can measure on the surface of the Earth. Think about it like this: If the Earth were a ball of water spinning in space with no currents or waves in the water (not too far from the truth), then the surface of the water would define a *gravitational equipotential* surface. If we are in an unknown location on the Earth and want to know our position we could drop a plum line to define vertical and then measure the angle between vertical and the north star. Which latitude would this give us? Well, it depends on where the plum line would point. Would it point to the center of mass of the Earth, λ_c, or would it point to the focus of the spheroid, λ_g? The plum line would point to the focus of spheroid because, as we all know, *field lines* are always perpendicular to *equipotentials*, and so the plum line would give us *geographic* latitude.

Geographic latitude is what appears on maps, and more importantly, is what GPS units display. We are going to use the site latitude to calculate the distance between two sites so we will need geocentric latitude. Thankfully the conversion is simple, and is as follows:

$$tan\lambda_c = \frac{b^2}{a^2} tan\lambda_g$$

The latitude quoted in the database is simply the geographic latitude determined by the GPS system. We convert to geocentric latitude whenever it is necessary in the analysis routines.

Longitude is defined as usual, with zero longitude at Greenwich and positive defined to the east (therefore $\rho_{Edmonton} \simeq -113°$). Altitude is defined as the height above the surface of the spheroid. This definition of altitude is different

than altitude above mean sea level. The difference between the two definitions is usually on the order of 10's of meters and varies from place to place on the globe.

4.2.3 Astronomical Coordinate Systems

Astronomers have many different coordinate systems that are convenient for describing and analysing various phenomena. There are three astronomical coordinate systems that lend well to the ALTA project which are descibed in this section. Each coordinate system is defined by a fundamental plane and a fundamental direction in that plane. For example, in the Earth's coordinate system the fundamental plane is the equatorial plane and the fundamental direction is the line from the centre of the Earth to the Greenwich meridian in the fundamental plane. The fundamental direction always defines the zero of the "around" angle, and the fundamental plane defines the zero of the "up/down" angle. An astronomical coordinate system does not define a distance to the astronomical object, it only gives the direction from the origin of the system to the object. So having said that, here are the astronomical coordinate systems that ALTA uses.

Horizon Coordinate System

A site's local timing allows us to point to the direction in the sky that a shower came from. This direction is most easily described in the horizon coordinate system. The horizon coordinate system's fundamental plane is the plane of the horizon that an observer on Earth would see if they spun around 360° (while standing vertically), and the fundamental direction is from the observer toward geographic north. The two angles of the horizon coordinate system are called altitude and azimuth. Figure 4.3, cf. [63], shows the coordinate system where X is the direction the shower came from, Z is the observers zenith (the point directly overhead), ϕ is the azimuth angle, and θ is the altitude angle. Some texts use the zenith angle instead of the altitude angle. The zenith angle is the angle between X and the observer's zenith (ie. $90° - \theta$)

This coordinate system is useful because it allows us to analyse the data
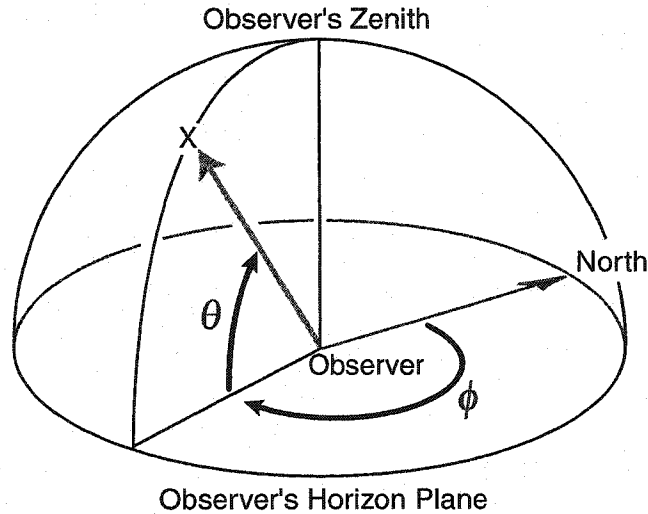
Figure 4.3: Horizon coordinate system

from a local perspective. For example, most showers we observe will be close to vertical, but we know the cosmic ray flux is isotropic, so why don't we see showers from all over the sky? The answer is that showers at lower altitude angles will have more atmosphere to penetrate, and so we will not observe as many showers.

The disadvantage of the horizon coordinate system is that it rotates with the Earth, it is an "Earth fixed" system. To see where in the universe an event pointed we need to know the horizon angles (altitude and azimuth) as well as the latitude, longitude, and time of the event. The next two coordinate systems do not have that drawback.

Celestial Coordinate System

The celestial (also known as the equatorial) coordinate system is Earth centered (origin at the center of the Earth), but not Earth fixed (does not rotate with the Earth). The fundamental plane is the equatorial plane of the Earth, and the fundamental direction is from the centre of the Earth to vernal equinox (also called the first point of Aries). A point in the celestial coordinate system is defined by the angles called right ascension and declination (RA, Dec) or (α, δ). Figure 4.4 shows the celestial coordinate system where α is the right ascension angle, and δ is the declination angle.

81
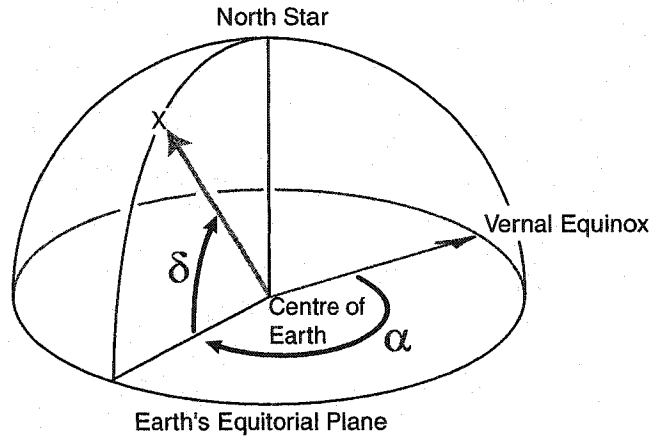
Figure 4.4: Celestial coordinate system

This is the most common coordinate system used to describe the location of stars. The celestial coordinate system will be the most commonly used system when looking for correlated cosmic ray pheneomena. The local timing information will be coverted to (RA, Dec) for comparison to other sites.

Galactic Coordinate System

The galactic coordinate system is often used when searching for phenomena originating in our galaxy. The two angles defining direction are galactic longitude, l, and galactic latitude, b. The fundamental plane is the plane of the galaxy, and the fundamental line is the line from our sun to the center of the galaxy, as shown in Figure 4.5.
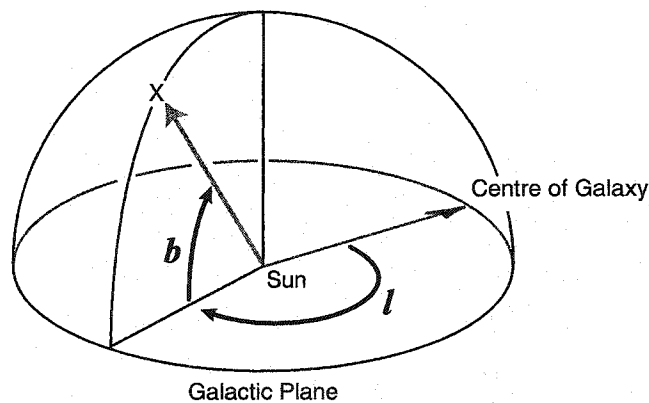
Figure 4.5: Galactic coordinate system

Table 4.4 is a summary of the astronomical coordinate systems used.

System	Fund. Plane	Fund. Line	"Around"	"Up/Down"
Horizon	observer's horizon	observer to north	azimuth (a)	altitude (A)
Celestial	Earth's equatorial plane	Earth to first point of Aries	right ascension (α)	declination (δ)
Galactic	galactic plane	sun to galactic center	galactic longitude (l)	galactic latitude (b)

Table 4.4: Summary of astronomical coordinate systems

4.2.4 Converting Local Timing To Horizon

Converting the local timing (relative arrival time of the shower front in the scintillators) information to horizon coordinates is an important step in the handling of the ALTA data. The process is called *triangulation*. In the conversion it is assumed that; 1) the shower front is planar, 2) the shower front is perpendicular to the shower axis, 3) the shower front is travelling at the speed of light in vaccum, c.

In order to be explain how the conversion is done I will first review some basic geometry. The equation of any plane which contains a point $p_0(x_0, y_0, z_0)$ is defined by:

$$A(x - x_0) + B(y - y_0) + C(z - z_0) = 0$$

A vector normal to that plane is then defined as $\vec{n} = (A, B, C)$. The distance from some point $p_i(x_i, y_i, z_i)$ to the plane can then be defined by:

$$d_i = \frac{A(x_i - x_0) + B(y_i - y_0) + C(z_i - z_0)}{\mid \vec{n} \mid}$$

where the sign of $A(x_i - x_0) + B(y_i - y_0) + C(z_i - z_0)$ determines if the point is above or below the plane. We will use these concepts in the following derivation of the conversion from the local timing to the azimuth and altitude angles.

Using the site coordinate system defined in Section 4.2.1 label the positions of detectors 0, 1, and 2 as p_0, p_1, p_2:

$$p_0 = (x_0, y_0, 0)$$

$$p_1 = (x_1, y_1, 0)$$

$$p_2 = (x_2, y_2, 0)$$

Now, imagine the shower plane as it is incident on detector 0. Let's call this plane Π. Π is therefore defined as:

$$A(x - x_0) + B(y - y_0) + C(z) = 0$$

where A, B and C are the direction numbers of the plane. Since the plane is propagating at the speed of light (c), we can define $\vec{c} = (A, B, C)$ (note that this just makes A, B, and C velocities). Therefore distance from a point x_i, y_i, z_i to Π is:

$$d_i = \frac{A(x_i - x_0) + B(y_i - y_0) + C(z_i)}{c}$$

Therefore,

$$d_0 = 0 \tag{4.1}$$

$$d_1 = \frac{A(x_1 - x_0) + B(y_1 - y_0)}{c} \tag{4.2}$$

$$d_2 = \frac{A(x_2 - x_0) + B(y_2 - y_0)}{c} \tag{4.3}$$

Solving for A and B using Equation 4.2 and Equation 4.3:

$$A = c \frac{d_2 - d_1 \frac{y_2 - y_0}{y_1 - y_0}}{(x_2 - x_0) - (x_1 - x_0)\frac{y_2 - y_0}{y_1 - y_0}} \tag{4.4}$$

$$B = c \frac{d_2 - d_1 \frac{x_2 - x_0}{x_1 - x_0}}{(y_2 - y_0) - (y_1 - y_0)\frac{x_2 - x_0}{x_1 - x_0}} \tag{4.5}$$

Using the time signals of the detectors t_0, t_1, and t_2, and the approximation that the shower is traveling at the speed of light, the distance from the plane to the detectors will be:

$$d_i = c(t_i - t_0) \quad i = 0, 1, 2 \tag{4.6}$$

Substituting these distances into Equation 4.4 and Equation 4.5 will give the direction numbers of the shower in terms of the time signals of the detectors and the positions of the detectors.

The direction numbers A and B can also be represented in horizon coordinates, azimuth (ϕ) and altitude (θ), by the equations:

$$A = c \cos \theta \sin \phi$$

84

$$B = c\cos\theta\cos\phi$$

To solve for the azimuth angle, take the fraction A/B:

$$\tan\phi = \frac{A}{B} \tag{4.7}$$

Substitude Equations 4.4 and 4.5 for A and B to get ϕ in terms of time and detector position.

Notice that the arc tangent function will result in azimuth angles in the range $(-\pi/2, \pi/2)$, while the azimuth angle requires a range of $(0, 2\pi)$ to cover the whole sky. This is because taking the fraction A/B creates an ambiguity, note $A/B = (-A)/(-B)$. To resolve this ambiguity we simply note the sequence of the coincidence and use logical arguments to resolve which quadrant the shower came from. This allows for the conversion of the range $(-\pi/2, \pi/2)$ to the range $(0, 2\pi)$.

To solve for the altitude angle, solve $A^2 + B^2$:

$$\cos\theta = \sqrt{\frac{A^2 + B^2}{c^2}} \tag{4.8}$$

Notice that if the square root is always assumed to be positive, then the altitude angle will be given from 0 to $\pi/2$, as desired. This ambiguity in the square root represents the fact that there is no way to tell if the shower came from above or below the detector. It is assumed that the shower comes from above.

This solution uses a simple linear system of two equations and two unknowns. When solving a system of linear equations the *condition number* of the system should be checked. The condition number will indicate whether the system is sensitive to small perturbations. The condition number is defined as the norm of the matrix (a 2×2 matrix in this system) multiplied by the norm of the inverse of the matrix. In this system the matrix is defined by the x_i and y_i values, so the condition number depends only on the positions of the detectors. The triangular positioning of the detectors optimizes the condition number.

4.2.5 Converting Horizon to Celestial

To convert from the horizon coordinate system to the celestial coordinate system we need to know the geographic latitude, λ_g, and longitude, ρ, of the detector array as well as the UTC (Coordinated Universal Time) and date of the event. To calculate the declination, δ, use Equation 4.9, from [63]:

$$\sin \delta = \sin \theta \sin \lambda_g + \cos \theta \cos \lambda_g \cos \phi \qquad (4.9)$$

Calculating the right ascension, α is only slightly more complex since we must first calculate the hour angle, HA, of the shower. The hour angle is the angular distance from the shower axis to the detector's meridian.

$$\cos HA = \frac{\sin \theta - \sin \lambda_g \sin \delta}{\cos \lambda_g \cos \delta}$$

To convert from hour angle to right ascension use Equation 4.10:

$$\alpha = LST - HA \qquad (4.10)$$

Where the hour angle is measured in hours, minutes, and seconds, and west is defined as the positive angular direction. LST is called Local Sidereal Time. Sidereal time is the time referenced from the stars, as opposed to universal time which uses the sun as a reference. There is a series of time conversions to go from UTC to LST which are detailed in Reference [63].

4.2.6 Converting Celestial to Galactic

The equations for converting celestial coordinates to galactic coordinates are [63];

$$b = sin^{-1}\{cos(\delta)cos(27.4°)cos(\alpha - 192.25°) + sin(\delta)sin(27.4°)\}$$

$$l = tan^{-1}\left\{\frac{sin(\delta) - sin(b)sin(27.4°)}{cos(\delta)sin(\alpha - 192.25°)cos(27.4°)}\right\} + 33°$$

where α is right ascension and δ is declination.

4.3 Analysis Routines

There are several different analysis routines, each looking for different phenomena. The routines are written in C. The important parts of the code are written in Appendix A. Here I will describe the steps of the routines.

4.3.1 Correlation Routine

The correlation routine, called correlation.c, searches for correlations in air showers between ALTA sites. When a correlation is found it could mean that correlated cosmic showers have been observed or that a very large shower covering several detectors has been observed. Figure 4.6 shows a schematic of a pair of hypothetical, perfectly correlated, cosmic ray air showers.
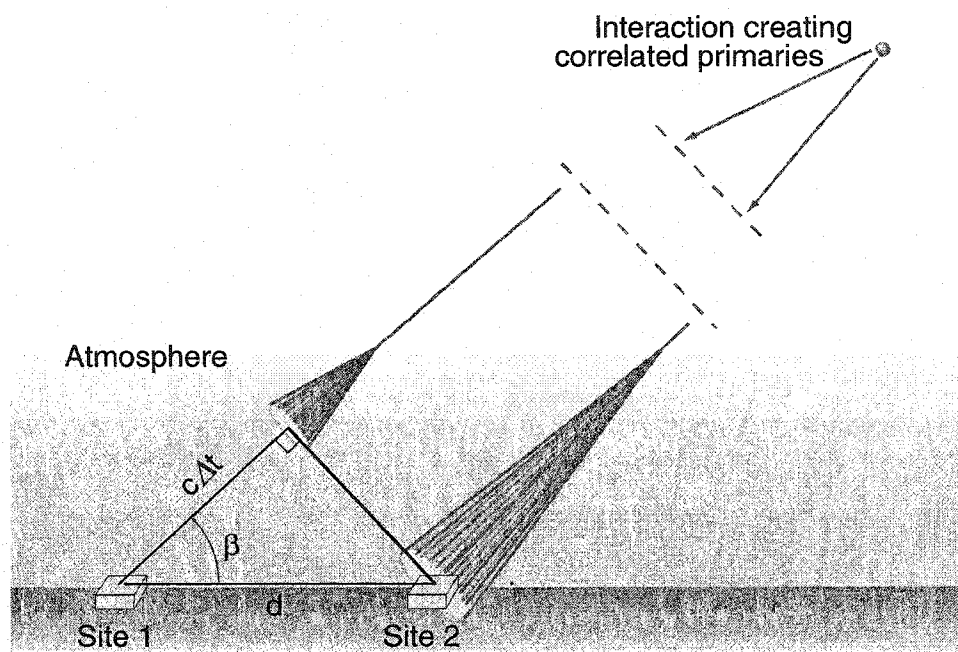
Figure 4.6: Hypothetical, perfectly correlated, air shower events

The correlation routine has two basic functions: to search for strictly correlated and very high energy air showers, and to search for angular correlations between air showers over large time intervals. A pair of strictly correlated air showers would be like those shown in Figure 4.6, while a very high energy air shower would be an air shower that was large enough to trigger more than one site. To differentiate these two possibilities we will need to look at the

87

particle density information from both sites and consider the distance between the sites. This can be done on an event by event basis. Searching for angular correlations over large time intervals is motivated by the possibility of a source that produces uncharged cosmic rays that would arrive at the Earth close in time, but not stricly correlated as defined by Figure 4.6. If the production or acceleration of these cosmic rays were to fluctuate with time a fluctuation in the total number of showers arriving from the direction of the source could potentially be observed.

The correlation routine has 3 basic steps, or cuts;

1. Determine if Δt is less than a specified time

2. Determine if the difference between the two arrival angles is less than a specified angle, ε

3. Determine if $c\Delta t \simeq dcos(\beta)$ (only used to search for strictly correlated and very high energy air showers)

To accomplish the first of the basic functions the first cut requires that $\Delta t < 1.1\tau$, where *tau* is the light travel time between the two sites being compared. The extra 10% (the multiplication by 1.1) is given to account for potential experimental error and shower fluctuations. Pairs of showers that pass the first cut progress to the second cut. To pass the second cut, the angle between the two shower axes must be less than 10° (that's roughly 2 times the uncertainty in the arrival angles). For the third cut the $c\Delta t - dcos(\beta)$ is required to be less than 0.2d. These cuts have been chosen to be loose cuts, since there will be few events that pass all three cuts. The events that do pass all of the cuts can then be examined closely, one at a time, to determine if they are a pair correlated showers or a single very high energy shower.

A rough estimate of the number of events that are expected to pass all three triggers can be attained by estimating the event rate for showers large enough to trigger two sites and adding the estimated event rate for correlated phenomena. The set of operational and in-planning sites: Ross Sheppard, MacDonald, Odysseum, and U of A cover an area of approximately 10 km^2

(Figure 2.2), so approximately 10 showers above the ankle ($\sim 10^{18.5}$ eV) can be expected to be incident on this area each year (Figure 1.2). Placing more sites within 5 to 10 km of each other would increase the expected rate. Placing sites south-east of U of A, connecting the O'Brien, W.P. Wagner, and Harry Ainlay group (Figure 2.2) with the U of A group, would be an efficient way of increasing effective detection area for high energy events. Using the Carrel [3] and Fegan [5] observations versus run time as very rough approximations an event rate of around 0.5 per year can be estimated.

The second basic function of the correlation routine is accomplished by setting the Δt cut to be less than the desired time interval, on the order of hours to days, and then applying the second cut. This produces a list of showers that arrived within $10°$, and within the specified time interval, in both sites being examined. This list can then be compared to other site pairs.

Correlation Routine Details

The following contains the details of how each cut is executed using the data given by the ALTA data acquisition system.

Determining τ

To determine τ (the light travel time between sites) the straight line distance between two sites, d, must be known. To determine d use the longitude, latitude, and altitude of the site. It is easiest to find the distance between two points in a Cartesian coordinate system, so convert to a right handed Cartesian system with the origin at centre of Earth, z-axis toward north pole, and y-axis toward Greenwich. Writing x, y, and z in terms of longitude,ρ, latitude,λ_c, and altitude:

$$x = R(\lambda_c)cos(\lambda_c)sin(\rho) \tag{4.11}$$

$$y = R(\lambda_c)cos(\lambda_c)cos(\rho) \tag{4.12}$$

$$z = R(\lambda_c)sin(\lambda_c) \tag{4.13}$$

where $R(\lambda_c)$ = Radius of Spheroid Earth at λ_c + Altitude. The radius of the WGS84 spheroid at any latitude can be calculated from the equation of an

ellipse:

$$\frac{1}{r^2} = \frac{cos^2(\lambda_c)}{a^2} + \frac{sin^2(\lambda_c)}{b^2}$$

Then simply calculate the distance (d) between points 1 and 2 with the Pythagorean Theorem:

$$d = \sqrt{(x_2 - x_1)^2 + (y_2 - y_1)^2 + (z_2 - z_1)^2}$$

Truncation errors in *cos* and *sin* are not a factor for distances greater than 1 meter if you use double values for λ_c and ρ in the code. With the straight line distance between the sites known, $\tau = d\,c$, where c=299792458 m/s.

Determining ε

The next cut in the analysis is the relative arrival angles of the showers. To calculate the angle between the shower axes (ε), the dot product is the simplest method. To take the dot product, the celestial coordinates must be projected onto a unit sphere in right handed Cartesian coordinates. In this projection y is pointing toward α=0, z pointing to δ=90 degrees:

$$x_i = cos(\delta_i)sin(\alpha_i) \tag{4.14}$$

$$y_i = cos(\delta_i)cos(\alpha_i) \tag{4.15}$$

$$z_i = sin(\delta_i) \tag{4.16}$$

So, using the dot product, the angle between shower axes 1 and 2, ε, is:

$$cos(\varepsilon) = (x_1 x_2 + y_1 y_2 + z_1 z_2);$$

ε can now be compared to the desired cut.

Determining $d\cos(\beta)$

The final cut in the analysis is comparing the correlated shower front with the global timing difference between showers, the $c\Delta t = dcos(\beta)$ test. $d\cos(\beta)$ is basically the same as the 2 dimensional triangulation in 2.1. The only complication is that there are two coordinate systems; the positions of the sites in latitude and longitude, and the shower axes in celestial coordinates.

So, consider a right-handed Cartesian coordinate system with its origin at the centre of the Earth, z-axis pointing toward north, and y-axis pointing toward Vernal Equinox (the zero of right ascension). To get the sites' coordinates in this system Equations 4.11 are used, just with ρ replaced by the angle Greenwich mean Sidereal Time (GST) + ρ. This angle is called 'Celestial Longitude' in the analysis code. It takes into account the rotation of the Earth in the non-Earth fixed coordinate system being used here. With the positions of the two sites known in this coordinate system; create a vector, $\vec{d}$, with a magnitude equal to the distance between the sites and a direction from the second site hit to the first site hit. Create another vector, $\vec{cr}$, this time a unit vector in the direction of the right ascension and declination of the showers (the average of two angles is used in the code). The dot product of these two vectors is then equal to $d\cos(\beta)$ (see Figure 4.6 for definition of β). $d\cos(\beta)$ can be calculated with the statement of the two vectors in the Cartesian coordinate system:

$$\vec{d} \cdot \vec{cr} = |\vec{d}||\vec{cr}|\cos(\beta)$$

Therefore:

$$d\cos(\beta) = x_d x_{cr} + y_d y_{cr} + z_d z_{cr}$$

Now, $d\cos(\beta)$ can be compared to $c\,\Delta t$.

4.3.2   Burst Find Routine

The burst find routine, burstfind.c, is designed to locate time periods of elevated count rate at a site. The routine simply reads sequentially through the data and searches for consecutive pairs of events that have a time difference, Δt, that is less than a user defined time, t_α. When a sequence of consecutive pairs with $\Delta t < t_\alpha$ is found, it is recorded as a burst with the number of events in the burst and the end time of the burst. The end of the burst is defined when one consecutive pair has $\Delta t > t_\alpha$, as shown in Figure 4.7. The routine is based on analysis by Katayose of the LAAS group [36], the code can be found in the Appendix A.

91

$$\Delta t_3 \cdots \Delta t_6 < t_\alpha$$
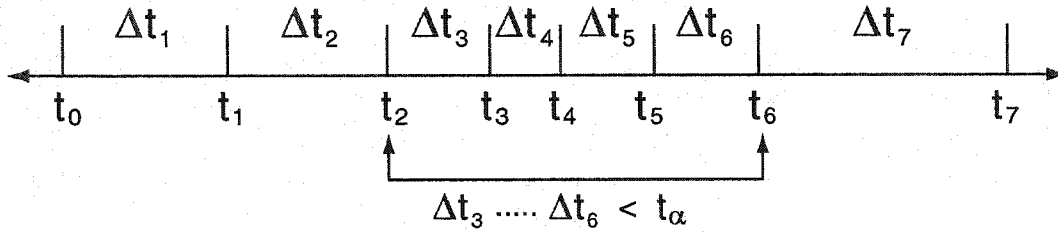
Figure 4.7: Burstfind routine would find a burst of 5 events ending at t_6

When a burst is found data from all other sites will be examined closely to look for bursts that occured at and around the same time.

4.3.3 Skyplot

There is another analysis tool, called skyplot, that plots the locations of events in a Hammer-Aitoff plot of the celestial or galactic coordinate systems. Figure 4.8 is an example plot of three hypothetical events with skyplot. Skyplot was written with ROOT by Doug Gish.
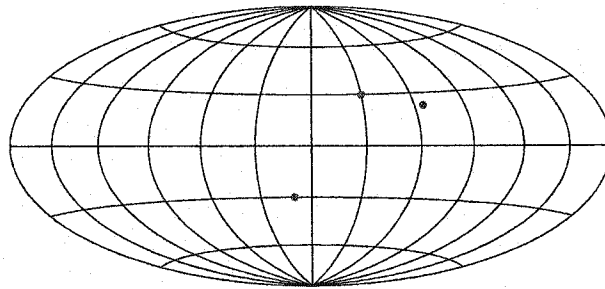
Figure 4.8: An example of 3 hypothetical events displayed with skyplot

Chapter 5

Conclusion

The Alberta Large Area Time Coincidence Array (ALTA) is almost ready
to search for cosmic ray phenomena that could be vital to unravelling some of
the mysteries surrounding cosmic rays. The possibility that cosmic ray showers
can be correlated over large distances has been glimpsed at, but never fully
explored. The existence of correlated showers could point the proverbial finger
at interactions and processes that could give valuable insight into the nature
of our universe. It is generally accepted that cosmic rays arrive at the Earth
randomly in time, but several experiments have shown that this might not be
the case. The presence of a component of the cosmic ray spectrum with some
structure in the arrival time could indicate possible sources of cosmic rays and
help solve the mystery of where cosmic rays come from.

ALTA currently has 6 sites in operation, each of them capable of deter-
mining the arrival time and direction of air showers with energies $\gtrsim 10^{14}$ eV.
The arrival time can be determined to about 16 ns, while the arrival angle
can determined to within 7° (for showers arriving at least 45° above the hori-
zon). In the near future the arrival angle uncertainty will be examined in more
detail by overlapping two sites and completing more extensive Monte Carlo
simulations. The overlapping arrays will on the roof of physics building at the
U of A. The current U of A site is already on the west roof of the physics
building, so a second site will be installed overlapping the existing site. This
overlapping site will be temporary. A permanent site will be installed on the
east roof of the physics building ($\sim$100 m away) to look for rates of larger air

showers.

ALTA is envisioned to have approximately 30 sites spread throughout the province of Alberta. Within the next 12 months at least 5 more sites are expected to be operational, with several more under construction.

ALTA and NALTA will be able to search for correlations in cosmic ray phenomena that will not be observable by the largest air shower arrays under construction today. When complete, the Auger project could provide an unparalleled observation of cosmic rays at the highest energies. When complete, the ALTA and NALTA experiments could provide a valuable observation of cosmic ray correlations over very large distances and time structure analysis with pointing information that is just begining to be examined in the cosmic ray research community.

Bibliography

[1] T. O'Halloran *et al.* **The Highest-Energy Cosmic Rays.** *Physics Today*, January:31, 1998.

[2] M. Nagano and A.A Watson. *Rev. Mod. Phys*, 72:689, 2000.

[3] O. Carrel and M. Martin. **Observation of time correlations in cosmic rays.** *Physics Letters B*, 325:526, 1994.

[4] N. Ochi *et al.* **Search for Coincident Air Showers in the Network Observation.** *Nucl. Phys. B (Proc. Suppl.)*, 97:169, 2001.

[5] D.J. Fegan *et al.* **Observation of a Burst of Cosmic Rays at Energies above 7×10^{13} eV.** *Phys. Rev. Lett*, 51:2341, 1983.

[6] T. Kitamura *et al.* **Chaos in cosmic ray air showers.** *Astropart. Phys.*, 6:279, 1997.

[7] C.L. Bhat *et. al.* **A Non-Random Component in Cosmic Rays of Energy $\lesssim 10^{14}$ eV.** *Nature*, 288:146, 1980.

[8] N. Ochi *et al.* **Search for Non-Random Features in Arrival Times of Air Showers.** *Il Nuovo Cim.*, 24C:719, 2001.

[9] Alta web page. http://csr.phys.ualberta.ca/alta.

[10] Nalta web page. http://csr.phys.ualberta.ca/nalta.

[11] V. Hess. **Observations of the Penetrating Radiation on Seven Balloon Flights.** *Phys. Z.*, 13:1804, 1912.

[12] R. Clay and B. Dawson. ***Cosmic Bullets.*** Addison-Wesley, 1997.

[13] M. Teshima *et. al.* **The Highest Energy Cosmic Rays Observed by AGASA.** *26th ICRC Highlight Papers*, page 365, 1999.

[14] K. Greisen. **End to the Cosmic Ray Spectrum?** *Phys. Rev. Lett.*, 16:748, 1966.

[15] G.T. Zatsepin and V.A. Kuz'min. *Zh. Eksp. Teor. Fiz.*, 4:114, 1966.

[16] J. Linsley. **Evidence for a Primary Cosmic Ray with Energy 10^{20} eV.** *Phys. Rev. Lett.*, 10-4:146, 1963.

[17] D.E. Groom. **Cosmic Background Radiation.** *European Physical Journal*, C15:1, 2000.

[18] L. Anchordoqui *et. al.* **Effect of 3K Background Radiation on UHECR.** *Phys. Rev. D*, 55:7356, 1997.

[19] C. Jui *et. al.* **Results from the High Resolution Fly's Eye Experiment.** *26th ICRC Highlight Papers*, page 370, 1999.

[20] Frauenfelder and Henley. **Subatomic Physics, 2nd ed.** Prentice Hall, 1991.

[21] S.P. Swordy *et al.* **The Composition of Cosmic Rays at the Knee.** *arXiv:astro-ph/0202159*, 2002.

[22] S. Yoshida *et. al.* **Cosmic Ray Energy Spectrum above .... ** *Astropart. Phys.*, 3:105, 1995.

[23] D. Bird *et al.* **The Cosmic Ray Energy Spectrum Observed by the Fly's Eye.** *Astrophys. J.*, 424:491, 1994.

[24] T. Abu-Zayyad *et al.* **Measurement of Cosmic Ray Energy Spectrum and Composition ....** *Astrophys. J.*, 557:686, 2001.

[25] J. Bahcall and E. Waxman. **Has the GZK Cutoff Been Discovered?** *arXiv:hep-ph/0206217*, 2002.

[26] Malcolm Longair. **High Energy Astrophysics, 2nd ed.** Cambridge University Press, 1997.

[27] E. Fermi. **Galactic Magnetic Fields and the Origin of Cosmic Radiation.** *Astrophys. J.*, 119:1, 1954.

[28] D. Torres *et al.* **Nearby Quasar Remnants and Ultra-High Energy Cosmic Rays.** *arXiv:astro-ph/0204419*, 2002.

[29] Z. Fodor *et. al.* **Relic Neutrino Masses and the Highest Energy Cosmic Rays.** *Phys. Rev. Lett.*, 88, 2002.

[30] T. Weiler. **Cosmic Ray Neutrino Annihilation ....** *Astroparticle Physics*, 11:303, 1999.

[31] G. Badino *et. al. Lett. Nuovo Cimento C*, 28:93, 1980.

[32] G. Smith *et al.* **Is there a Nonrandom Component in High-Energy Cosmic Rays?** *Phys. Rev. Lett*, 28:1601, 1983.

[33] D.J. Fegan *et al.* **Observation of a Burst of Cosmic Rays at Energies above 7×10^{13} eV.** *Proc. XVII ICRC (Paris)*, 51:2341, 1983.

[34] G. Smith *et al.* **Possible Observation of a Burst of Cosmic Ray Events in the Form of Extensive Air Showers.** *Phys. Rev. Lett*, 50:2110, 1983.

[35] K. Cheng. **Gamma-Ray Bursts: Afterglows and Central Engines.** *arXiv:astro-ph/0101147*, 2001.

[36] Y. Katayose *et al.* **A Search for Non-Random Cosmic Ray Time Series by a Cluster Analysis.** *Il Nuovo Cim.*, 21C:299, 1998.

[37] T. Konishi *et al.* **Arrival Direction of Successive Air Showers.** *Il Nuovo Cimento*, 24C:859, 2001.

[38] G.T. Zatsepin. *Dokl. Akad. Nauk SSSR*, 80:377, 1951.

[39] Zatsepin G.T. and Gerasimova N.M. *Soviet Phys. JETP*, 11:899, 1960.

[40] Watson A.A. and Medina-Tanco G.A. **The Photodisintegration of Cosmic Ray Nuclei by Solar Photons: The Gerasimova-Zatsepin Effect Revisited.** *Astropart. Phys.*, 10:157, 1999.

[41] L. Anchordoqui. **Cosmic Dust Grains Strike Again.** *Phys. Rev. D*, 61:087302, 2000.

[42] V. Berezinskiy *et. al.* **On the Hypothesis of Dust Grain Origin of Cosmic Ray Air Showers.** *Proc. XIII ICRC (Denver)*, 4:2493, 1973.

[43] Jacee web page. http://marge.phys.washington.edu/jacee/.

[44] Stacee web page. http://www.astro.ucla.edu/ stacee/.

[45] Hegra web page. http://wpos6.physik.uni-wuppertal.de:8080/.

[46] N. Hayashida *et. al.* **Observation of a Very Energetic Cosmic Ray ....** *Phys. Rev. Lett.*, 73:3491, 1994.

[47] Pierre auger project web page. http://www.auger.org.

[48] P. Auger. *Rev. Mod. Phys.*, 11:288, 1939.

[49] T. Wada *et al.* **Observation of Time Correlation in Cosmic Air Shower Network.** *Nucl. Phys. B (Proc. Suppl.)*, 75A:330, 1999.

[50] L. Villasenor *et al.* **Cosmic Ray Observations at Chacaltaya ....** *Poceedings of the 27th ICRC*, 2001.

[51] Bicron web page. http://www.bicron.com/bc408.htm.

[52] Philips data handbook, 1985.

[53] Philips data handbook. http://www.electrontubes.com.

[54] Trimble web page. http://www.trimble.com/gps.

[55] N. Ashby. **Relativity and the Global Positioning System.** *Physics Today*, page 41, May 2002.

[56] Tac32 web page. http://www.cnssys.com/.

[57] W. Brouwer *et. al.* **The ALTA Global Positioning Satellite Based Timing System.** to be published in *Nucl. Inst. Methods.*, 2002.

[58] D. Gedcke and W. McDonald. **A Constant Fraction of Pulse Height Trigger For Optimum Time Resolution.** *Nucl. Inst. and Methods*, 55:377, 1967.

[59] C Caso *et. al.* **Particle Data Book.** *Euro. Phys. J.*, C3, 1998.

[60] Kalmykov N.N., S.S. Ostapchenko, and A.I. Pavlov. *Nucl. Phys. B (Proc. Suppl.)*, 52B:17, 1997.

[61] Triumf kinematic handbook, 1987.

[62] Geant web page. http://wwwinfo.cern.ch/asd/geant/.

[63] Peter Duffet-Smith. ***Practical Astronomy with Your Calculator, 3rd Ed.*** Cambridge University Press, 1998.

Appendix A

Analysis Code

This appendix contains the code for the analysis routines described in Chapter 4.3. The code is written in C. In an effort to save space all of the code is not written here, only the important function calls and 'main' routines are written.

A.1 The Summary Routine

The summary routine is used before each of the other analysis routines to convert the TDC and Time Tag information into arrival angles (in horizon, celestial, and galactic coordinates) and arrival times.

main Program

```
//read through the input file with while loop

while( !feof(fpinput) )
{
//call conversion functions

timeconvert( sawtooth, delta, frequency, &time );
horizon( coin, &site, &angle );
celestial( &site, &time, &angle );
galactic( &angle );

    //write ouput file
}
```

timeconvert Function

```
struct TIME *timeconvert( int sawtooth, long delta,
double frequency, struct TIME *time )
{
  double fracsecond;

  fracsecond =  delta/frequency + sawtooth/pow(10,9);
```

```
    time->second = time->second + fracsecond;

    return( time );
}
```

horizon Function

```
struct ANGLE *horizon( int *coin, struct SITE *site,
        struct ANGLE *angle )
{
  double time[3], A, B;
  float x1, x2, y1, y2;
  int c =  299792458;

// Converting TDC value to seconds

  time[0] = 0.000000000025*coin[0];
  time[1] = 0.000000000025*coin[1];
  time[2] = 0.000000000025*coin[2];


// Calculating A and B values for azi and alt calculations

  x1 = site->x[1] - site->x[0];
  y1 = site->y[1] - site->y[0];

  x2 = site->x[2] - site->x[0];
  y2 = site->y[2] - site->y[0];

  A = c*( ( time[2]-time[0] )-( time[1]-time[0] )*( y2 / y1 ) )
 / ( x2 - x1 * ( y2 / y1 ) );

  B = c*( ( time[2]-time[0] )-( time[1]-time[0] )*( x2 / x1 ) )
 / ( y2 - y1 * ( x2 / x1 ) );


// Calculate azi and convert from [-pi/2, pi/2] to [0, 2*pi]

  angle->azi = atan( A/B );      // azi in rad [-pi/2 to pi/2]

  if ( angle->azi < 0 && angle->azi >= -pi/2 )
    { angle->azi = angle->azi + pi; }

  if ( time[1] > time[2] )     /* DEPENDS ON SITE GEOMETRY */
    { angle->azi = angle->azi + pi; }


// Calculate of alt angle

  angle->alt = acos( sqrt(A*A+B*B) );   // alt in rad [0 to pi/2]


// Algorithm fails for alt = pi/2 (since then azi is undefined)
```

```
// so this is the correction

  if( coin[0] == coin[1] && coin[1] == coin[2] )
  {
    angle->alt = pi/2;
    angle->azi = 0;
  }


  return angle;
}
```

celestial Function

```
struct ANGLE *celestial( struct SITE *site, struct TIME *time,
 struct ANGLE *angle )
{
// Convert the time from hour, min, sec to decimals

  decimalUTC = time->hour + ( time->minute )/60.0
+ time->second/3600.0;


// Convert lat to radians and lon to hours

  lat = (pi/180) * lat;
  lon = lon / 15.0;

// Calculations for ra and dec (ha is hour angle)

  angle->dec = asin( sin(angle->alt) * sin(lat) + cos(angle->alt)
* cos(lat) * cos(angle->azi) );

  ha = acos( ( sin(angle->alt) - sin(lat) * sin(angle->dec) )
 / ( cos(lat)*cos(angle->dec) ) );

  ha = ( ha / (pi/180) );

  if ( sin(angle->azi) > 0)
  { ha = 360 - ha; }

  ha = ha / 15;

  lst = GST(decimalUTC, time) + lon;

  if ( lst < 0 )
  { lst = lst + 24; }

  if ( lst > 24 )
  { lst = lst - 24; }

  angle->ra = lst - ha;      //ra in decimal hours
```

```
  if ( angle->ra < 0 )
  { angle->ra = angle->ra + 24; }

  if ( angle->ra > 24 )
  { angle->ra = angle->ra - 24; }

  angle->ra = (pi/12)*angle->ra;   //convert hours to radians

  return angle;
}
```

galactic Function

```
struct ANGLE *galactic( struct ANGLE *angle )
{
  angle->b = asin( 0.8878*cos(angle->dec)
*cos(angle->ra-192.25*(pi/180))
+ 0.4602*sin(angle->dec) );

  angle->l = atan2((sin(angle->dec)-0.460199784*sin(angle->b)),
(0.887815385*cos(angle->dec)
*sin(angle->ra-192.25*(pi/180)))) + 33*(pi/180);

  if( angle->l < 0 )
  {
    angle->l = angle->l + 2*pi;
  }

  return angle;
}
```

GST Fuction

```
double GST( double decimalUTC, struct TIME *time )
{
  double t, T, gst;

  t = ( JDate( time ) - 2451545.0 ) / 36525.0;
  T = 6.697374558 + 2400.051336*t + 0.000025862*t*t;

  if ( T < 0)
  {
   while ( T < 0 )
   { T = T + 24; }
  }
  else
  {
   while ( T > 24 )
   { T = T - 24; }
  }

  decimalUTC = 1.002737909 * decimalUTC;
```

```c
    gst = decimalUTC + T;
    if ( gst < 0 )
    { gst = gst + 24; }

    if ( gst > 24 )
    { gst = gst - 24; }

    return (gst);
}
```

JDate Function

```c
double JDate ( struct TIME *time )
{
  int year, month, day, A, B, C, D;
  float Date;

  year = time->year;
  month = time->month;
  day = time->day;

  if ( month <= 2 )
    { year = year - 1;
      month = month + 12;
    }

    A = (year) / 100;
    B = 2 - A + A/4;
    C = 365.25 * ( year);
    D = 30.6001 * ( month + 1);

    Date = B + C + D + day + 1720994.5;

    return(Date);
}
```

A.2 The Correlation Routine

This program finds correlations in cosmic ray showers between two sites.

Constant Variable Definitions

```
#define pi 3.14159265358979323846426433832795
#define a 6378137          // Earth's equitorial radius (WGS84)
#define b 6356752.314      // Earth's polar radius (WGS84)
#define c 299792458        // Speed of light in vaccum
```

main Program

```
//convert longitude and latitude to radians

site1.lon = (pi/180) * site1.lon;
site2.lon = (pi/180) * site2.lon;
site1.lat = (pi/180) * site1.lat;
site2.lat = (pi/180) * site2.lat;

//calculate tau (the light travel time between the sites)

tau = make_tau( &site1, &site2 );


//read through file 1 with while loop

while( !feof( fp1dst ) )
    {
    //read event from file 1

    //for each event in file 1, compare to event in file 2

    while( !feof( fp2dst ) )
    {
//read event from file 2

//sequence of if statements to make the comparisons

if( comparetime( &time1, &time2, tau ) == 1 )
{
   if( make_epsilon( &angle1, &angle2 ) <= delta )
   {
      if( fabs( time1.second - time2.second ) -
fabs( dcosbeta( ... ) / c ) <= DELTA )
      {
fprintf( fpoutput,"to output file" );
      }
   }
}
}
```

```
   rewind( fp2dst );
   }
```

comparetime Function

```
int comparetime( struct TIME *time1, struct TIME *time2,
 double tau )
{
   if( time1->year == time2->year )
     {
       if( time1->month == time2->month )
{
  if( time1->day == time2->day )
    {
       if( time1->hour == time2->hour )
{
  if( time1->minute == time2->minute )
    {
       if( fabs( time2->second
    - time1->second ) <= tau )
{
  return(1);
}
       else { return(0); }
     }
   else { return(0); }
}
       else { return(0); }
     }
   else { return(0); }
}
       else { return(0); }

   }
   else { return(0); }
}
```

make_epsilon Function

```
double make_epsilon(struct ANGLE *angle1, struct ANGLE *angle2)
{
   double epsilon;
   double ra1, ra2, dec1, dec2;
   double x1, y1, z1, x2, y2, z2;

// x, y, z on a unit circle,
// y is pointing in ra=0, z pointing to dec=90 degrees

   x1 = cos(dec1)*sin(ra1);
   y1 = cos(dec1)*cos(ra1);
   z1 = sin(dec1);

   x2 = cos(dec2)*sin(ra2);
   y2 = cos(dec2)*cos(ra2);
```

```
  z2 = sin(dec2);

// 1 dot 2 = cos(epsilon)

  epsilon = acos( x1*x2 + y1*y2 + z1*z2 );

  return( epsilon );
}
```

make_tau Function

```
double make_tau( struct SITE *site1, struct SITE *site2 )
{
  double tau;
  double x1, y1, z1, x2, y2, z2;
  double gclat1, gclat2;  /* gclat is GeoCentric LATitude */

  gclat1 = atan( pow( b/a, 2 ) * tan( site1->lat ) );
  gclat2 = atan( pow( b/a, 2 ) * tan( site2->lat ) );

  x1=(radius(gclat1)+site1->alt)*cos(gclat1)*sin(site1->lon);
  y1=(radius(gclat1)+site1->alt)*cos(gclat1)*cos(site1->lon);
  z1=(radius(gclat1)+site1->alt)*sin(gclat1);
  x2=(radius(gclat2)+site2->alt)*cos(gclat2)*sin(site2->lon);
  y2=(radius(gclat2)+site2->alt)*cos(gclat2)*cos(site2->lon);
  z2=(radius(gclat2)+site2->alt)*sin(gclat2);

  tau=sqrt(pow(x2-x1,2) + pow(y2-y1,2) + pow(z2-z1,2) )/c;

  return( tau );
}
```

radius Function

```
double radius( double lat )
{
  double radius;

  radius = 1/sqrt( pow(cos(lat)/a,2) + pow(sin(lat)/b,2));
  return( radius );
}
```

dcosbeta Function

```
double dcosbeta( ... )
{
  double x1, y1, z1, x2, y2, z2, xCR, yCR, zCR;
  double gclat1, gclat2;
  double cstlon1, cstlon2;
  double dcosbeta, dec, ra;
```

```
// convert geographic to geocentric latitude

  gclat1 = atan( pow( b/a, 2 ) * tan( site1->lat ) );
  gclat2 = atan( pow( b/a, 2 ) * tan( site2->lat ) );

// calculate cstlon "Celestial Longitude"

  cstlon1 = (pi/180)*(15)*GST( time1 ) + site1->lon;
  cstlon2 = (pi/180)*(15)*GST( time2 ) + site2->lon;

// calculate x, y, z and make site2 the last site hit
  if( time2 > time1 )
  {
  x1=(radius(gclat1)+site1->alt)*cos(gclat1)*sin(cstlon1);
  y1=(radius(gclat1)+site1->alt)*cos(gclat1)*cos(cstlon1);
  z1=(radius(gclat1)+site1->alt)*sin(gclat1);
  x2=(radius(gclat2)+site2->alt)*cos(gclat2)*sin(cstlon2);
  y2=(radius(gclat2)+site2->alt)*cos(gclat2)*cos(cstlon2);
  z2=(radius(gclat2)+site2->alt)*sin(gclat2);
  }

  if( time2 < time1 )
  {
  x2 = (radius(gclat1)+site1->alt)*cos(gclat1)*sin(cstlon1);
  y2 = (radius(gclat1)+site1->alt)*cos(gclat1)*cos(cstlon1);
  z2 = (radius(gclat1)+site1->alt)*sin(gclat1);
  x1 = (radius(gclat2)+site2->alt)*cos(gclat2)*sin(cstlon2);
  y1 = (radius(gclat2)+site2->alt)*cos(gclat2)*cos(cstlon2);
  z1 = (radius(gclat2)+site2->alt)*sin(gclat2);
  }

  if( time2 == time1 ) // if time1=time2 then dcosbeta=0
  {
     return( 0 );
  }

// taking average of ra and dec

  dec = ( angle1->dec + angle2->dec ) / 2;
  ra = ( angle1->ra + angle2->ra ) / 2;

//calculate xCR, yCR, zCR

  xCR = cos( (pi/180)*dec ) * sin( (pi/180)*15*ra );
  yCR = cos( (pi/180)*dec ) * cos( (pi/180)*15*ra );
  zCR = sin( (pi/180)*dec );

  dcosbeta = (x2-x1)*xCR + (y2-y1)*yCR +(z2-z1)*zCR;

  return( dcosbeta );
}
```

A.3 The Burstfind Routine

This program takes output of summary.c program and searchs for a non-random time series.

main Program

```c
//read the first event
//read sequential events with while loop
while( !feof( fpinput ) )
{
  previous_event = current_event;

  //read event

  delta_t = get_delta_t( &current_event, &previous_event );


  if( delta_t < time_interval ) //can be > for "anti-bursts"
  {
    if( index_check+1 == index )
    {
burst_counter[n]++;
      burst_event[n]=current_event;
    }
    index_check = index;
  }
  index++;

  if( index_check+2 == index ) //go to next burst_counter
  {
  n++;
  }
}
```

get_delta_t Function

```c
double get_delta_t( struct EVENT *current_event,
struct EVENT *previous_event )
{
  double delta;
  double current_time, previous_time;

  current_time = 3600*current_event->hour
  + 60*current_event->minute
  + current_event->second;
  previous_time = 3600*previous_event->hour
  + 60*previous_event->minute
  + previous_event->second;

  delta = current_time - previous_time;

  return(delta);
}
```

Glossary

ADC Pedestal The value of the ADC that corresponds to zero energy being deposited in the detector., page 59

ADC An Analog to Digital Converter is an electronic device that converts the amount of charge in (the size of) an electronic signal to a digital value., page 49

AGASA Akeno Giant Air Shower Array is a 100 km^2 ground based air shower array near Akeno Japan, page 26

Air Shower The cascade of particles produced when a high energy cosmic ray enters the atmosphere., page 2

Ankle The kink in the cosmic ray energy spectrum at $\sim 10^{18}$ eV is called the ankle., page 4

Auger The Pierre Auger project is a pair of 3000 km^2 air shower arrays being built in Argentina and the United States, page 26

Cerenkov Radiation Light created by a charged particle traveling faster than the local speed of light in a medium., page 16

CMB The Cosmic Microwave Background is electromagnetic radiation (photons) that seem to permeate the entire universe, page 4

Correlated Cosmic Rays Cosmic rays coming from some common origin creating air showers that would tend to point in similar directions. The cosmic rays could be *stricly* correlated, meaning that the primaries were all contained in a plane; or *roughly* correlated, meaning the primaries would all have come from the same direction, but not necessarily in a plane., page 20

Cosmic Ray Burst An increase in the rate of air showers over time intervals from seconds to hours., page 18

Cosmic Ray A high energy subatomic particle of extra-terrestrial origin.

Electromagnetic Shower An air shower initiated by a photon, page 12

eV An electron volt is a unit of energy: 1 eV $= 1.602 \times 10^{-19}$ J

Extensive Air Shower An air shower large enough to reach the ground., page 12

Flux The amount of something passing through some specified area in some specified time

Global Timing The relative timing between sites; the GPS time., page 32

GZK Limit The Greisen-Zatsepin-Kuz'min limit is a restriction on the distance protons with energy greater than 5×10^{19} eV are likely to travel due to pion production with the photons of the CMB, page 4

Hadronic Shower An air shower initiated by a hadron, page 14

Hadron A class of subatomic particles containing 3 quarks, protons and neutrons are the most common hadrons.

HiRes The High Resultion Fly's Eye experiment is a nitrogen fluorescence detector in Utah, USA; an upgraded version of the former Fly's Eye experiment, page 25

ICRC The International Cosmic Ray Conference is a gathering of cosmic ray researchers every two years to discuss progress and future goals in cosmic ray physics.

Knee The kink in the cosmic ray energy spectrum at $\sim 10^{15}$ eV is called the knee., page 4

LAAS Large Area Air Shower group is a group of 9 small air shower arrays in Japan., page 26

Local Timing The relative timing between the detectors at a site., page 32

MIP A Minimum Ionizing Particle is a particle that deposits ~ 2 MeV of energy in every g/cm^2 of material it passes through., page 57

Mpc A unit of distance equal to 1 million parsecs: 1 parsec $\simeq 3.2$ light years

Nitrogen Fluorescence Light created by an electron exciting atoms as it propagates through nitrogen gas, page 17

Nucleon A proton or neutron.

PMT A PhotoMultiplier Tube is a device that detects small amounts of light and converts it to a measurable electric signal., page 33

Primary Cosmic Ray The cosmic ray that initiates an air shower., page 2

Scintillator A material that emits a small flash of light when a charged particle passes through it., page 33

Secondary Cosmic Ray A particle produced in an air shower., page 2

Shower Front The roughly planar region that contains the secondary particles of an air shower., page 2

Spallation Spallation is the process of a heavy nucleus splitting appart, or fragmenting, when it interacts with a lighter nucleus

TDC A Time to Digital Converter is an electronic device that converts the time between two electronic signals to a digital value., page 45